

# 博士論文

Development of in Situ Quantitative Bridge Inspection  
System with Portable 950keV/3.95MeV Linac X-ray Sources  
(950keV/3.95MeV 可搬型 X 線源を用いたその場定量化  
橋梁検査システム開発)

WU Wenjing (武 文晶)

A thesis submitted in partial fulfillment for the  
PhD degree

Department of Nuclear Engineering and Management  
School of Engineering

**THE UNIVERSITY OF TOKYO**

June 2014



# *Acknowledgements*

I would like to express my sincere gratitude and love to all the people who were always there for me and helped me from every aspects in the process of this thesis.

Let me start with my very great appreciation to my supervisor, Professor Mitsuru Uesaka, for the careful guidance and comprehensive support to my research as well as my personal life during the last 3 years study.

I would also like to offer my gratitude to Assistant Takeshi Fujiwara, Mr.Katsuhiro Dobashi, and Mr.Joichi Kusano for their generous help and suggestions throughout my experiment. I feel particularly grateful for Mr. Hideyuki Sunaga and Ms. Yoshie Otake of Riken, Japan, for their expertise and valuable advice to my work.

My special thanks are extended to the stuff of Uesaka Laboratory, Ms. Kayoko Shigematsu and Ms. Moe Sekiguchi for their kind support and help. I'd like to thank all the lab members for the good times and friendly memories we had together. Special mention goes to Dr. Cuixiang Pei, Dr. Haitao Zhu, Mr. Ming Jin, Mr. Hiroshi Fujisawa, Ms. Ritu Bhusal Chhatkuli, Mr. Shiegeaki Sunada, Mr. Kazuhiro Tagi, Ms. Bhowmik Oiendril, Mr. Changheng Liu, Mr. Yusuke Nakamura, Mr. Shohei Otsuki, Mr.Sodai Tanaka, Ms.Yudhitya Kusumawati, Mr. Unico Bautista, Mr.Daiki Matsuyama, Mr.Masanori Akaike.

Also, I'd like to thank the examiners Professor Naoto Kasahara, Professor Hiroyuki Takahashi, Professor Koichi Maekawa, Associate Professor Hideaki Murayama, for the time they spend and advice they give on my thesis.

Advice and encourage given by Professor Zhenmao Chen of Xi'an Jiaotong University, China, has been a great help in inspiring me to insist my pursuit of knowledge in spite of difficulties in research work.

To my family, I am particularly grateful for the whole hearted support, comfort, and trust from my parents and younger sister.

To my beloved fiance, a heartfelt thanks goes for all the companion and understanding from him and for the love and our upcoming wedding.

# Contents

<b>Acknowledgements</b>	<b>i</b>
<b>List of Figures</b>	<b>iv</b>
<b>List of Tables</b>	<b>vii</b>
<b>Abstract</b>	<b>viii</b>
<b>1 Introduction</b>	<b>1</b>
1.1 Background . . . . .	1
1.2 Current Solutions and Difficulties . . . . .	4
1.3 A Short Review about NDE Techniques Using X-ray . . . . .	6
1.4 Objectives of This Research . . . . .	9
<b>2 In Situ NDE Experiment for RC and PC Structures</b>	<b>12</b>
2.1 Methodology of X-ray Radiography . . . . .	12
2.2 In Situ NDE Experiment for RC Structures . . . . .	13
2.2.1 Experiment set-up . . . . .	13
2.2.2 Results and discussion . . . . .	15
2.3 Quantitative Evaluation Methods for Steel Rebar Diameter Reduction . . . . .	15
2.3.1 Quantitative analysis by radiography imaging . . . . .	16
2.3.1.1 Analysis principle . . . . .	16
2.3.1.2 Experiment validation . . . . .	18
2.3.2 Imaging enhancement by tomosynthesis . . . . .	18
2.4 In Situ NDE Experiment for PC Structures . . . . .	20
2.4.1 Experiment set-up . . . . .	20
2.4.2 Result and discussion . . . . .	24
2.4.3 Incomplete and truncated projection problems . . . . .	27
<b>3 Simulation for Partial Computed Tomography</b>	<b>29</b>
3.1 Methodology of Computed Tomography (CT) . . . . .	29
3.2 Fundamental Reconstruction Algorithms . . . . .	32
3.2.1 Filtered Back Projection (FBP) . . . . .	32
3.2.2 Algebraic Reconstruction Technique (ART) . . . . .	33
3.2.3 Simultaneous Algebraic Reconstruction Technique (SART) . . . . .	34
3.3 CT Reconstruction of Incomplete Projection Problem . . . . .	35
3.3.1 Incomplete Projection Problem . . . . .	35

3.3.2	SART with Total Vibration (SART-TV) . . . . .	37
3.3.3	Simulation and discussion . . . . .	40
3.4	CT Reconstruction of Region of Interest (ROI) . . . . .	40
3.4.1	Truncated Projection Problem . . . . .	40
3.4.2	Differentiated Back Projection with Hilbert Transform (DBPH) . . . . .	43
3.4.3	Simulation and discussion . . . . .	46
<b>4</b>	<b>Computed Tomography Experiment for Incomplete Projection Problem</b>	<b>52</b>
4.1	Test with Commercial CT Device . . . . .	52
4.2	Experiment with 950keV Linac Source . . . . .	58
4.2.1	Experiment set-up . . . . .	58
4.2.2	Image reconstruction . . . . .	58
4.2.3	3D modelling and mechanical analysis by VCAD . . . . .	59
4.3	Experiment Improvement with Collimator . . . . .	63
4.3.1	Experiment set-up . . . . .	63
4.3.2	Result and discussion . . . . .	66
4.4	Image Reconstruction under Incomplete Projection . . . . .	70
<b>5</b>	<b>Computed Tomography Experiment for Truncated Projection Problem</b>	<b>78</b>
5.1	Experiment with Concrete Specimen of PC Bridge Girder . . . . .	78
5.1.1	Experiment set-up . . . . .	78
5.1.2	Results and discussion . . . . .	80
5.2	ROI CT Experiment with Scaled Downed Specimen . . . . .	83
5.2.1	Experiment set-up . . . . .	83
5.2.2	Results and discussion . . . . .	85
<b>6</b>	<b>Dual-energy Computed Tomography Analysis for Corrosion Evaluation</b>	<b>90</b>
6.1	Simulation about Dual-energy CT Analysis . . . . .	90
6.1.1	Methodology of dual-energy CT . . . . .	90
6.1.2	Simulation with monochromatic beam . . . . .	93
6.1.3	Simulation with spectrum beam . . . . .	98
6.2	Experiment for Material Identification of Rusty Iron Sample . . . . .	103
6.2.1	Experiment set-up . . . . .	103
6.2.2	Results and discussion . . . . .	105
<b>7</b>	<b>Conclusion and Future Work</b>	<b>109</b>
7.1	Conclusion . . . . .	109
7.2	Future Work . . . . .	111
	<b>Bibliography</b>	<b>113</b>

# List of Figures

1.1	Component of RC bridge . . . . .	2
1.2	Component of PC bridge . . . . .	3
1.3	Component of steel bridge . . . . .	3
1.4	Visual and tapping test . . . . .	5
1.5	Ultrasonic test . . . . .	6
1.6	Infrared thermography imaging . . . . .	6
1.7	Ground penetrating radar imaging . . . . .	7
1.8	Induced voltage change due to defect by eddy current test . . . . .	7
1.9	950keV Linac . . . . .	9
1.10	3.95MeV Linac . . . . .	10
1.11	Research work structure . . . . .	10
2.1	Illustration of radiography . . . . .	13
2.2	Experiment layout view . . . . .	14
2.3	Magnification ratio . . . . .	14
2.4	Transmission image of RC structure . . . . .	16
2.5	Quantitative analysis by radiography imaging . . . . .	17
2.6	Transmission images of inner rebar . . . . .	19
2.7	Tomosynthesis . . . . .	20
2.8	Shift-and-add (SAA) reconstruction . . . . .	21
2.9	PC structure . . . . .	21
2.10	End section of PC structure . . . . .	22
2.11	950keV Linac on the stage frame . . . . .	22
2.12	Detector on the stage frame . . . . .	23
2.13	Transmission image of RC rebar . . . . .	24
2.14	Transmission image of PC wire cluster taken with horizontal beam . . . . .	25
2.15	Inclined X-ray beam . . . . .	25
2.16	Linac and detector at inclined angle . . . . .	26
2.17	Transmission image of PC wire cluster taken with inclined beam . . . . .	27
2.18	constraints of in situ inspection . . . . .	28
3.1	X-ray beam . . . . .	31
3.2	Simulation phantom . . . . .	32
3.3	Reconstruction with full projection by FBP (SNR=17.3dB) . . . . .	34
3.4	Reconstruction with full projection by ART (SNR=20.7dB) . . . . .	35
3.5	Reconstruction with full projection by SART (SNR=22.2dB) . . . . .	36
3.6	Incomplete projection tomography . . . . .	37
3.7	Few view problem (10° increment) . . . . .	38

---

3.8	Limited angle range problem( $90^\circ$ ) . . . . .	39
3.9	Comparison of few view problem ( $10^\circ$ increment) . . . . .	41
3.10	Comparison of limited angle range problem( $90^\circ$ ) . . . . .	42
3.11	Truncation geometry of ROI problem for bridge inspection . . . . .	43
3.12	Standard truncation geometries . . . . .	44
3.13	Hilbert lines of ROI problem for bridge inspection . . . . .	45
3.14	Reconstruction for ROI by analytic methods . . . . .	46
3.15	Reconstruction for ROI by iterative methods . . . . .	47
3.16	Profile of horizontal line in ROI reconstruction image . . . . .	48
3.17	Reconstruction for ROI with limited angle range problem( $90^\circ$ ) by analytic methods . . . . .	49
3.18	Reconstruction for ROI with limited angle range problem( $90^\circ$ ) by iterative methods . . . . .	50
3.19	Profile of horizontal line in ROI reconstruction image with limited angle range problem( $90^\circ$ ) . . . . .	51
4.1	Y.CT Compact CT device of YXLON . . . . .	53
4.2	Small concrete sample . . . . .	54
4.3	Small concrete sample in compact CT device . . . . .	54
4.4	Transmission image of small concrete sample by compact CT device . . . . .	55
4.5	CT image of small concrete sample by compact CT device . . . . .	56
4.6	3D model of Small concrete sample built from sectional slices reconstructed by compact CT device . . . . .	57
4.7	Illumination of experiment layout . . . . .	58
4.8	Transmission image . . . . .	59
4.9	CT image of small concrete sample . . . . .	60
4.10	CT image comparison by FBP, ART, SART ( $180^\circ$ ) . . . . .	61
4.11	Post manual processing . . . . .	62
4.12	3D model meshing of small sample . . . . .	62
4.13	Mechanical model of structure analysis for small sample . . . . .	63
4.14	Structure analysis results for small sample: equivalent stress(MPa) . . . . .	64
4.15	Structure analysis results for small sample: displacement(mm) . . . . .	65
4.16	Configuration of IIC Todai Hybrid Scintillator . . . . .	66
4.17	IIC Todai Hybrid Scintillator with reference detector . . . . .	67
4.18	Experiment Schema of improved CT system . . . . .	67
4.19	Experiment set up of improved CT system . . . . .	67
4.20	Trigger synchronization system . . . . .	68
4.21	Transmission image . . . . .	68
4.22	CT image of small concrete sample of improved CT system . . . . .	69
4.23	3D model for small sample of improved CT system . . . . .	70
4.24	CT image of few view problem ( $10^\circ$ increment) using experimental data with FPD . . . . .	71
4.25	CT image of limited angle range ( $90^\circ$ ) using experimental data with FPD . . . . .	72
4.26	CT image of few view problem ( $10^\circ$ increment) using experimental data with FPD by SART-TV . . . . .	73
4.27	CT image of limited angle range ( $90^\circ$ ) using experimental data with FPD by SART-TV . . . . .	74

---

4.28	CT image using experimental data with line sensor ( $180^\circ$ ) . . . . .	75
4.29	CT image of few view problem ( $16^\circ$ increment) using experimental data with line sensor . . . . .	76
4.30	CT image of limited angle range ( $90^\circ$ ) using experimental data with line sensor . . . . .	77
5.1	Concrete specimen of PC bridge girder . . . . .	79
5.2	Experiment set up for big concrete specimen . . . . .	80
5.3	Transmission image of RC Steel rod (reduce scattered X-ray noise by lead blocks to rise S/N ratio) . . . . .	81
5.4	Transmission image at position A . . . . .	82
5.5	Transmission image at position B . . . . .	83
5.6	Detector efficiency of FPD and line sensor . . . . .	84
5.7	Scaled down specimen . . . . .	85
5.8	Experiment setup for ROI CT of scaled down specimen . . . . .	87
5.9	Transmission image of scaled down specimen . . . . .	88
5.10	ROI reconstruction for section of scaled down specimen . . . . .	89
6.1	Standard database of attenuation . . . . .	92
6.2	Program flowchart of dual-energy CT analysis . . . . .	93
6.3	Simulation phantom of dual-energy CT analysis . . . . .	94
6.4	F(Z) curve under 30/60keV (black: true value; red: interpolation value) . . . . .	95
6.5	Estimated material with monochromatic beam (30/60keV) . . . . .	96
6.6	Error of estimated material with monochromatic beam (30/60keV) . . . . .	97
6.7	Simulation model of dual-energy CT using spectrum beam . . . . .	98
6.8	EGS5 simulation results about spectrum and detector . . . . .	99
6.9	F(Z) curve under spectrum beam (black: true value; red: interpolation value) . . . . .	100
6.10	Estimated material with spectrum beam . . . . .	101
6.11	Error of estimated material with spectrum beam . . . . .	102
6.12	Experiment setup of dual-energy CT . . . . .	103
6.13	Rusty iron sample . . . . .	104
6.14	Transmission image of rusty steel sample . . . . .	105
6.15	Reconstructed image of rusty steel sample . . . . .	106
6.16	Estimated material of rusty steel sample . . . . .	107
6.17	Attenuation ability of Fe and $Fe_2O_3$ . . . . .	108
7.1	Research work structure . . . . .	110

# List of Tables

1.1	Comparison of current NDE methods for bridge . . . . .	7
2.1	Evaluation result of steel rebar thinning in RC structure . . . . .	15
2.2	Evaluation result of inner rebar radius . . . . .	18
4.1	Specifications of Y.CT Compact CT device of YXLON . . . . .	53
4.2	Specifications of 950keV Linac . . . . .	58
4.3	Specifications of small flat panel detector (Perkin Elmer XRD0822) . . . . .	59
4.4	Parameters of small sample . . . . .	63
5.1	Specifications of 3.95MeV Linac . . . . .	79
5.2	Specifications of large flat panel detector (Perkin Elmer XRD1622) . . . . .	80
5.3	Specifications of Amptek Mini-X X-ray tube . . . . .	86
5.4	Specifications of Hamamatsu CCD area image sensor (S10811-11) . . . . .	86
6.1	Parameters of materials in the phantom . . . . .	95

# *Abstract*

Techniques to inspect inner structure are highly demanded for aging bridges suffering degradation problems due to long years' service. Quantitative NDE system for bridge is under development in this research to realize in situ inspection with portable 950kV/3.95MeV X-band linac as beam source. The research scope focuses on early prevention of deterioration phenomenon of corrosion or crack in inner steel rebar and wire as well as steel components. In this research, specific inspection methods are proposed for inspection of reinforced steel rebar thinning problem, prestressed steel wire cluster soundness problem and corrosion of steel component problem. The method can provide credible quantitative reference for analysis by the beam bending theory to further verify the mechanical character and degradation performance.

The RC rebar is single steel rebar and it can be easily confirmed by radiography. In situ NDE experiment for RC rebar inspection is successfully implemented and diameter reduction is estimated quantitatively based on prior information. Referring to the inspection result, comprehensive evaluation is assessed by mechanical analysis. Hence final maintenance plan was established with economic measure so that budget is saved substantially. Quantitative rebar thinning evaluation can also be realized by deducing from analyzing radiography images at different geometry, when prior information is inaccessible. For example, 3mm diameter rod inside 40mm thickness polyethylene material is irradiated in test experiment. The distance between source and detector varies from 100mm to 40mm. By analyzing the diameter in these two images, the real diameter can be calculated and the error is just 3.2667%. The accuracy could be further improved by rising image resolution, enhancing boundary in the image by tomosynthesis and so on.

Similar field work of NDE experiment for PC structure was conducted. PC wire is very difficult to be discriminated clearly from simple radiography image, because more than 10 wires are overlapped in each cluster. Computed Tomography is adopted to provide detail information in sectional slice of object. Considering that bridge is large scale structure, it's impossible to realize full scanning during CT application and such situation would bring about artifacts in the sectional image. Advanced algorithms are studied and compared in this research with both simulation and experimental validation. Artifacts caused by incomplete projection problem of limited angle range or sparse view can be reduced by Simultaneous Algebraic Reconstruction Technique with Total Variation (SART-TV) algorithm. Furthermore, truncated projection data can still reconstruct region of interest effectively with Differentiated Back Projection with Hilbert Transform (DBPH) algorithm.

CT application is proposed focusing on degradation part and sectional images can be reconstructed with projection data obtained to detect interior details. Further structural analysis is possible to estimate the mechanical characters of bridge with 3D model built from CT sectional images. A small concrete sample is tested with 950keV Lianc and analysis is realized including sectional image reconstruction, 3D modeling and mechanical analysis. The system is further improved by collimator to suppress scattered X-ray noise.

Assessment of steel components corrosion can be estimated through deducing material components of atomic number and density from dual-energy CT analysis. Corrosion will be distinguished and the rusty layer or the rust rate of steel rebar or wire would be verified in the analysis. Simulation was calculated by developed program using the sample of concrete including one steel rod with corrosion coating. The result shows that Fe and Fe<sub>2</sub>O<sub>3</sub> can be identified correctly and apparently. Relative experiment was done using seriously eroded iron component cut from bridge. The estimated atomic number shows large error from the standard value for several reasons, such as lack of real spectrum information, unstable operation condition, and scattered X-ray noise. Correspondent solutions are proposed by calibration with reference sample, denoising measures, compensation algorithm, etc.

In a word, the proposed method and inspection results would provide meaningful information for bridge NDE referring to mechanical analysis and civil work criterions.

# Chapter 1

## Introduction

### 1.1 Background

In late half of last century since 1960, Japan began to enter a period of rapid economic development in order to achieve the main objective of the modernization. A lot of social public infrastructure was constructed during that time, including highways, tunnels, bridges, etc. Take the bridges as an example, totally about 13,000 bridges were constructed over Japan until 1960, while comparatively the number tripled to over 41,000 after just 10 years. [1] Most of those bridges were made of concrete and steel and they have already sustained for several decades up to now. Henceforward, recently the number of aging bridges that have been constructed for more than 50 years would increase sharply, which brings about huge dangerous threat to normal use and great economic burden to maintenance. In recent years, cracking and fracture and even collapse accident happened from time to time. For example, in 2006, more than 1m crack occurred in Yamazoe Bridge, near Nara, Japan, between the crossbeam and the main girder due to fatigue. In addition, in 2007, corrosion of steel truss bridge component caused fracture in Kiso River Bridge, near Aichi, Japan, which had been forced to traffic regulation temporarily during the repair constructing work. [2] Other countries are facing the similar problem as Japan. For instance, in the U.S., the sudden collapse of Mississippi River Bridge caused tragedy of 13 deaths and more than 140 injuries on August 1, 2007. [3] Therefore, it becomes very urgent and important global issue to perform proper inspection and maintenance to deterioration of the aging bridges.

There are mainly 3 types of the constructed bridges:

- Reinforced concrete bridge (RC bridge)

As we know that concrete is very strong in compression while weak in tension, necessary strengthen measure is always taken by embedding some steel rods or wires. The reinforced concrete contains reinforcing steel bars which can resist tensile force.

- Prestressed concrete bridge (PC bridge)

Prestressed concrete is a composite material that the concrete is casted around steel wires which is placed in tensile force. The steel wires are always set in clusters or bundles. Then the prestress can form a built-in compression situation inside concrete. When loading is applied to the beam, the caused tensile stress will be balanced by compressive stress of steel wires and the beam would be much more resistant than ordinary one.

- Steel bridge

High strength and elasticity of steel make it popular for long bridges, usually in truss structure. Steel components are connected by bolt and welding, and painting proof is coated against corrosion.



FIGURE 1.1: Component of RC bridge

For RC and PC bridge, it would become very dangerous if corrosion or crack happens in steel rebar or wires, which play the crucial role of resisting the tensile force. Corrosion of steel bridge is also a serious problem. The main causes of deterioration are usually considered as fatigue, wet, and salt. Repeated dynamic traffic loading and thermal stress can lead to crack or hole in concrete and cracking in steel welding parts. Wet and salty environment due to rain and sea water would result in corrosion of steel rebar and wires and other steel components, as well as cracking of concrete caused by volume



FIGURE 1.2: Component of PC bridge



FIGURE 1.3: Component of steel bridge

expansion of rust. If those degradation problems cannot be detected and fixed promptly in advance, there might be a high risk of accidents.

The soundness of embedded steel rebar and wires are very critical for the mechanical performance of bridge. When evaluating the usability and safety against destruction, the cross section of steel rebar and wire is the most crucial parameter to estimate the allowable safety loading degree. For evaluation of the bridge beam by mechanical analysis, appropriate formula is provided under different strain conditions. The bending moment can be calculated based on the beam configuration and steel material usage. According to beam bending theory, to assure the safety, the final bending moment should be no more than the fracture resistance bending moment, which is largely determined by cross section of the steel rebar and wire. Diameter reduction or fracture of steel material

caused by degradation would greatly reduce the fracture resistance ability of the whole bridge.

## 1.2 Current Solutions and Difficulties

Several Nondestructive Evaluation (NDE) techniques are used in current preventive maintenance against bridge degradation, such as visual and tapping test, ultrasonic test, infrared thermography, ground penetrating radar with microwave, eddy current test, etc. Visual and tapping test is the most convenient and economic method to detect surface crack. It can also be used to check if the welding or bolt become loosening. Because it need manual work to find the defects by human visual check to the structure surface and hearing sense about the tapping sound, there would be large variation of accuracy and only very experienced investigators can be qualified for the job, not to mention the time consuming and low efficiency problem. [2]

Another economic method uses ultrasonic test to measuring the thickness or find superficial cracks by analysing the propagation of reflected acoustic wave. The inspection apparatus is portable and easy to use. However, the biggest problem is that in order to assure the wave propagation and the receiving of reflection signal, ultrasonic test has high requirement about the surface condition of the inspected object. The roughness of the surface should be relatively smooth and coupling agent is always necessary. Another problem is that diffraction makes it difficult for inspecting complex structures and the resolution is limited. [4]

Based on temperature information, infrared thermography can detect shallow crack. The limited accuracy is mainly constrained by environment that wet and temperature have great influence in inspection results. [5]

Ground penetrating radar detects radar pulses of electromagnetic microwave radiation. A variety of media material can be inspected to exam voids, cracks and other defects. The results is not so intuitive and additionally, the diffraction effect and the low resolution limits its application to shallow defect inspection. [4]

For conductive material, it can also be inspected by eddy current test to discriminate the conductivity variation among common media material and defects. It's effective to shallow cracks as long as the cracks are not in complex shape. [6]

As compared in the Table 1.1, these methods can detect surface or superficial crack very economically and efficiently, although some may be restricted by object condition, environment or materials. However, before surface or superficial crack is induced which



(A) Surface cracking



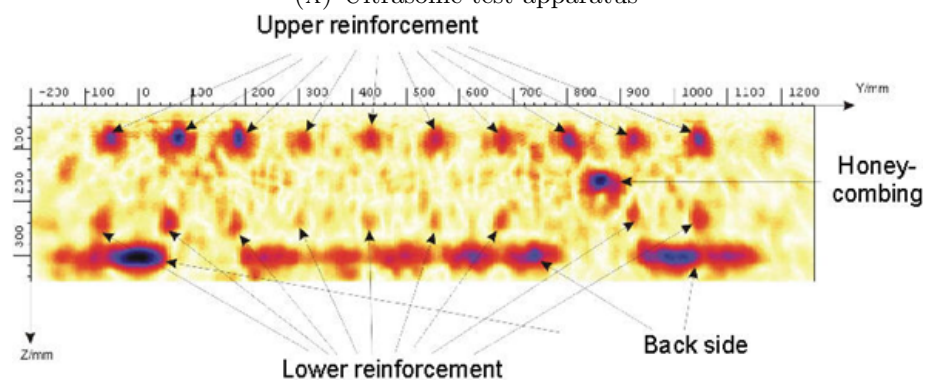
(B) Manual work

FIGURE 1.4: Visual and tapping test

may be detected with the above NDE methods, damages inside concrete would already happened to inner steel rebar or wires. Common defects like voids, cracking and corrosion of inner structure have great influence to load bearing capacity and durability of the whole structure. Beyond the detection scope of these conventional NDE methods, there's is still possible risk that early deterioration inside structure would cause dangerous accidents. The current problem is that none of the above mentioned methods can provide effective and intuitive inspection of internal structure with a certain amount of depth. So it's significantly meaningful to develop new technique to inspect the inner structure in the sense of preventive maintenance.



(A) Ultrasonic test apparatus



(B) Ultrasonic imaging

FIGURE 1.5: Ultrasonic test

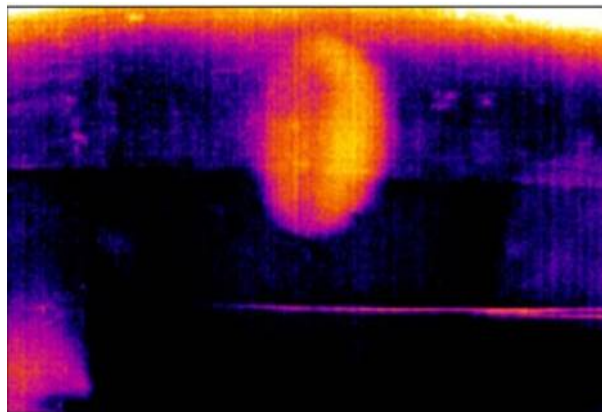


FIGURE 1.6: Infrared thermography imaging

### 1.3 A Short Review about NDE Techniques Using X-ray

When it comes to inspection of internal structure, NDE techniques using X-ray become better solutions to provide visual inner structure image. The most common way is radiography. The first X-ray image was taken by the German physicist Wilhelm Rontgen who won the Noble Prize in Physics in 1901 for his discovery of X-ray. [7]

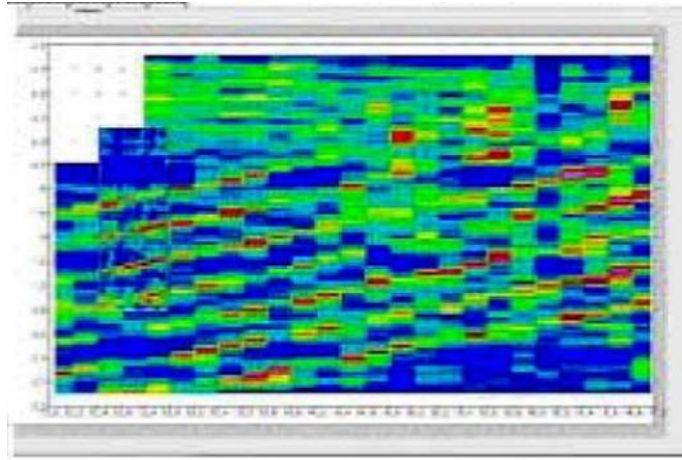


FIGURE 1.7: Ground penetrating radar imaging

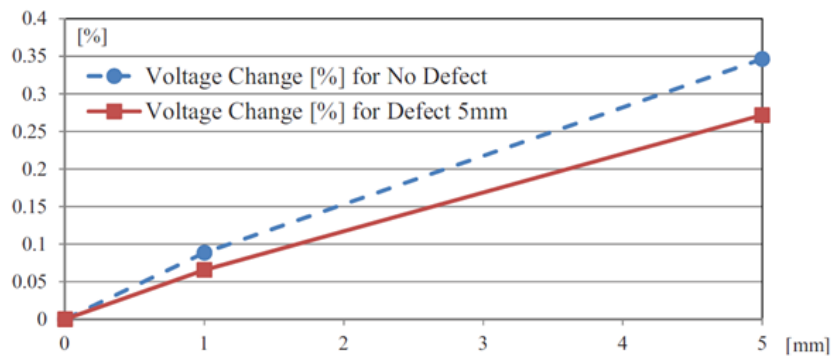


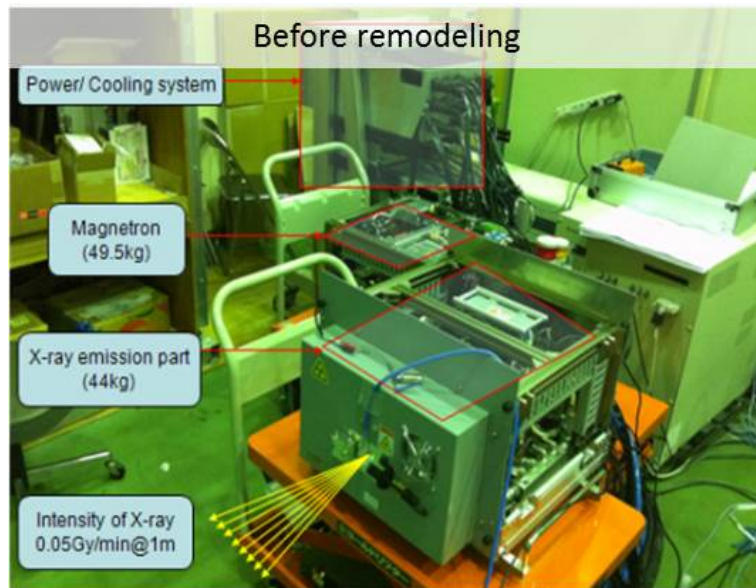
FIGURE 1.8: Induced voltage change due to defect by eddy current test

TABLE 1.1: Comparison of current NDE methods for bridge

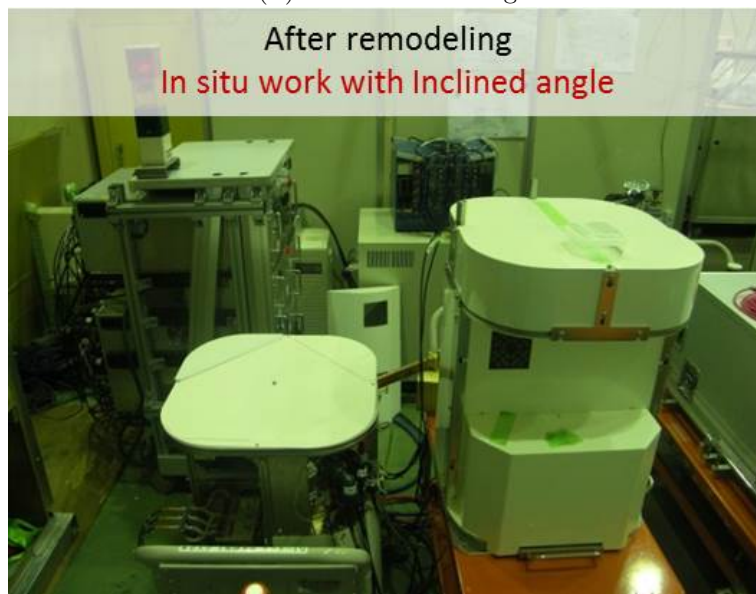
NDE Method	Application Scope	Problems
Visual and tapping test	Surface crack Loosening of bolt	Need experienced investigator Low efficiency Accuracy with large variation
Ultrasonic test	Thickness Superficial crack	Limited resolution Requirement of surface condition Difficult for complex structure
Infrared thermography	Shallow crack	Influence by environment (wet, temperature) Limited accuracy
Ground penetrating radar	Shallow crack	Limited resolution Diffraction influence Indirect
Eddy current test	Conductive material Shallow crack	Difficult for complex crack Limitation to material Need Experienced investigator

Very soon after the discovery, X-ray imaging was widely put into medical diagnoses use. The application to NDE is also very early in the inspection of welding defects, holes and flaws in industrial products. Dr. H. Lester developed fundamental methods of industrial X-ray radiography for metals in 1920s. [8] Similar application can be found in inspection for storage tanks, pipelines of gas or oil, components of vehicles or aircraft, etc. [8] However, the field inspection by X-ray radiography for bridge is not so widely used due to several reasons. Firstly, the legislation against radiation hazard confines the application scope. Secondly, there's very little X-ray equipment suitable for field work of bridge inspection. Most accelerators are too heavy to be moved. Portable devices are physically small but always have limited penetration ability and take long measuring time. For example, according to work done by Public Work Research Institute (PWRI), Japan, 300keV X-ray tube took 60min to irradiate 400mm thickness concrete of cut bridge girder part, in order to get transmission image. Another example is the Betatron (4MeV) of Hiroshima University, which cannot succeed in imaging because of weak dose and confines by safety regulations. [9] Aimed at realization of in situ inspection by X-ray radiography, portable 950keV/3.95MeV X-band (9.3GHz) linac X-ray sources have been developed in Uesaka laboratory, The University of Tokyo. In experimental room, 950keV system can achieve almost real time scanning for a petrochemical pipe of 8mm thickness and 300mm diameter. The holes of 1 mm and 5mm diameter in the pipe can be clearly detected. After newly remodeling, the equipment can work with inclined angle and its inspection scope is further expanded. The 3.95MeV system just need 1sec to get transmission view of concrete PC bridge sample with 400mm thickness. [9] Both of the two X-ray sources is possible to apply field work according to law revision in 2005 that temporary outdoor use of X-ray source less than 4MeV is allowed. [9]

Comparatively, Computed Tomography (CT) is a more advanced method to acquire more details about internal information of opaque objects through sectional view of internal structure. The first CT scanner was invented by G. Hounsfield, 1972. [10] Medical diagnose imaging is the most common application of X-ray CT and new generations are improved over the past decades. [11–14] Industrial CT is helpful to detect defects, voids and cracks within an object nondestructively. [15] It can also provide reference for design and assembly with 3D CT technique. [16] Dual-energy CT plays a role in material analysis especially to identify unknown inner materials, which can be used to medical diagnose or security inspection at airport or so on. [17, 18] As for inner structure inspection of composite concrete material, Lawrence Berkeley Laboratory showed possible applications of CT in civil engineering by simulate the limited angle tomography of reinforced concrete columns. [18] No substantive experiment or on site work about X-ray CT for composite concrete material is published yet.



(A) Before remodeling



(B) After remodeling

FIGURE 1.9: 950keV Linac

## 1.4 Objectives of This Research

Concerned about the high demanding of inspection for inner structures of aging bridges, this research worked on developing an in situ NDE system using portable 950keV/3.95MeV linac X-ray sources. The research scope focuses on early prevention of deterioration phenomenon of corrosion or crack in inner steel rebar and wire as well as steel components. For the RC rebar with diameter around 10~25cm, the thinning is evaluated through X-ray radiography. Since 2~3% thinning rate would be very critical for RC bridge and collapse may be induced under such situation, inspection accuracy of

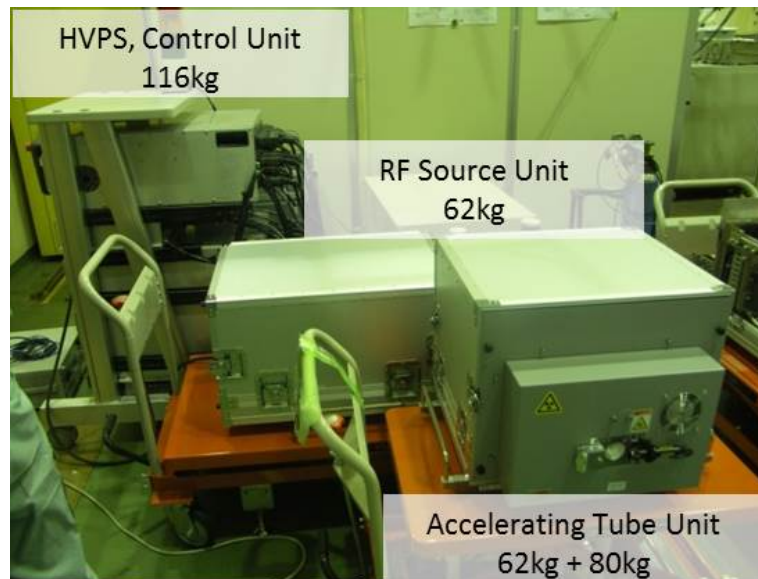


FIGURE 1.10: 3.95MeV Linac

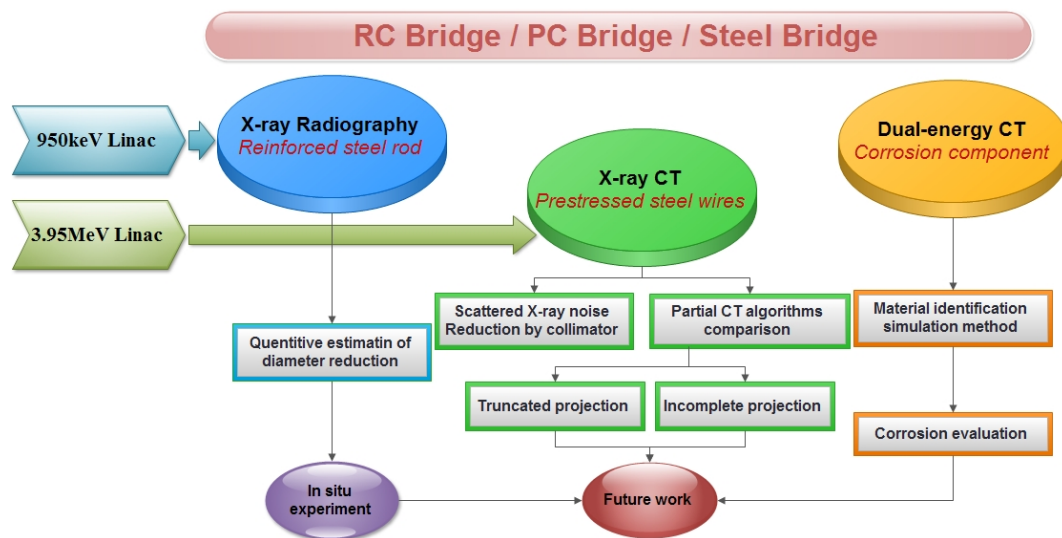


FIGURE 1.11: Research work structure

1~3mm is expected. For the PC wire clusters, the detection of details will be examined in sectional image by X-ray CT. Although the diameter of PC wires is around 7mm, PC bridge is much more robust than RC bridge and it can still sustain under thinning rate of 7~10%. Resolution of CT image is expected to be 1mm. For the steel components, corrosion will be distinguished by dual-energy CT analysis. The rusty layer or the rust rate of steel rebar or wire would be verified in the analysis. The structure of this research work is presented in figure 1.11. The mentioned inspection results would provide meaningful information for further evaluations referring to mechanical analysis and civil work criterions.

The thesis is organized as following: after introduction, the in situ inspection experiment for RC structure with portable X-ray source is explained in chapter 2, as well as the similar work for PC structure. Based on such experience and considering incomplete CT, relative simulation is carried out and illustrated in chapter 3. Then the CT experiment with small concrete sample is introduced in chapter 4. The following chapter 5 presents the experiment with concrete specimen slice cut from bridge girder and ROI CT work with a scaled down specimen. Afterwards, dual-energy CT to analysis corrosion situation, especially experiment with rusty steel component is explained in chapter 6. The conclusion and future work are discussed in the final chapter.

## Chapter 2

# In Situ NDE Experiment for RC and PC Structures

Referring to fundamental theory of X-ray radiography, in situ NDE experiments for RC and PC structures are carried out respectively. This chapter describes the in situ work and results in details and discussed problems that might appear during future CT in situ work.

### 2.1 Methodology of X-ray Radiography

When X-ray beam is penetrating through a general object, it will be absorbed or scattered by the material along the path which it passes through. The main interaction with the matter would be Photoelectric Effect, Compton Scattering, Pair Production and the mechanics details are related with the frequency and energy besides materials. If the material is denser, there will be greater absorption. Furthermore, if the material is thicker so that longer the path X-ray passes through is, greater the absorption would be. The ability of absorption of the material for a certain beam is described by attenuation coefficient  $\mu$ . The formula 2.1 of the Beer-Lambert law reveals the relationship between the transmitted intensity of the radiation  $I$ , and the incident intensity  $I_0$ , where  $x$  is the thickness of the object, or say, the path length.

$$I = I_0 e^{-\mu x} \quad (2.1)$$

For heterogeneous material or objects with inclusion, the absorption is determined by the integrated effects of the whole mass media. The relationship is considered as

formula 2.2 similarly and the contrast in the transmission image will provide the information about inclusion as figure 2.1 indicates.

$$I = I_0 e^{-\mu_1 x_1 - \mu_2 x_2 \dots - \mu_i x_i} \quad (2.2)$$

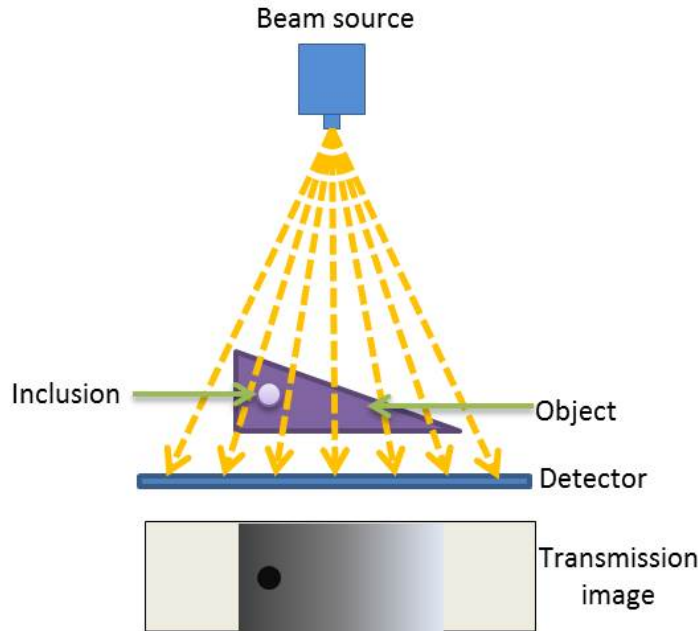


FIGURE 2.1: Illustration of radiography

## 2.2 In Situ NDE Experiment for RC Structures

### 2.2.1 Experiment set-up

Pillars of a berth pier constructed 40 years ago were inspected by 950keV Linac and Imaging Plate (IP) of FUJIFILM. According to prior information, there are several RC steel rebars of 22mm diameter casted in concrete which are located at 70mm height from the bottom. Other NDE methods were already used, however there is still no clear conclusion about the degradation situation of this structure due to lack of inner structure information. In particular, the exact defect position and situation are expected to be verified, as well as the overall evaluation about structure loading ability.

The devices are split and transported by vehicle to the field and then assembled. The X-ray emitter unit and RF unit is carefully carried down below the stage of the berth pier. Hanging shaft was put up in advance under the stage, on which the X-ray emitter unit and RF unit are installed and settled near the pillar. Lead sheet filter is

placed before IP to reduce scattered X-ray noise. A steel stick of 10mm diameter as reference sample is attached at the pillar bottom.

The X-ray beam is emitted as pencil beam of  $15^\circ$  angle. Due to the magnification effect, the quantitative evaluation of RC rebar diameter should be confirmed based on prior information and reference steel stick. The estimation method is explained in figure 2.3. The steel stick was placed in the perpendicular direction to the RC steel rebar during measurement. As a result, along the direction of steel stick, magnification ratio of the captured image is 1.15 times at the position of 50mm height, 1.3 times at the position of 100mm height, 1.45 times at the position of 150mm height. Then the diameter of RC rebar located at 70mm height can be estimated by this magnification ratio. Inspection is implemented at several positions and the radiation time for each image takes around 1 ~ 5min.

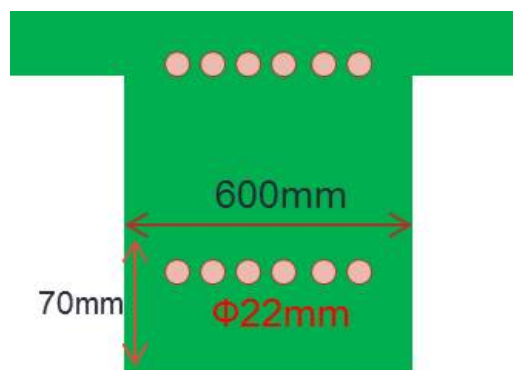


FIGURE 2.2: Experiment layout view

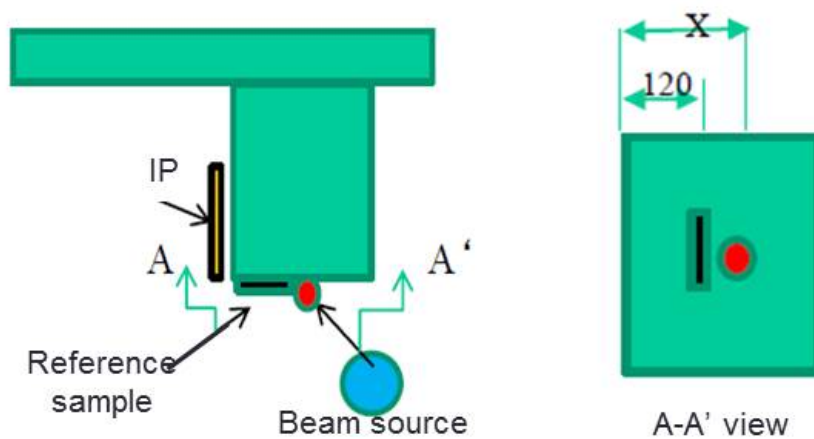


FIGURE 2.3: Magnification ratio

### 2.2.2 Results and discussion

Transmission images at two positions are given in figure 2.4 as examples. The red arrows indicated the RC steel rebar in the images. The red number showed the RC steel rebar with reduced diameter where thinning is estimated. According to overall evaluation in 3 different positions in several directions, the thinning situation of the structure is assessed. The diameter thinning is 6.3mm and the general reduction rate of cross-section area is around 7% ~ 14.5%. Further structural analysis based on the results is carried out by other experts and final evaluation conclusion and maintenance scheme are set up. According to the mechanical analysis and simulation, the structure would need reinforcement maintenance if the general thinning rate exceeds 30%. Hence, although aging and thinning indeed happened, the actual thinning situation still not reaches the dangerous level. The overall loading bearing ability of the whole structure is yet robust enough for continue application as long as necessary maintenance is applied, such as water proof. The quantitative evaluation result is very convincing and acceptable. Instead of initial plan about integral repair of the whole structure, new scheme is decided that only waterproof glue repair is necessary in several fixed positions. As a result, a large amounts of budget is saved.

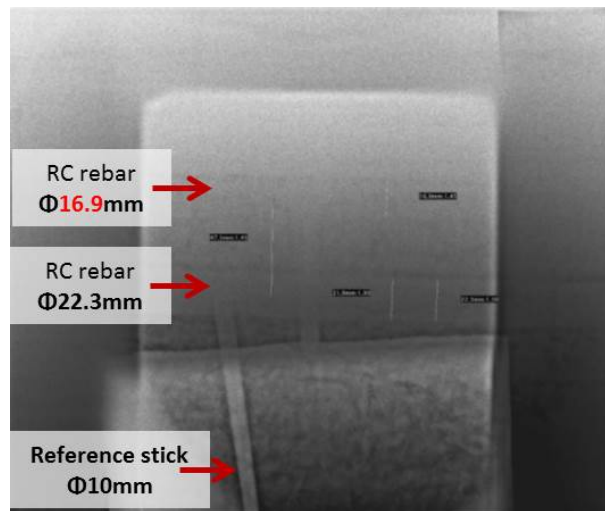
Besides, the experiment was implemented during midnight to avoid high tide period, in order to ensure enough working space below the stage of the berth pier. In spite of harsh environment of low temperature, strong wind and heavy rain, the transmission image is photographed successfully, which showed the advantages over other NDE methods which have high requirements about environment condition.

TABLE 2.1: Evaluation result of steel rebar thinning in RC structure

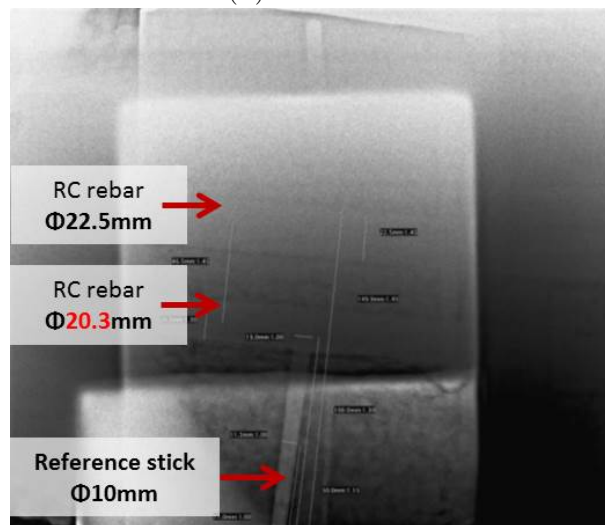
Position	A	B	C
Maximum thinning rate	8.7%	14.5%	7.0%
Maximum reduction (mm)	3.1	6.3	3.9

## 2.3 Quantitative Evaluation Methods for Steel Rebar Diameter Reduction

Considering in most circumstances, it's not possible to acquire prior information about inner structures, the quantitative estimation of inner rebar diameter reduction becomes difficult due to the magnification effects of pencil beam. Hence, the method



(A) Position A



(B) Position B

FIGURE 2.4: Transmission image of RC structure

of quantitative analysis by radiography imaging is proposed as one possible solution to this problem.

### 2.3.1 Quantitative analysis by radiography imaging

#### 2.3.1.1 Analysis principle

This simple quantitative analysis is proposed based on geometry of radiography imaging. The figure 2.5 showed the geometry of radiography imaging which are taken twice at the same detector position. The distance is changed  $\Delta L$  between the target and X-ray beam source. The most general and simple way is that the penile beam and the rebar share the same central axis. The detector is located at distance of  $L$  from

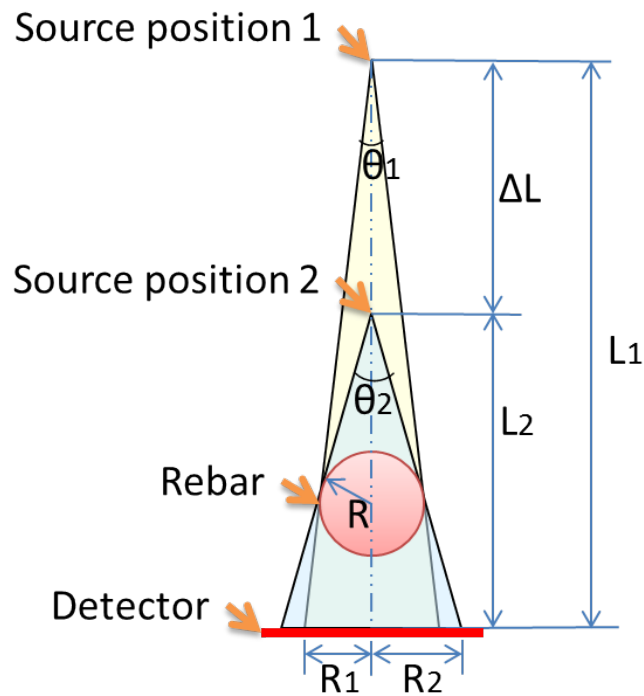


FIGURE 2.5: Quantitative analysis by radiography imaging

the source. Reading the radiography imaging from the detector, the radius of rebar presented in the images are  $R_1$  and  $R_2$ .

If the distance between center of rebar and source is  $D$ , apparently

$$D_1 - D_2 = \Delta L. \tag{2.3}$$

Then according to the triangle relationship, we have

$$\begin{aligned} \sin(\theta_1/2) &= \frac{R}{D_1} \\ \tan(\theta_1/2) &= \frac{R_1}{L_1} \end{aligned} \tag{2.4}$$

$$\begin{aligned} \sin(\theta_2/2) &= \frac{R}{D_2} \\ \tan(\theta_2/2) &= \frac{R_2}{L_2} \end{aligned} \tag{2.5}$$

so that the radius of rebar can be calculated:

$$R = \Delta L \left/ \left( \frac{\sqrt{L_1^2 + R_1^2}}{R_1} - \frac{\sqrt{L_2^2 + R_2^2}}{R_2} \right) \right. \tag{2.6}$$

### 2.3.1.2 Experiment validation

This method is validated by a test experiment. Small test sample is made by polyethylene with thickness of 40mm. It contains horizontal inner rebar made of aluminium with diameter of 3mm. The radiography imaging was taken by 50keV X-ray tube as beam source and small CCD camera as detector. The distance between beam source and detector are set as 100mm and 40mm respectively for two transmission images. The 3mm aluminium rebar is indicated in figure 2.6 by red arrow. The calculation result according to above equations are listed in table 2.2.

TABLE 2.2: Evaluation result of inner rebar radius

Real radius	1.5mm
$R_1$	1.00mm at $L_1 = 100mm$
$R_2$	1.27mm at $L_2 = 40mm$
$R$	1.549mm
Error	3.2667%

The result is very accurate and this method is validated to be reliable. however, during actual application, the geometry should be carefully designed to make sure the target can be reflected effectively and clearly in the imaging. Additionally, the accuracy would be influenced by the transmission image quality. The contrast is very critical to determine the precise radius in transmission image by identifying the edge of steel rebar, which is necessary parameter to deduce the real radius.

### 2.3.2 Imaging enhancement by tomosynthesis

When the transmission image quality is not very good, the vague boundary would make it difficult to confirm the diameter of rebar in the image accurately. As a result, the estimation of actual steel rebar diameter. Hence, the imaging enhancement to strengthen the edge is needed under such circumstance. Tomosynthesis is a novel solution to improve the image sharpness. In medical field especially breast cancer imaging or dental diagnose, slice imaging by tomosynthesis becomes a novel and popular method in recent years. [19] The application in industrial NDE field is just getting started. As indicated in figure 2.7, it only needs photography of several directions focusing on the to-be reconstructed thin planes.

One of the most fundamental algorithm to reproduce the plane image is Shift-and-add (SAA) method. Referring to figure 2.8, According to the position of difference

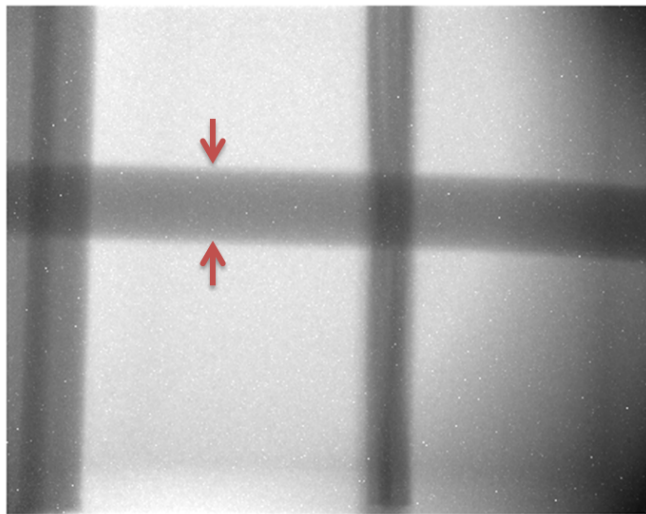
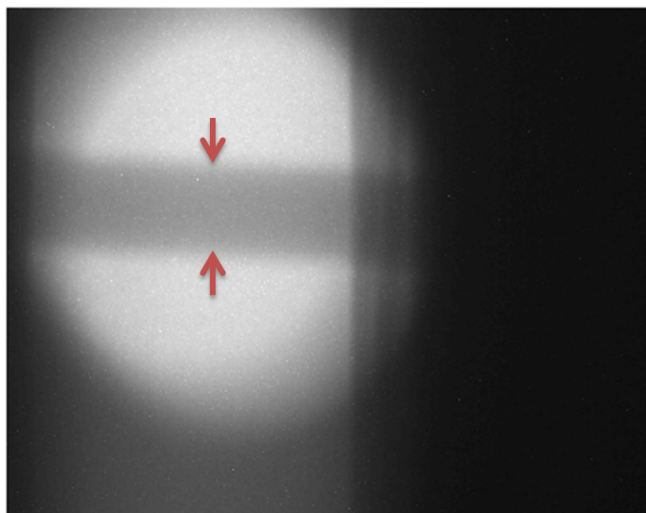
(A)  $L_1 = 100mm$ (B)  $L_2 = 40mm$ 

FIGURE 2.6: Transmission images of inner rebar

planes, the photos is shifted to focusing on the target plane and the shape of interiors is enhanced. Then synthesized image of the plane is acquired by added the re-focused photos. In spite of that the exact and full information of interior structure is still incomplete, details can be provided inside the thin plane. Specifically, focusing the thin plane at the inner rebar and synthesize the image, it is possible to provide image with sharp edge for the diameter estimation with just a few photography at several angles.

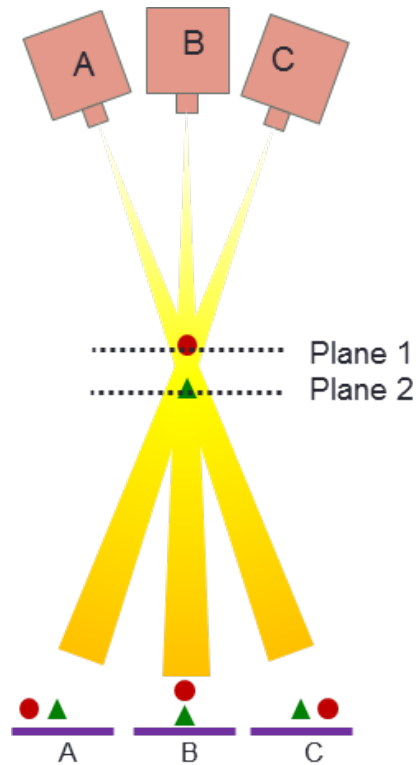


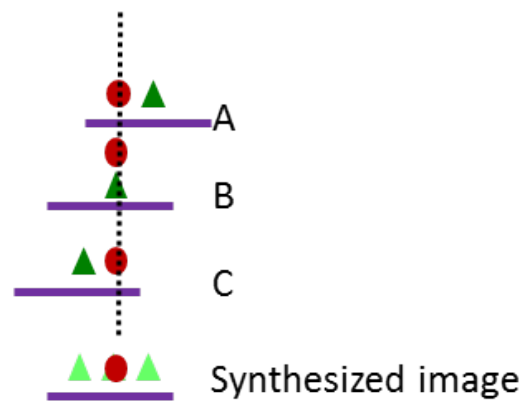
FIGURE 2.7: Tomosynthesis

## 2.4 In Situ NDE Experiment for PC Structures

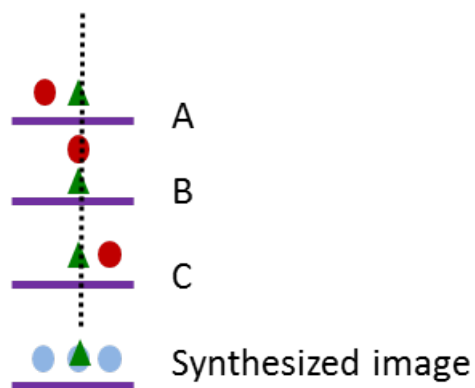
### 2.4.1 Experiment set-up

In order to further verify the in situ NDE experiment conditions, another experiment for PC structure is conducted in National Institute for Land and Infrastructure Management, Tsukuba, Japan. The specimens are repealed PC bridge girders with both embedded RC steel rebar and PC steel wires clusters. Seen from the end section of the specimen in figure 2.10, the radiography focuses on two parts: the upper part of the specimen with 150mm thick concrete which mainly contains RC rebars; and the flange part below with concrete thickness of 380mm where 10 bundles of PC wire clusters are embedded.

950keV Linac is installed in a large moving stage frame which is designed to realize horizontal and rotation motion as in figure 2.11. Detector can be installed on the other side of the stage and both FUJIFILM Imaging Plate (IP) and Flat Panel Detector (FPD) of Perkin Elmer are adopted in this experiment. For the IP, it's easy to control the image quality by adjusting radiation time but it's not convenient to read the data. The X-ray emission should be stopped after each photography to take back the IP and connect it to computer to read the data. FPD can be controlled remotely so that the photography



(A) Plane 1



(B) Plane 2

FIGURE 2.8: Shift-and-add (SAA) reconstruction

data is transmitted through cable and showed in the controlling screen in real time. But it's not easy to adjust the exposure condition because the controlling software fixes the radiation time to maximum of 1sec. A steel stick sample of diameter 19mm is attached before detector as reference.



FIGURE 2.9: PC structure

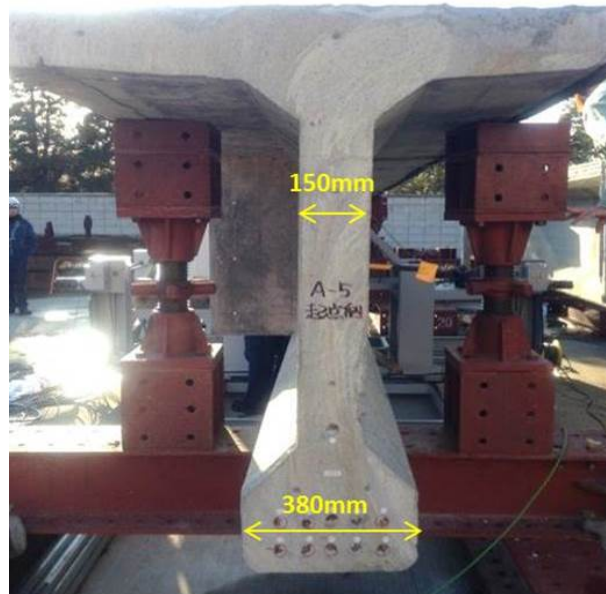


FIGURE 2.10: End section of PC structure



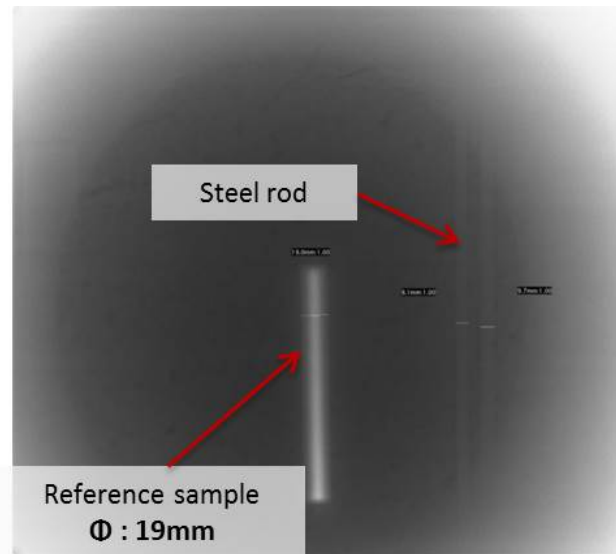
FIGURE 2.11: 950keV Linac on the stage frame



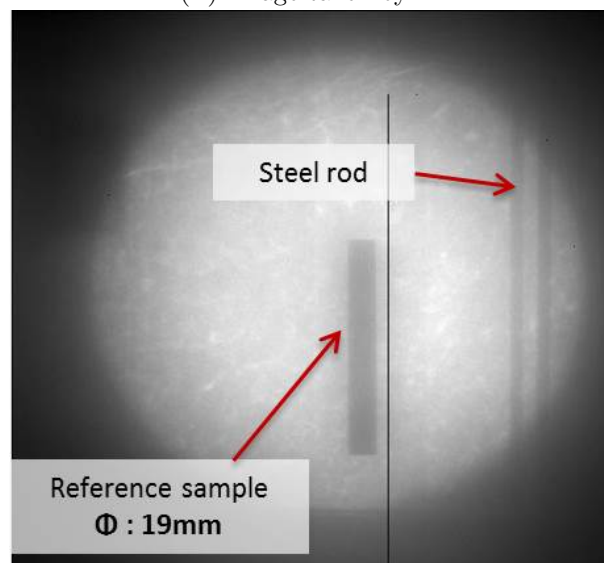
FIGURE 2.12: Detector on the stage frame

### 2.4.2 Result and discussion

Firstly, the upper part is photographed and images are showed in figure 2.13. IP takes 2min to get a clear image and two steel rebar is confirmed in the right. However, the diameter can't be estimated without prior information about the location depth. Clearer image is taken by FPD in just 1sec in the same position.



(A) Image taken by IP



(B) Image taken by FPD

FIGURE 2.13: Transmission image of RC rebar

Then the Linac and detector are lowered down to flange part and aimed at PC wire clusters. The penetration ability of X-ray beam is not enough for such thickness so that FPD couldn't get clear image in just 1sec. IP took 10min to get the clear image as figure

2.14. 4~5 wires appeared in the image but more overlapped ones are not distinguishable.

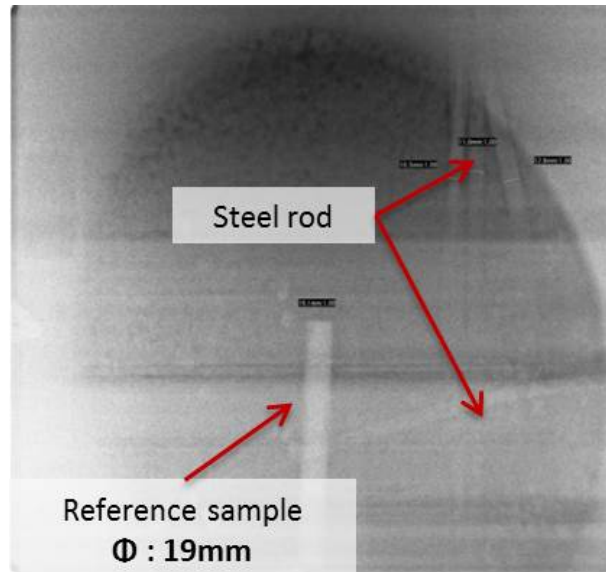


FIGURE 2.14: Transmission image of PC wire cluster taken with horizontal beam

Another shot was taken with Linac inclined by  $16^\circ$  to focus on the left bottom cluster of PC wires as explained in figure 2.16 and figure 2.15. However, wires become distorted and can hardly be identified as in figure 2.17 because the detector cannot be placed perpendicular to the beam due to limited space and the scattered X-ray noise effected the image quality.

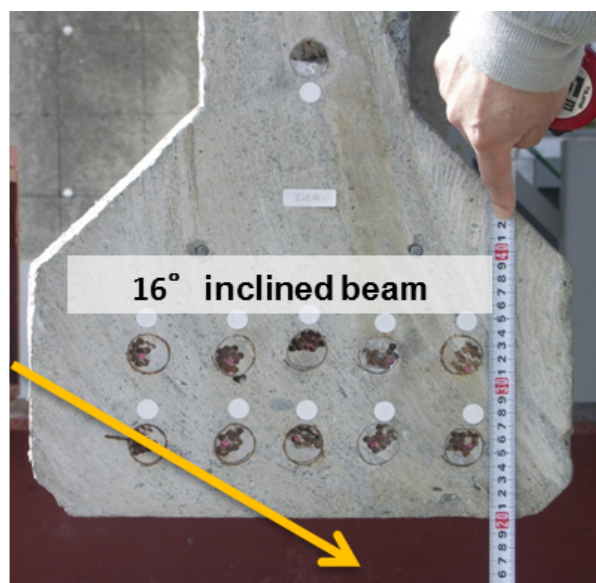


FIGURE 2.15: Inclined X-ray beam



(A) Inclined Linac



(B) IP under flange with lead cover

FIGURE 2.16: Linac and detector at inclined angle

In conclusion, PC steel wires are overlapped and very hard to distinguish in transmission image by simple Radiography. Therefore, evaluation for PC wires details by sectional image are expected to be realized through X-ray CT. To apply CT, we need:

- Higher energy

Rise penetration ability to get clear image at positions with thick concrete in a short time.

- Fast scanning speed of 1 2s per image

Rise efficiency of CT scanning when scanning over a certain angle range to acquiring projection data at different directions.

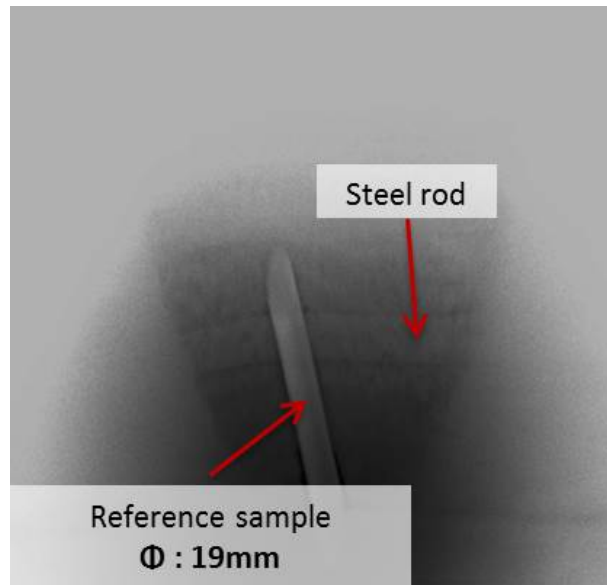


FIGURE 2.17: Transmission image of PC wire cluster taken with inclined beam

- Continuous detector

Rise efficiency of continuous scanning and keep constant beam condition. Detector with real time data transmission and remote control function is expected.

- Larger Inclined angle

Realize rotation scanning and acquiring enough scanning data from a certain angle range.

The higher energy level 3.95MeV Linac with stronger penetration ability is expected to work in situ for CT projection. FPD can realize continuous scanning and remote control. The improvement of rotation function is under discussion by reforming the stage frame.

### 2.4.3 Incomplete and truncated projection problems

Several constraints have been found during in situ experiments. Firstly, there is quite limited space around to install inspection devices. The system configuration should be carefully designed when work in field. Moreover, since bridge is very large scale structure with complex shape, as a result, full scanning is almost inaccessible and only partial scanning angle range is allowed. The possible scanning angle is approximately up to only 90° according to filed experience, which becomes very serious data missing problem compared with usual case of 180° scanning. Additionally, only limited region can be covered due to limited beam width and detector size and fewer projection views scanning is expected to control dose and save scanning time.

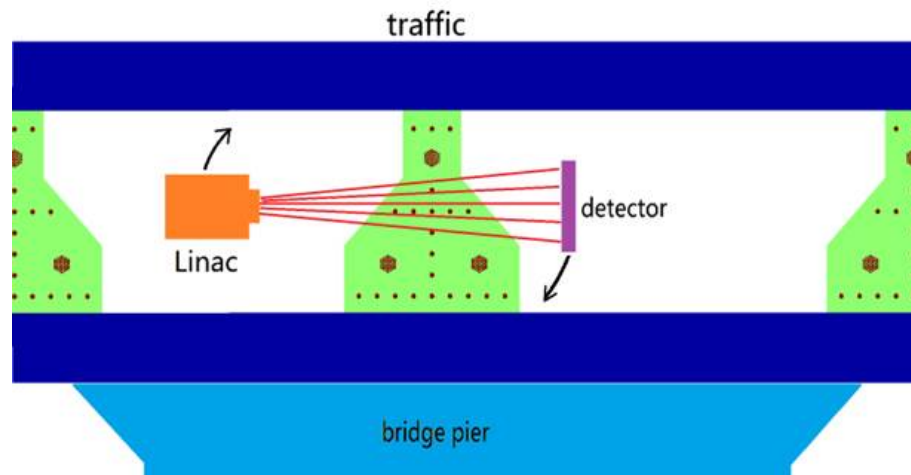


FIGURE 2.18: constraints of in situ inspection

In order to solve the above mentioned problems and realize in situ bridge inspection, countermeasures are considered. Firstly, scanning will be conducted with both rotation and translation to acquire as much data as possible by reforming the devices. Secondly, reconstruction with incomplete projection data will be optimized for better image quality. Thirdly, reconstruction algorithms will be developed for region of interest (ROI) inspection focusing on where inner steel wires are located.

## Chapter 3

# Simulation for Partial Computed Tomography

As mentioned in last chapter, the partial CT reconstruction problems are inevitable for in situ CT inspection of bridges. One of the most critical countermeasures is choosing the proper reconstruction algorithm. This chapter discussed the methodology of common CT and several improved algorithms which can recover missing information under incomplete projections and truncated projections.

### 3.1 Methodology of Computed Tomography (CT)

Computed Tomography(CT) is an effective method to provide interior information for Nondestructive Evaluation. As mentioned in last chapter, X-ray beam would be absorbed and scattered when penetrating an object and the variation of intensity can be described by the Beer-Lambert law. However, the simple radiography can only reveals the integral intensity difference along the whole beam path length, hence the details of each point inside the object is still unknown. when it comes to CT, further reconstruction can disclosure more information about the interiors based on radiography data around the object at a certain angle range. At a given slice, sectional image is reconstructed through back projection or solving inverse problem. As a result of that those projection information are rearranged to the sectional plane, each voxel of interior at this slice becomes obvious.

A typical CT application consists of the following three steps:

1. Projection at one direction

Measure the linear attenuation coefficient  $\mu$ , which reflects the x-ray intensity reduced by object material along the path between X-ray beam source and detector. Sample  $\mu$  at one direction to generate one projection view. The background is calibrated by detector reading under X-ray on and X-ray off situations. Usually CT can be categorized by system configuration of detector and beam geometry. Generally speaking, 3 types of CT configuration is common seen: parallel beam CT, fan beam CT or cone beam CT as showed in figure 3.1 and each type has appropriate detector such as 1D or 2D sensors. The reconstruction process would be adjusted according to the X-ray beam geometry character.

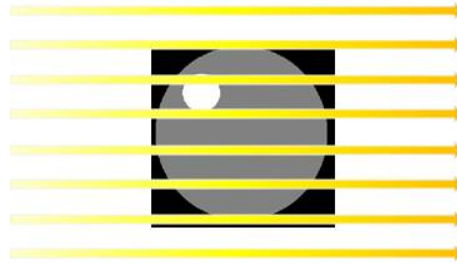
## 2. Projection around a certain angle range

Rotate and repeat last step to acquire projection in other directions, usually covering  $180^\circ$ . Both styles are Rotate the target object or rotate At a certain slice, there is one line of data corresponding to this slice plane in the projection view at one direction. Pick up this line of raw data at each projection view around the total angle range and arrange them into a 2 dimensional array, such that two coordinate axis represent the single line set of detector reading and view angle, which is called "sinogram". It contains all the information in this slice.

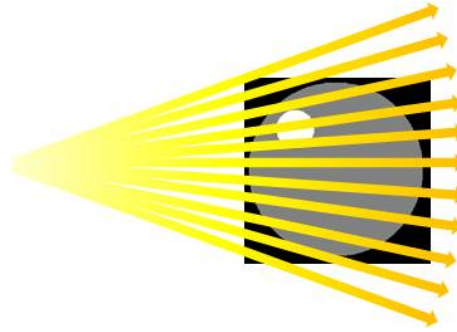
## 3. Reconstruction from sinogram

Smear back sinogram by each projection direction across the reconstructed image, which is actually reversing the measuring process to reconstruct a sectional image. The fundamental reconstruction algorithm is Filtered Back Projection (FBP) which is analytic method and most commonly used in commercial CT devices. Other algorithms like Algebraic Reconstruction Technique (ART) and Simultaneous Algebraic Reconstruction Technique (SART) are iterative methods.

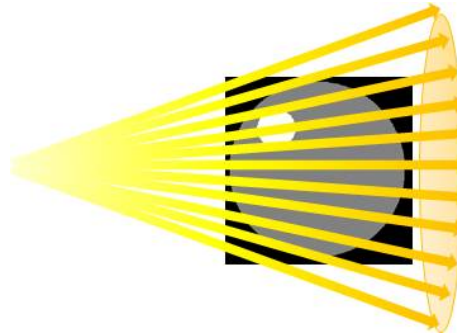
In the application for degradation bridge inspection, steel rods inside concrete can be detected through CT to clarify the erosion and soundness situation. However, due to large scale and complexity of bridge structure, several difficulties appeared, such as limited projection problem and truncation to projection data, as discussed in last chapter. Simulation studies are implemented to find proper algorithms for applying CT method to bridge NDE. The simulation is done under parallel beam situation with reconstructing of artificial phantom, which resembles specimen of bridge girder section slice. As showed in figure 3.2 there are several steel rods contained in the concrete in vertical or horizontal directions, as well as three clusters consists of 7 steel wires. For simplicity but without loss of generality, the simulation work adopts parallel beam. The conventional methods such as FBP, ART and SART are introduced and simulations with each method are tested with this phantom to reconstruct a  $256 \times 256$  image, followed



(A) Parallel beam



(B) Fan beam



(C) Cone beam

FIGURE 3.1: X-ray beam

with reconstruction by improved algorithms for partial and ROI problems. Besides the reconstruction images, profile of horizontal lines passing through steel wire clusters are compared, along with signal-noise-ratio (SNR) defined as

$$snr = 20 \log_{10} \frac{\| f \|}{\| f - f' \|} \quad (3.1)$$

where  $f$  is the real image of phantom,  $f'$  is the reconstructed image.

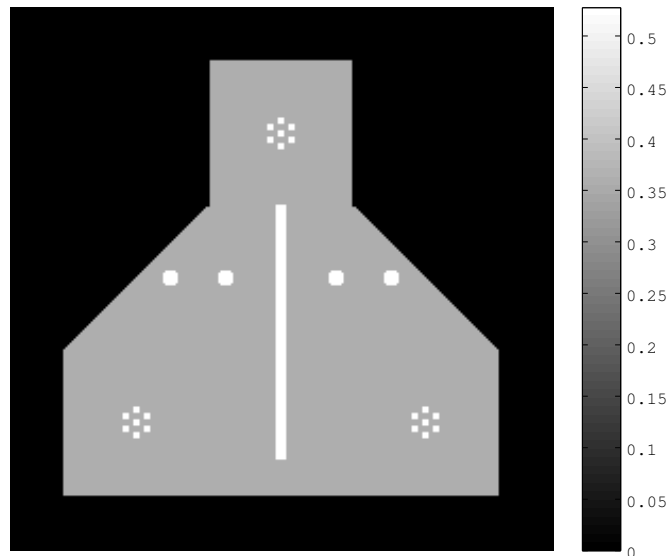


FIGURE 3.2: Simulation phantom

## 3.2 Fundamental Reconstruction Algorithms

### 3.2.1 Filtered Back Projection (FBP)

Currently the most widely used CT reconstruction algorithm is Filtered Back Projection (FBP). It's an analytic method derived from the X-ray transform function. The original function of real value is denoted by  $f(x, y)$  which represent the attenuation ability of each voxel at the sectional slice. The projection view data at each angle is denoted by  $p(\theta, r)$ . Define the Fourier transform of  $f(x, y)$  under polar coordinate system as  $F(\omega, \theta)$  then

$$f(x, y) = \int_0^{2\pi} \int_0^{+\infty} F(\omega, \theta) e^{j2\pi\omega(x \cos \theta + y \sin \theta)} \omega d\omega d\theta. \quad (3.2)$$

Considering that the path beam passing through at projection angle of  $\theta$  and  $\theta + \pi$  is symmetric as the same path but just opposite direction, use the property of

$$F(\omega, \theta + \pi) = F(-\omega, \theta)$$

then we have

$$f(x, y) = \int_0^{\pi} \int_{-\infty}^{+\infty} F(\omega, \theta) e^{j2\pi\omega(x \cos \theta + y \sin \theta)} |\omega| d\omega d\theta. \quad (3.3)$$

According to Fourier Slice Theorem, the one-dimensional Fourier transform of a

parallel projection is equal to a slice of two-dimensional Fourier transform of the original function. [20] This relationship is used in CT method to derive the original two-dimensional image from its one-dimensional projection. If the one-dimensional Fourier transform of  $p(\theta, r)$  is defined as

$$P_{\theta}(\omega) = \int_0^{+\infty} p(\theta, r) e^{j2\pi\omega r} dr,$$

then

$$F(\omega, \theta) = P_{\theta}(\omega). \quad (3.4)$$

Therefore, by performing a two-dimensional inverse Fourier transform with the given projection data, the original function can be recovered as following:

$$f(x, y) = \int_0^{\pi} \int_{-\infty}^{+\infty} P_{\theta}(\omega) e^{j2\pi\omega(x \cos \theta + y \sin \theta)} |\omega| d\omega d\theta. \quad (3.5)$$

Here the kernel

$$h(r) = \int_{-\infty}^{+\infty} |\omega| e^{j2\pi\omega r} d\omega$$

is ramp filter. [20, 21] With filtering process, FBP algorithm can effectively eliminate the stellate artifact caused by overlaying extra projection to originally empty voxel in simple back projection, which only back projects the projection data evenly to all voxels along the projection ray. However some errors may still be introduced due to discretization and model building.

Reconstruction of phantom in figure 3.2 with full projection data by FBP is given in figure 3.3. The inner steel rods and steel wire cluster are clearly presented. Some artifacts appeared slightly but it didn't affect the image quality very much.

### 3.2.2 Algebraic Reconstruction Technique (ART)

Different from analytic method, Algebraic Reconstruction Technique (ART) is an iterative method. This method uses estimate or prior information such as empty data or FBP reconstruction data as initial value, then it creates artificial raw data of projection or say, sinogram. The raw data is compared and corrected with real measured data until reaching a general rule. It approaching the original function by solving the inverse problem of

$$AX = b \quad (3.6)$$

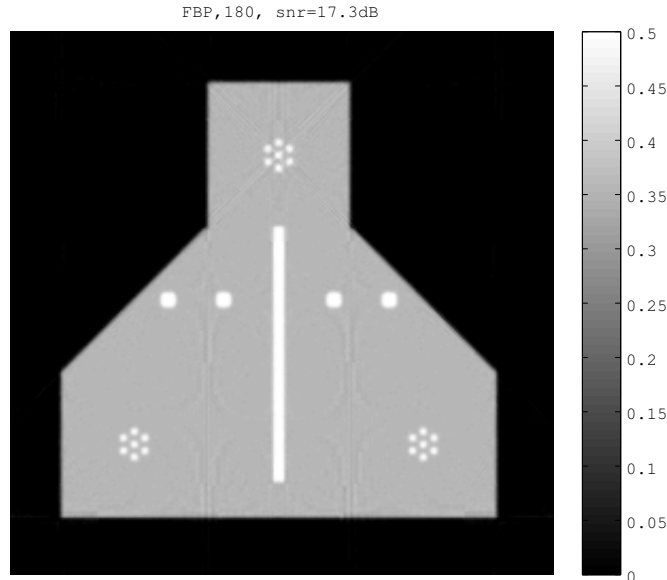


FIGURE 3.3: Reconstruction with full projection by FBP (SNR=17.3dB)

where  $X$  is the image to be reconstructed,  $A$  the matrix of projection path,  $b$  the projection data. The iteration procedure adopts Kaczmarz method: [20, 22–25]

$$x^{k+1} = x^k + \lambda_k \frac{b_i - \langle a_i, x^k \rangle}{\|a_i\|_2^2} a_i. \quad (3.7)$$

Since all projection data should be available before the iterative reconstruction starts and the reconstruction process is repeated several times, it costs quite large memory and long time to obtain the final imaging. Such kind of algorithm requires high demanding for computational hardware ability. [26] Although iteration methods are considered to be more robust to raw data with bad quality, it still not easy to find proper optimization pattern of the iteration process that is suitable for the specific situation.

Reconstruction with full projection data is given in figure 3.2.3. The interiors are quite distinctive and image SNR is superior than FBP. Some noise induced by iteration process is appeared in the image. The reconstruction takes several minutes as the loop was 100 and the calculation time extends when more loops are iterated. At the same time, noise induced during iteration would be more serious.

### 3.2.3 Simultaneous Algebraic Reconstruction Technique (SART)

Simultaneous Algebraic Reconstruction Technique(SART) is an advanced iterative method developed from Algebraic Reconstruction Technique(ART). It also approaching the original function by solving the inverse problem of equation . But for the solution of

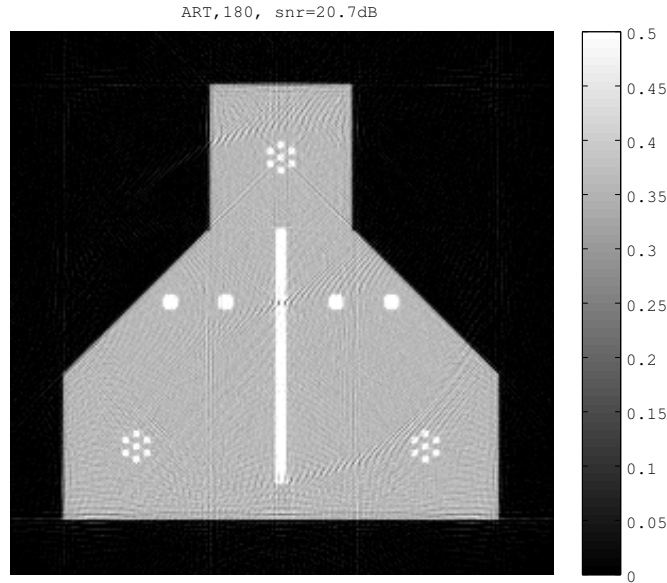


FIGURE 3.4: Reconstruction with full projection by ART (SNR=20.7dB)

inverse problem in each one iteration, all the equations is used simultaneously to correct errors in all ray-sum equations. This is why SART converges much faster than ART. The iterative procedure is as the following equation:[20, 22, 24, 27]

$$X^{k+1} = X^k + \lambda_k \frac{b - AX^k}{A \cdot A^{-1}} A^T. \quad (3.8)$$

Reconstruction with full projection data is given in figure 3.5. Image quality is much better than figure of ART and the SNR are improved further and the iteration noise is suppressed. calculation time by SART is between FBP and ART. Compared with analytic method FBP, although SART requires a little bit longer time and higher computational hardware ability due to iteration process, it can converge to real value more accurately. However the fast calculation speed of FBP is also a very crucial merit for in situ work and its image quality is not very bad. Both FBP and SART are better choice than ART and they are effective to provide reconstructed sectional image of good quality with full projection data.

### 3.3 CT Reconstruction of Incomplete Projection Problem

#### 3.3.1 Incomplete Projection Problem

In practical CT application, scanning covering 180° angle range is expected which contains full information of the target object. But sometimes, it's very difficult to

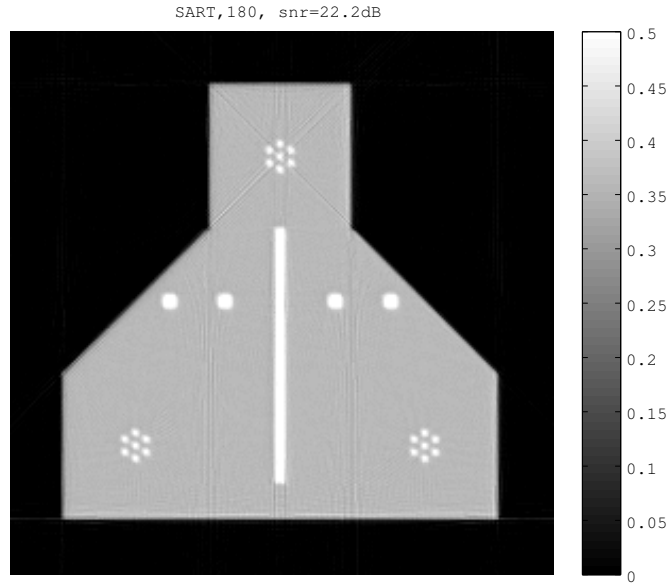


FIGURE 3.5: Reconstruction with full projection by SART (SNR=22.2dB)

acquiring full projection data because of several reasons, for instance, obstacles blocking on the beam path in some angle, small detector scale, constraints of exposure dose, limitation of scanning time, etc. When CT reconstruction is operated with projection view covering less than 180 degree or sparsely distributed, the problem became ill-posed and artifacts would appear in the sectional image due to missing information. Two of the common situations of such incomplete projection tomography are few projection views and limited angle range problems as indicated in figure 3.6. Few projection views problem means projection are sparsely taken at relatively large angle increment between each view in order to save time or reduce dose. Limited angle range problem happens often when some obstacle blocked the rotation in some angle that the projection data is inaccessible.

The two incomplete tomography situations are simulated with conventional reconstruction methods. As for few view problem,  $10^\circ$  was set as increment angle between each view and totally 18 views were used in reconstruction. In FBP image of figure 3.7a, severe artifact deteriorates image quality and affects evaluation about steel rods. In figure 3.7b of SART image, similar artifacts was generated and the interior information is also blurred due to lack of enough information. As for limited angle range problem, reconstruction was conducted using only  $0^\circ \sim 90^\circ$  projection data distributed with intensive increment of  $1^\circ$ . Around the angle where data was missing, bright shadow submerged the interior details in figure 3.8a reconstructed by FBP. In figure 3.8b, SART showed a little recovery ability of missing projection information through iteration process to some extent, but influence still exists on internal details and boundaries by artifact and

shadow. For the purpose of improving image quality, improved algorithm is proposed for reducing artifacts and shadows under such incomplete tomography situations.

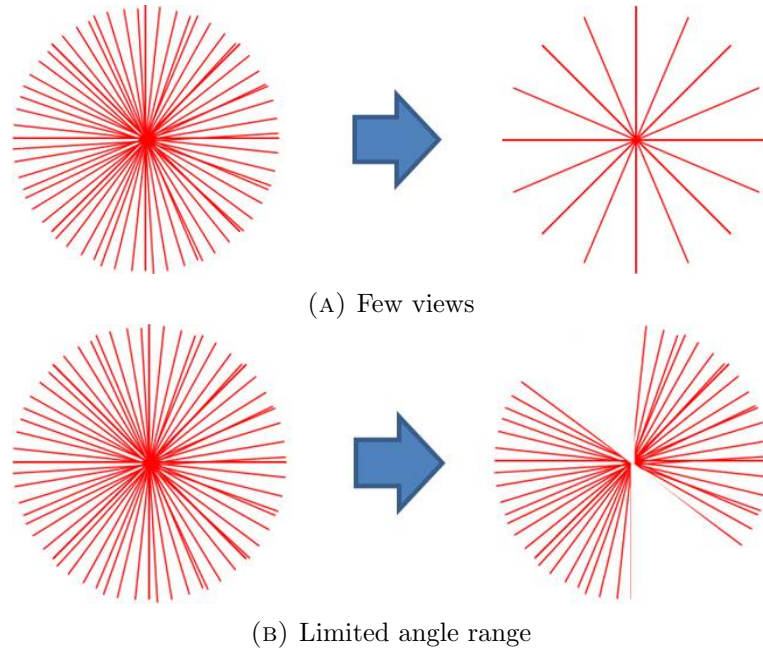
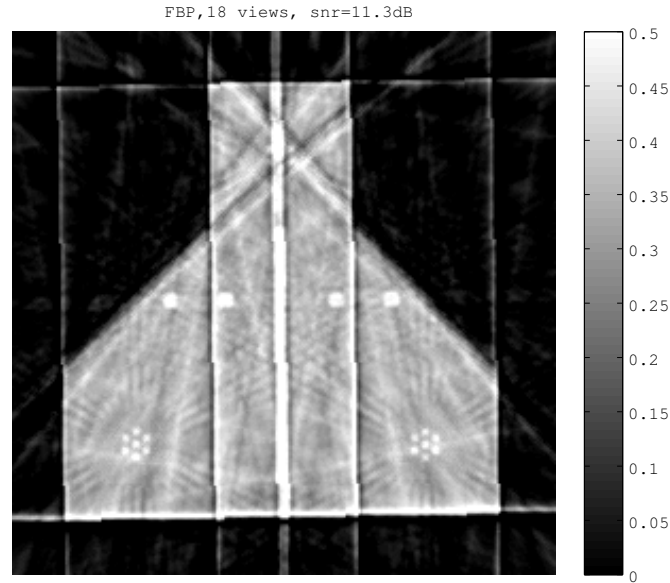


FIGURE 3.6: Incomplete projection tomography

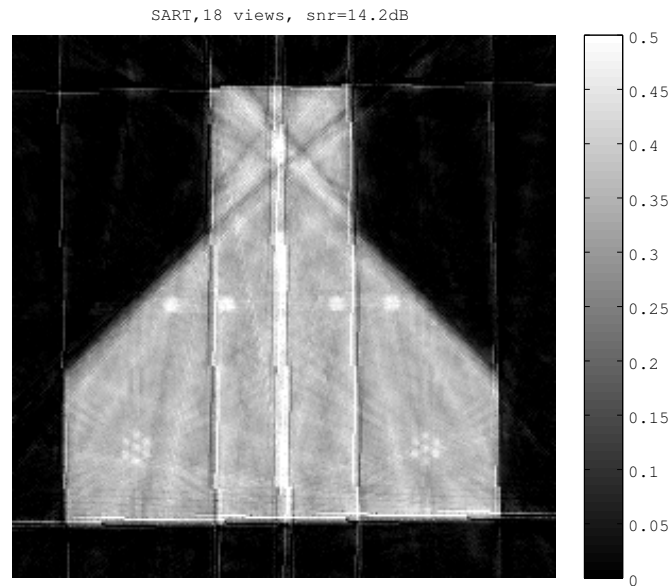
### 3.3.2 SART with Total Variation (SART-TV)

Many researchers around the world are studying the solutions for incomplete CT reconstruction but little improvement is seen and the problem is considered to be too ill-posed. In recent years as the idea of Compressed Sensing theorem application on CT set up by Candes et al. [28] become popular, people began to re-examine the possibility and quality of original signal recovery with sparse sampling. Based on such theory, the original idea of SART-TV is firstly proposed by Sidky in 2006, [29] combined iterative method with Total Variation minimization. Generally, according to the conventional Nyquist-Shannon sampling theorem, band limited images can be reconstructed if the sampling rate at least doubles the highest frequency of nonzero magnitude. While Compressed Sensing theorem finds solutions for reconstruction with under sampled data, that high-quality images can be recovered from far less measurements than Nyquist-Shannon sampling theorem. [28, 30, 31] In an appropriate orthonormal system, most signals are sparse, mostly close or equal to zero. Candes et al. proposed that if taking the magnitude of the image gradient as the sparsifying transform, which is called Total Variation (TV) term as  $\|f\|_{TV}$  denoted in the following equation

$$\nabla f_{x,y} = \sqrt{(f_{x,y} - f_{x-1,y})^2 + (f_{x,y} - f_{x,y-1})^2} \quad (3.9)$$



(A) FBP (SNR=11.3dB)



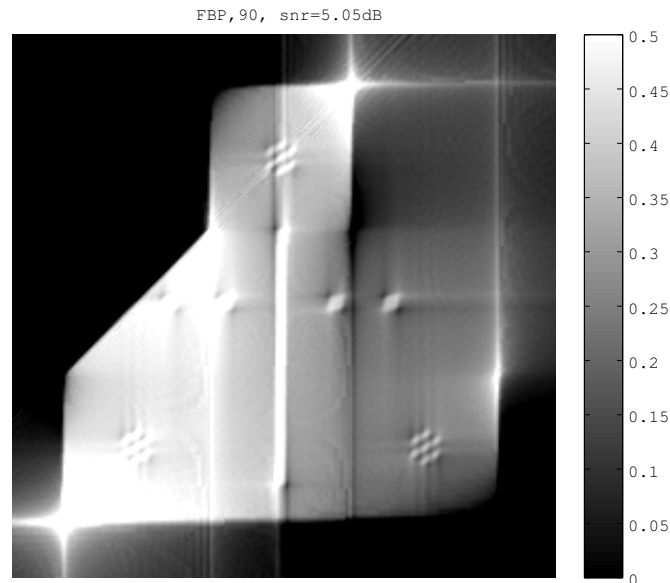
(B) SART (SNR=14.2dB)

FIGURE 3.7: Few view problem ( $10^\circ$  increment)

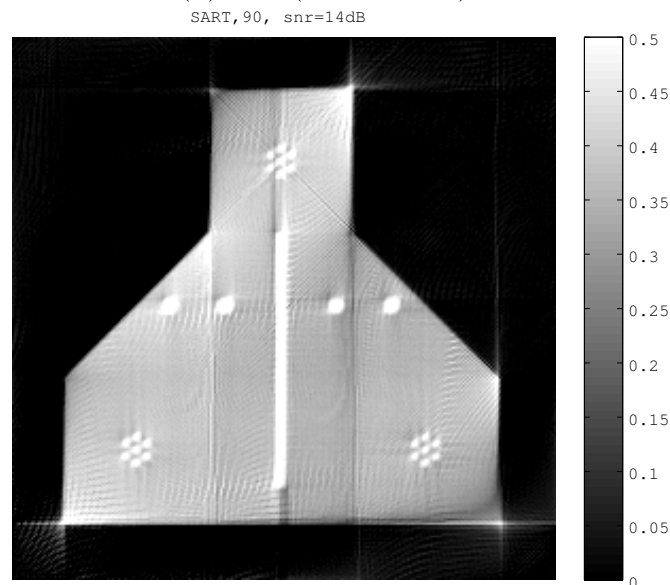
$$\|f\|_{TV} = \|\nabla f\|_1 = \sum_{x,y} |\nabla f_{x,y}|, \quad (3.10)$$

the real image becomes approximately sparse. [28] In spite of using incomplete sampling, the reconstruction method with TV regularization they proposed can recover CT images by solving the optimization procedure of

$$\min \|\nabla f\|_1, \quad \text{subject to } Af = p \quad \text{and} \quad f > 0, \quad (3.11)$$



(A) FBP (SNR=5.05dB)



(B) SART (SNR=14dB)

FIGURE 3.8: Limited angle range problem(90°)

Where  $A$  is the CT projection matrix,  $p$  is the measured projection sampling. [32–35] More developments are made by other researchers to further reduce blurring through adding prior information or weighting functions. [36, 37] The process of SART-TV algorithm consists of the following steps in one loop:

1. Initialization:

Setting up iteration parameters and initial threshold.

2. SART reconstruction:

Solving the inverse problem of  $AX = b$  by iterative process of SART algorithm;

3. Positive constraint:

Eliminating negative values in reconstructed image;

4. TV optimization:

Solving the minimization procedure of TV term for the image by gradient descent method to find the optimized image;

5. Stopping criteria:

Evaluating the error between image of this loop and last loop to determine whether to stop iteration;

6. Initialize next loop:

Taking the optimized image after TV minimization as the initial data for SART loop and starting from the second step again.

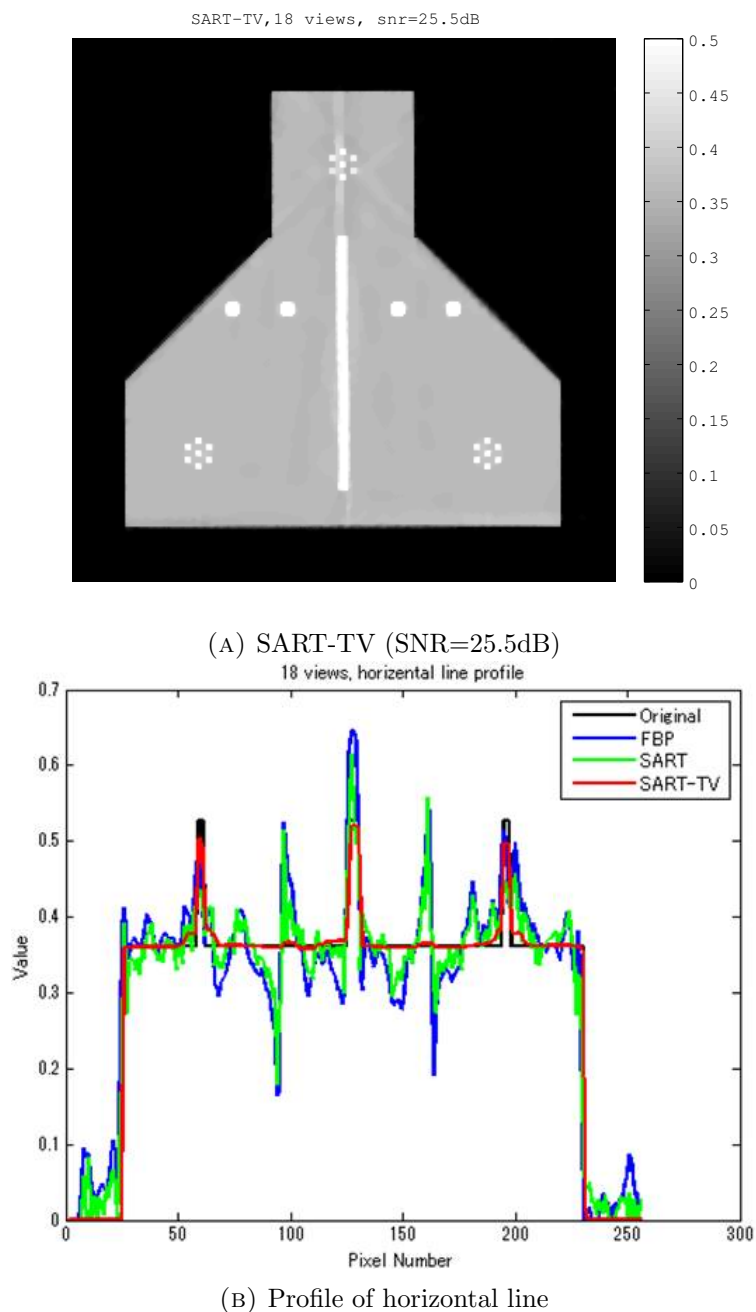
### 3.3.3 Simulation and discussion

In simulation results of figure 3.9a and figure 3.10a are reconstructed by SART-TV under the same situation of figure 3.7 and figure 3.8 respectively. Reconstruction figures are given as well as profiles along the horizontal line located at steel wire cluster of the images in figure 3.9b and figure 3.10b. Compared with FBP and SART results, the SART-TV algorithm can reach much higher SNR and effectively recover the missing data as well as eliminate the artifacts and shadow. In few view problem, line artifacts along missing angle direction is eliminated perfectly. In limited angle range problem, only a slight subtle shadow left near the object edge and the interiors are presented beautifully. With more iteration loops, the result can be further improved in the cost of time-consuming.

## 3.4 CT Reconstruction of Region of Interest (ROI)

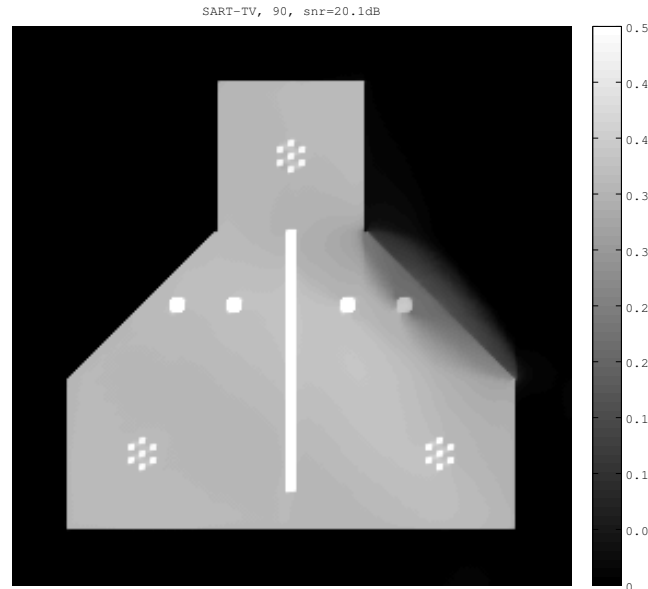
### 3.4.1 Truncated Projection Problem

When obstacles exist at projection lines or the sample is too large for the detector to cover the whole object, the projection data will be truncated. Such situation happens commonly in industrial CT. It may also occur in medical diagnostic imaging focusing on just tumor. Truncation problem is another kind of incomplete tomography, different from the few view or limited angle range problem. It suffers severe sparse information

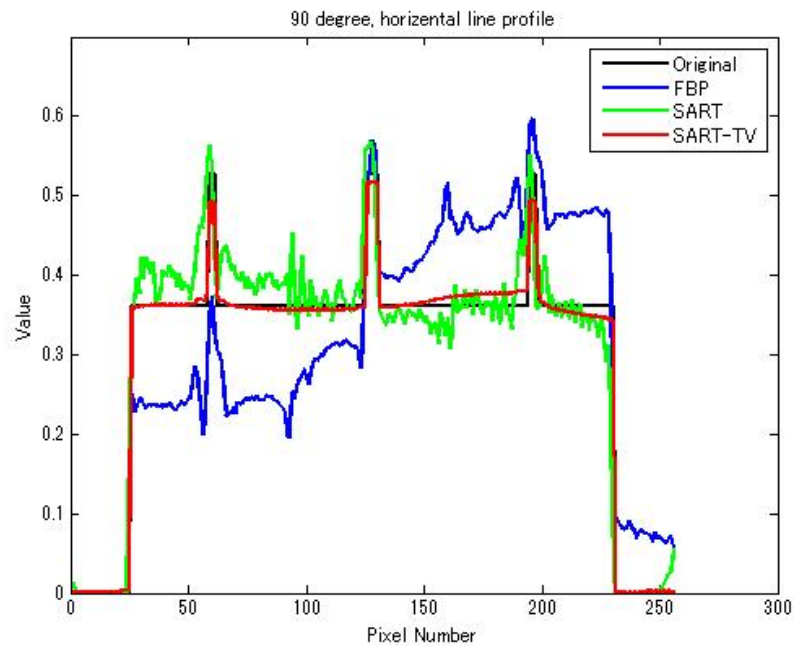
FIGURE 3.9: Comparison of few view problem ( $10^\circ$  increment)

and almost unrecoverable when reconstruction the whole sectional image. However for several specific truncation situations, some limited region in the section can still be precisely reconstructed, which is very meaningful and useful as long as the Region of Interest (ROI) is within this region.

During in situ inspection for large scale structures like bridge, it's almost impossible to collect full projection data. Take the bridge girder phantom as example in figure 3.11, focusing on PC steel wires, when the detector can only cover half of the common scan range instead of the whole phantom, except the region inside the yellow circle, projection



(A) SART-TV (SNR=20.1dB)



(B) Profile of horizontal line

FIGURE 3.10: Comparison of limited angle range problem( $90^\circ$ )

of other part would be truncated. [38] The method of Differentiated Back projection-Hilbert Transform(DBPH) proposed by Noo in 2004[39] as a analytic method can exactly reconstruct ROI inside the object in certain cases. Iterative methods like SART-TV also holds ability to recover the image. Both methods are tested with our phantom under the truncation situation of figure 3.11.

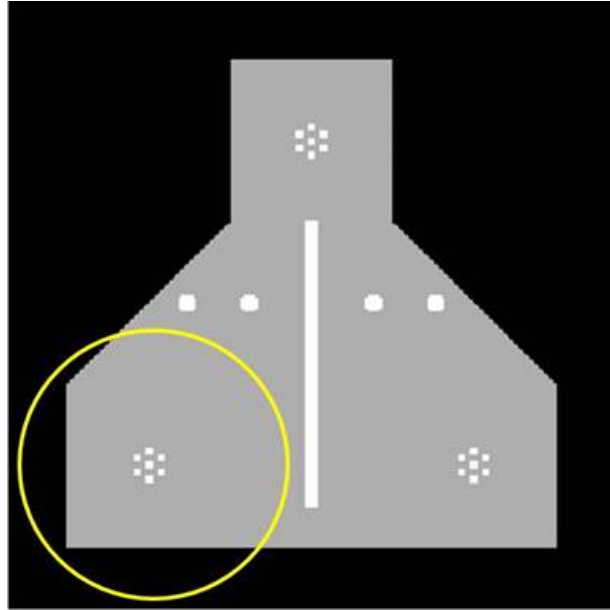


FIGURE 3.11: Truncation geometry of ROI problem for bridge inspection

### 3.4.2 Differentiated Back Projection with Hilbert Transform (DBPH)

When truncated projection data are reconstructed by conventional FBP, the ramp filtering operates through the entire projection and then errors caused by missing data would damage the whole image, including the ROI where the projection may not be actually truncated at all. [40] Differently, in DBPH algorithm the reconstruction process happens not over the whole image but along the so-called Hilbert lines independently. The conditions for exact reconstruction require that each point inside ROI should belong to at least one Hilbert line; and for each Hilbert line, at least one end point should be outside the object support. [39] There are some typical standard truncation geometries with Hilbert lines indicated in figure 3.12 that can fulfill these conditions. For our ROI reconstruction problem of figure 3.11, it satisfies the conditions in the category of figure 3.12b and the Hilbert lines are chosen at  $\theta = 0$  as in figure 3.13.

Firstly, derivatives of projections are taken to back project a Hilbert image:

$$p(r, \phi)' = \partial p(r, \phi) / \partial r \quad (3.12)$$

$$g_{\theta}(x) = -\frac{1}{2\pi} \int_0^{\pi} \frac{\partial}{\partial r} p(r, \phi) \operatorname{sgn}(\sin(\phi - \theta)) d\phi \quad (3.13)$$

Here  $p(r, \phi)$  is projection data and  $\operatorname{sgn}(x)$  is

$$\operatorname{sgn}(x) = \begin{cases} 1, & \text{if } x > 0 \\ 0, & \text{if } x = 0 \\ -1, & \text{if } x < 0 \end{cases} \quad (3.14)$$

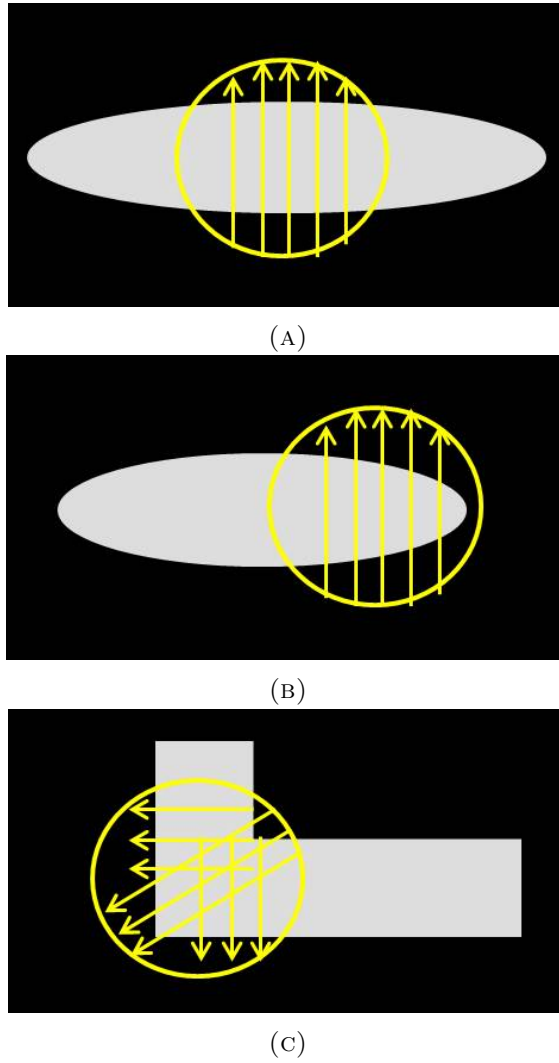


FIGURE 3.12: Standard truncation geometries

The  $g_\theta(x)$  is called Hilbert image, which is just the Hilbert transform of  $f(x)$  indicated by  $H_\theta f(x)$ , along each Hilbert lines within range  $[L, U]$ :

$$\begin{aligned} g_\theta(x) &= H_\theta f(x) \\ &= \frac{1}{\pi} \mathbf{p.v.} \int_L^U \frac{1}{x-s} f(x) ds. \end{aligned} \quad (3.15)$$

The  $\mathbf{p.v.}$  denotes the Cauchy principle value of integral and  $s = x \cdot (-\sin \theta, \cos \theta)$ . Then the Hilbert transform technique is used to recover the true image from Hilbert iamge:

$$f(x) = \frac{-1}{\sqrt{(x-L)(U-x)}} \left( \int_L^U \sqrt{(s-L)(U-s)} \frac{Hf(s)}{\pi(x-s)} ds + C \right) \quad (3.16)$$

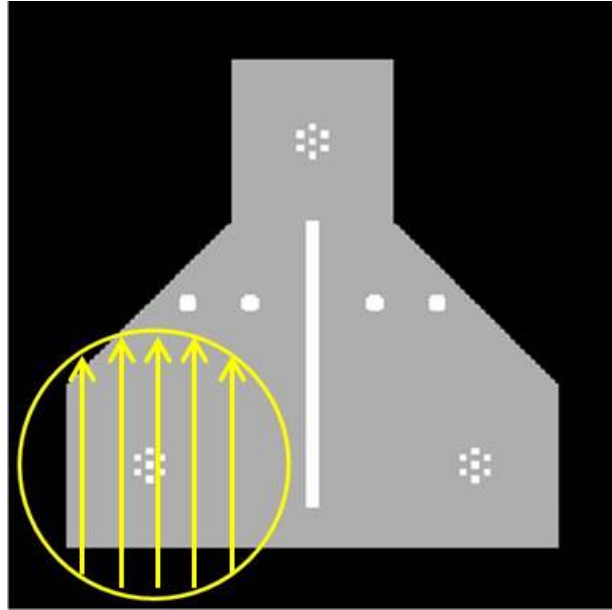


FIGURE 3.13: Hilbert lines of ROI problem for bridge inspection

At the  $t_{th}$  Hilbert line, for  $s \in [L_t, L_t + \varepsilon_t] \cup [U_t - \varepsilon_t, U_t]$  where  $f(x) = 0$ , the constant  $C_t$  can be calculated:

$$C_t = - \int_{L_t}^{U_t} \sqrt{(s - L_t)(U_t - s)} \frac{Hf(s)}{\pi(x - s)} ds. \quad (3.17)$$

The advantage of this method is that if some projections are truncated, at least other part of the reconstructed image can stay unaffected. Because for the complete projections, their derivatives still can be taken without effect from other part. [39, 40] The procedure for DBPH reconstruction is as the following:

1. Verify the problem geometry:

Determine the region that won't be affected by the truncation according to the geometry and identify the direction of the Hilbert filtering at angle  $\theta$ ;

2. Calculate differentiated term:

Take differentiated term of projection data of each view for all the accessible data;

3. Generate the Hilbert image:

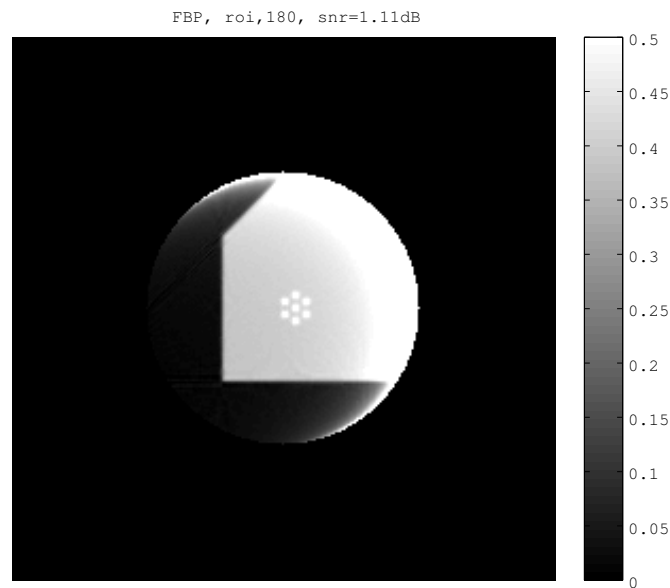
Use the simple Back Projection method with the differentiated projection to get the Hilbert image, and the Hilbert transform of real image is obtained;

4. Get the True image:

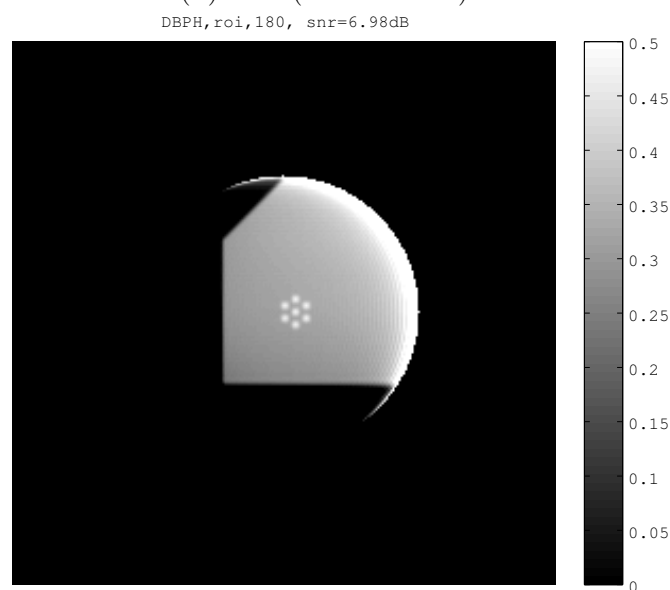
Take inverse Hilbert transform along each line of the Hilbert image at  $\theta$  direction to recover the real image.

### 3.4.3 Simulation and discussion

Both direct methods of FBP and DBPH are used to reconstruct with truncated projection as figure 3.11 indicated, and region constraint is added in the final image to compare only the ROI quality. The results in figure 3.14a showed that in the image reconstructed with FBP, large area of bright color appeared near edge of ROI due to truncation. As showed in figure 3.14b, DBPH can provide higher SNR and better image quality with much less artifact. The steel rod cluster in the center of ROI is clearly presented without any effect by truncation.



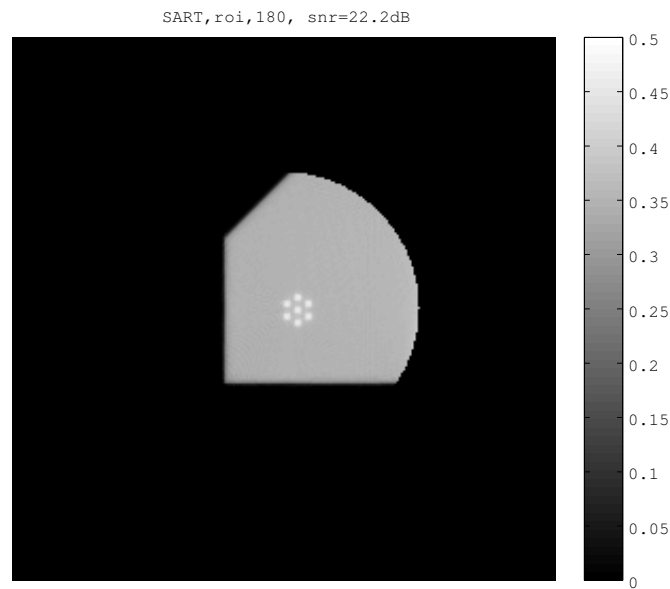
(A) FBP (SNR=1.11dB)



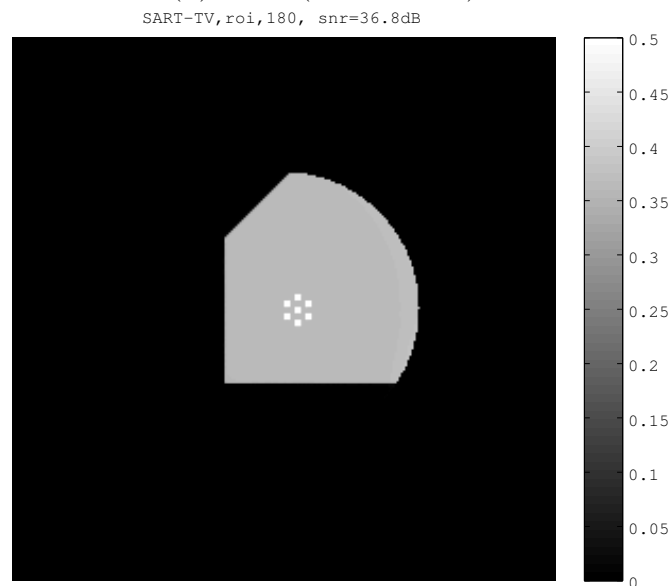
(B) DBPH (SNR=6.98dB)

FIGURE 3.14: Reconstruction for ROI by analytic methods

Similar simulation was taken with SART and SART-TV to verify the recovery ability to truncation through iteration in figure 3.18. The results indicate that the ROI are precisely reconstructed with very little shadow artifact, especially in SART-TV reconstruction. Further comparison of those methods in profile of horizontal line in reconstruction image are given in figure 3.16. In general, FBP and DBPH costs the least time, SART-TV the longest; while the SART-TV gives the most precise reconstruction for ROI, then SART, followed by DBPH, and finally FBP.



(A) SART (SNR=22.2dB)



(B) SART-TV (SNR=36.8dB)

FIGURE 3.15: Reconstruction for ROI by iterative methods

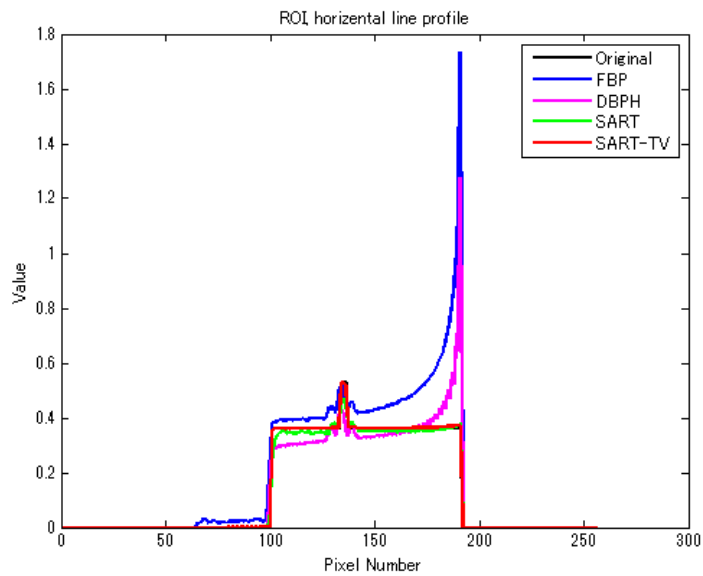
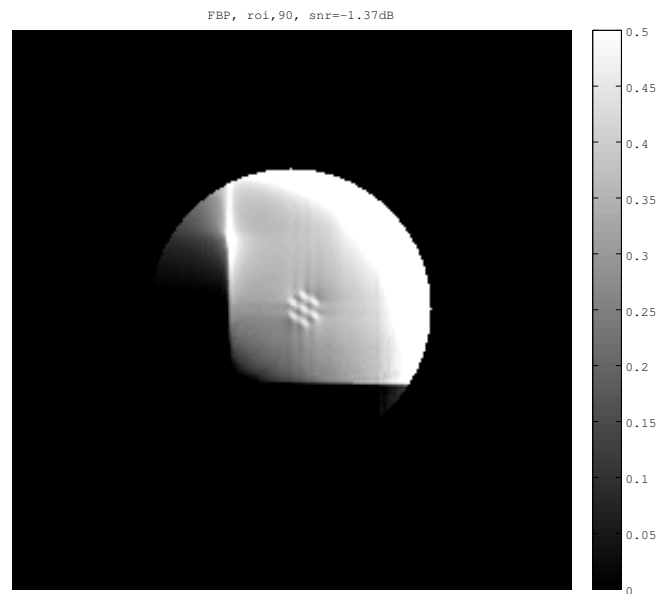
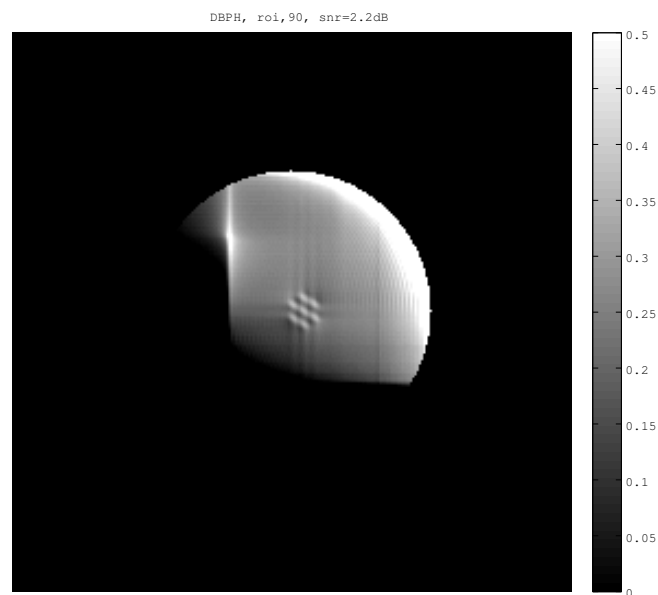


FIGURE 3.16: Profile of horizontal line in ROI reconstruction image

Further simulation work is implemented with those methods for ROI with limited angle range, which might happen during in situ inspection for bridges when it's necessary to reduce scanning time or irradiation dose. As showed in figure ?? and figure ??, the image quality is blurred and shadow deteriorates steel wires and phantom edge. Even for calculation with SART-TV, the recovery ability is very limited and error happened as the profile data indicated in figure 3.19. In order to solve the problem that holds both incomplete projection conditions and truncation problem, more other countermeasures are necessary because the lack of information is too serious to be recovered by just simply improving reconstruction algorithm. For example, adding some prior information may help reduce the uncertainty.

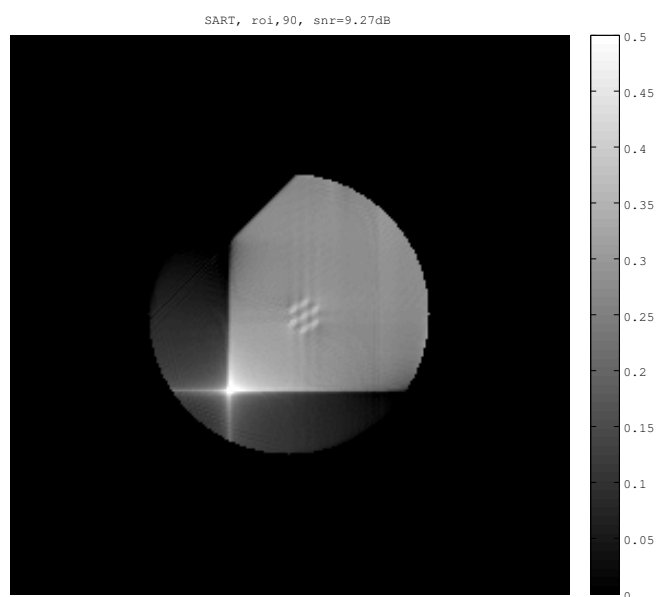


(A) FBP (SNR=-1.37dB)

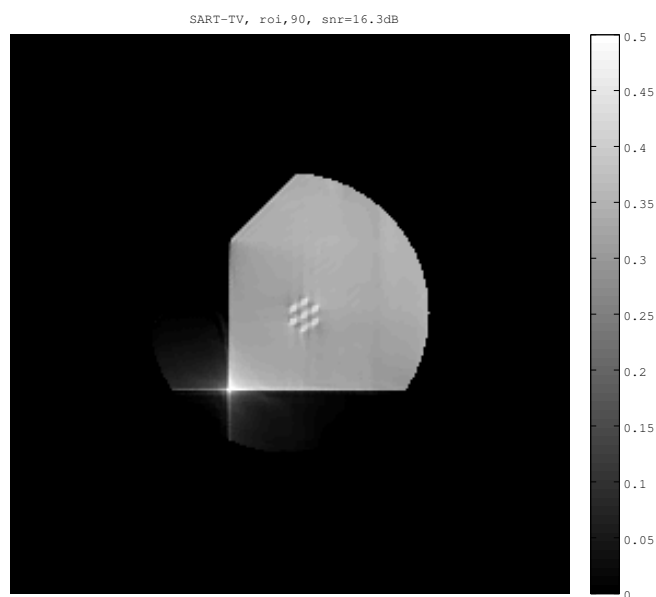


(B) DBPH (SNR=2.2dB)

FIGURE 3.17: Reconstruction for ROI with limited angle range problem( $90^\circ$ ) by analytic methods



(A) SART (SNR=9.27dB)



(B) SART-TV (SNR=16.3dB)

FIGURE 3.18: Reconstruction for ROI with limited angle range problem( $90^\circ$ ) by iterative methods

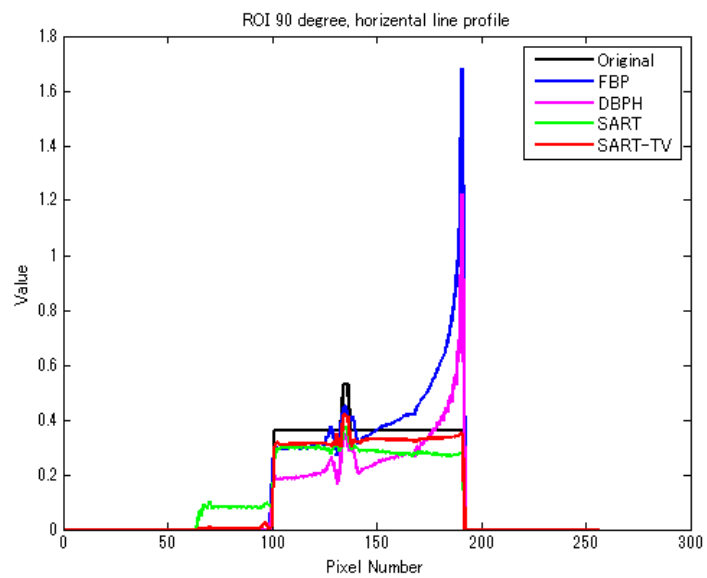


FIGURE 3.19: Profile of horizontal line in ROI reconstruction image with limited angle range problem( $90^\circ$ )

## Chapter 4

# Computed Tomography Experiment for Incomplete Projection Problem

In order to develop a CT system suitable for inspection of concrete material with inner steel rods, a testing system using Linac as beam source was designed and built in laboratory to conduct CT experiment in the first place. This chapter discusses the overall set up of the system and the primary performance of the experiment as well as CT reconstruction image quality with full or incomplete projections..

### 4.1 Test with Commercial CT Device

At the beginning, test experiment is done as reference with a commercial CT system in RIKEN, Japan. The Y.CT Compact is a CT device produced by YXLON, which adopts 450keV X-ray tube as beam source. A line detector and a metal filter is equipped in the device. There is a test platform for installation of specimen and the platform are combined with a stage which can move vertically and rotationally. All those components are assembled in big container. The maximum inspection envelope is limited to  $450mm \times 750mm$  and the sample should be no more than 50kg weight. Therefore, only specimen with small scale which can fit into the envelope would become the possible target. Such a compacted device cannot work in situ for bridge inspection.

The test for acquiring reference information is implemented with a small concrete sample containing inner steel rods. The sample is a 100mm height cylinder with diameter of 100mm as indicated in figure 4.2. For comparison, a battery, a aluminium cylinder



FIGURE 4.1: Y.CT Compact CT device of YXLON

TABLE 4.1: Specifications of Y.CT Compact CT device of YXLON

CT mode	Fan beam CT
Max. inspection envelope	450mm × 750mm
Max. sample weight	50kg
X-ray source	Y.TU450-D11 0.4mm@0.7kW/1.0mm@0.5kW
Detector	Y.LineScan 254μm Pitch
Min. scan time	15s per slice
Cabinet size( $W \times H \times D$ )	185 × 180 × 230cm
Cabinet weight	10t

and a iron cylinder is attached to the top of the concrete sample. Two steel rods of 8mm diameter are embedded inside, in the flat and inclined direction respectively.

Projection data was taken every 1° over 180° range and at each angle, it costs 15sec to acquire the projection. The built-in software automatically accomplished subsequent treatment and analysis. Sectional slice images are reconstructed every 10mm height and 3D model are built by stacking all the slices. The transmission in figure 4.4 provide the transparent image of X-ray passing through the object in a certain direction. Details in section slices are reflected in CT images given by figure 4.5. The inner structures are very clearly represented that the battery inner core, steel rod, stone, cement and voids are all distinguished with apparent contour. This result is referred in later study.

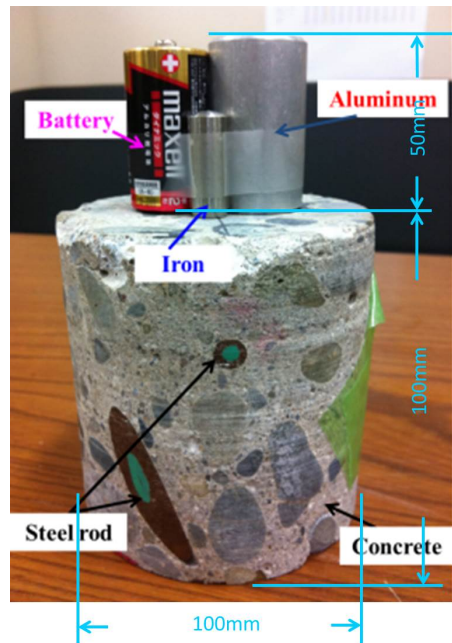


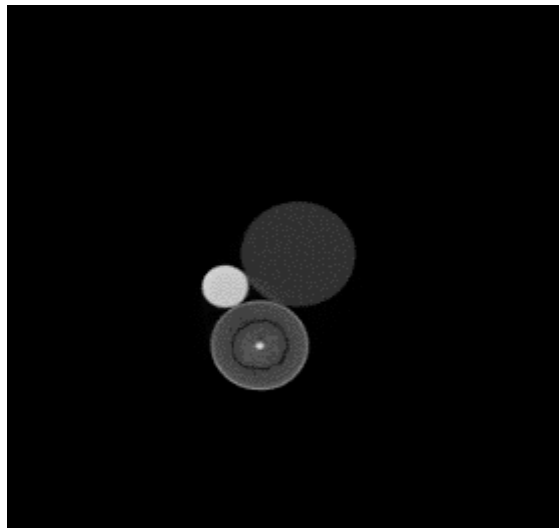
FIGURE 4.2: Small concrete sample



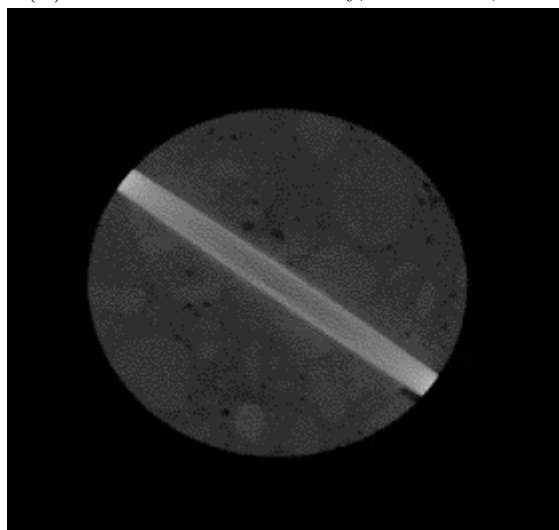
FIGURE 4.3: Small concrete sample in compact CT device



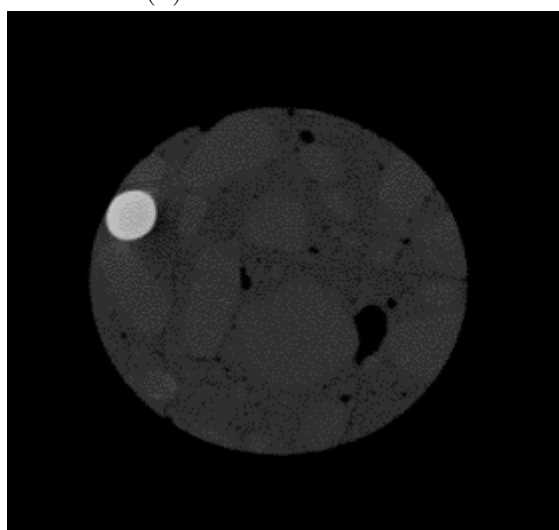
FIGURE 4.4: Transmission image of small concrete sample by compact CT device



(A) Slice of attached battery, aluminum, iron



(B) Slice of flat steel rod



(C) Slice of inclined steel rod

FIGURE 4.5: CT image of small concrete sample by compact CT device

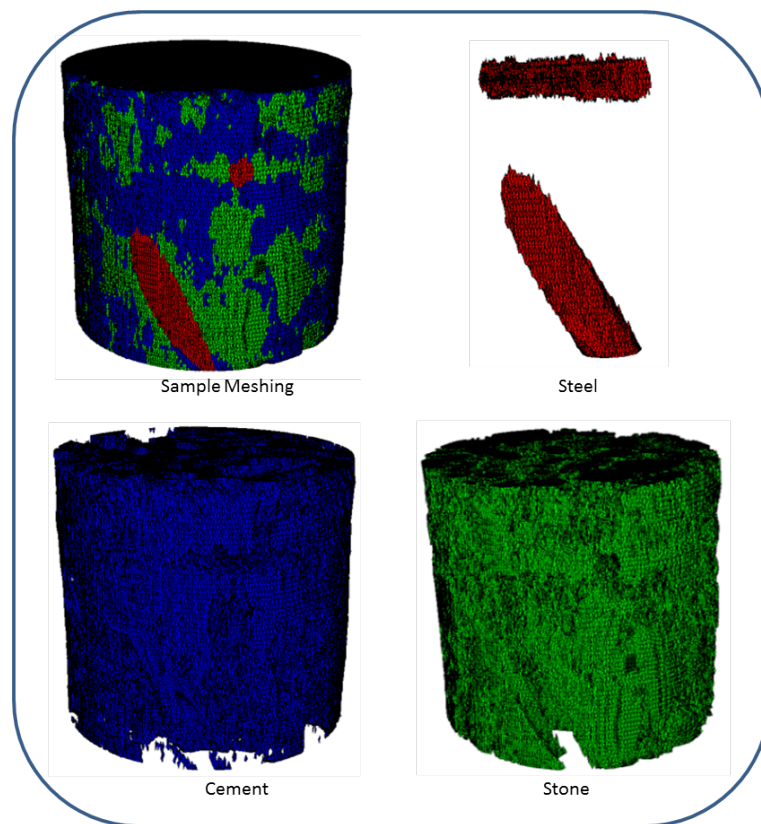


FIGURE 4.6: 3D model of Small concrete sample built from sectional slices reconstructed by compact CT device

## 4.2 Experiment with 950keV Linac Source

### 4.2.1 Experiment set-up

One of the most essential advantages that the CT inspection system proposed in this research precedes over the compacted CT device is that, our system can be easily disassembled and assembled for in situ inspection and there is no strict limitation to the scale of target object. Preliminary CT experiment is conducted in laboratory at first with the same sample in figure 4.2. The figure 4.7 illustrates the experimental layout. The X-ray beam source is 950keV Linac and a flat panel detector of Perkin Elmer is used to acquiring projection data, whose parameters are given in table 4.2 and table 4.3. The scanning is realized with a rotation stage to rotate sample every  $1^\circ$  over  $180^\circ$  range. The whole scanning process is remotely controlled.

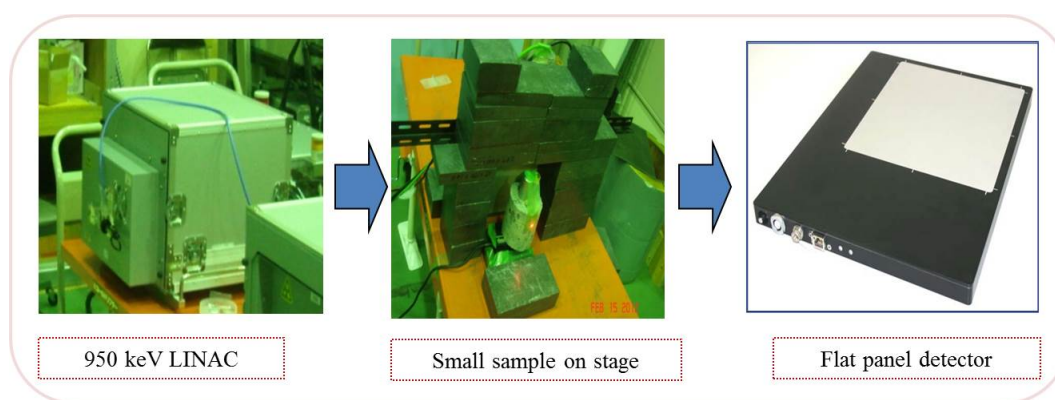


FIGURE 4.7: Illumination of experiment layout

TABLE 4.2: Specifications of 950keV Linac

Operating frequency	9.3GHz
RF source	Magnetron
RF power	250kW
Repetitive of pulse	$2\mu s$ 280pps
Beam current	64mA or more
Intensity of X-ray	50mGy/min or more at 1m
Voltage of electron gun	20kV

### 4.2.2 Image reconstruction

The transmission image from different angles are showed in figure 4.8, where part of inner details are reflected. Battery, aluminium and iron can be distinguished and

TABLE 4.3: Specifications of small flat panel detector (Perkin Elmer XRD0822)

Size	295 × 360 × 22mm
Scintillator	Gd2O2S:Tb
Pixel number	1024 × 1024
Pitch	200μm
Radiation energy	20kV-15MV

two steel rods inside the concrete is presented. Sectional images of 3 slices at the same position as figure 4.5 are reconstructed by FBP and displayed in figure 4.9. Identification is discernible for the inner structure especially the attachment accessories and steel rods. However, steel rod shows lighter color in center than outer mainly due to scattering X-ray inside concrete and beam hardening effect. More over, in figure 4.9c the steel rod contour is deteriorated by noise.

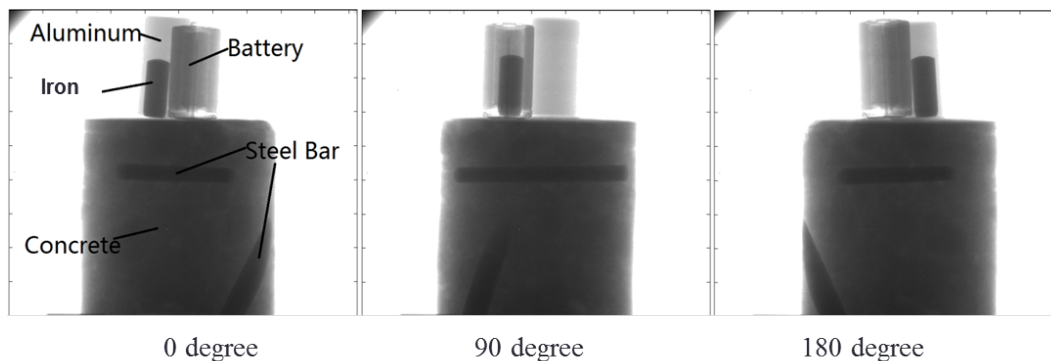


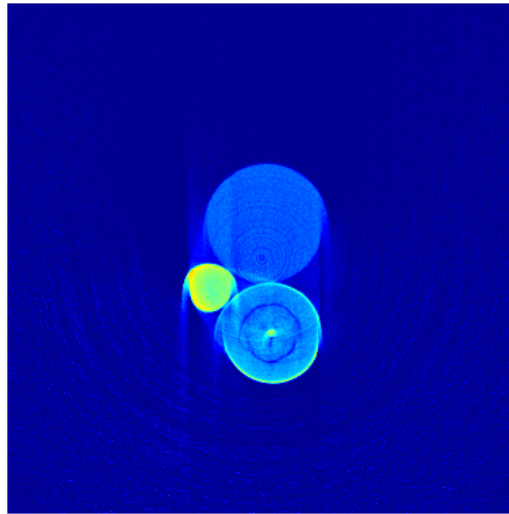
FIGURE 4.8: Transmission image

Sectional image of slice located at the flat steel rod is reconstructed with FBP, ART, SART as in figure 4.10 for comparison. ART result suffers more noise during iteration loops than that of SART and it converge much slower. Although some ring artifact is visible which is induced by back projection process, FBP deduces the result in just 1sec-3sec and gives similar image quality with SART.

### 4.2.3 3D modelling and mechanical analysis by VCAD

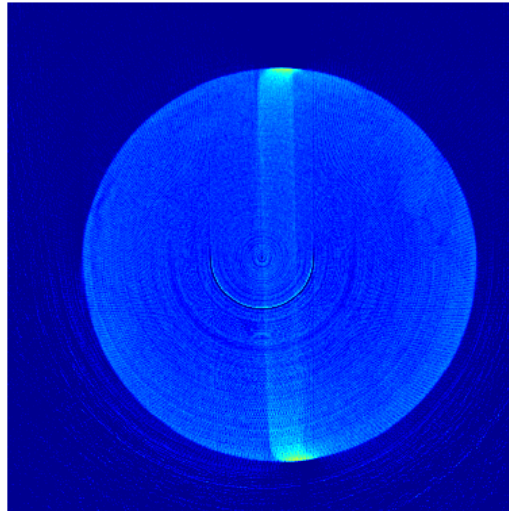
The small sample is divided into 80 slices along height direction and all the sectional images are reconstructed by FBP. By stacking all those slices, 3D model can be built using VCAD software, developed by Riken, Japan. [41] However, problem appeared when distinguishing materials by color contrast while modeling. As mentioned above, scattered X-ray noise and beam hardening effect influenced the image quality that the color

FBP,180



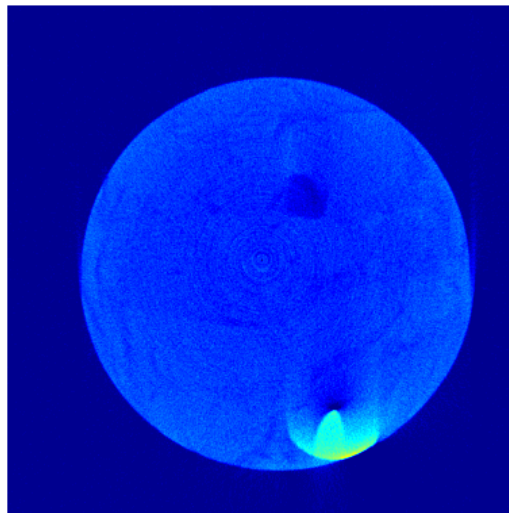
(A) Slice of attached battery, aluminum, iron

FBP,180



(B) Slice of flat steel rod

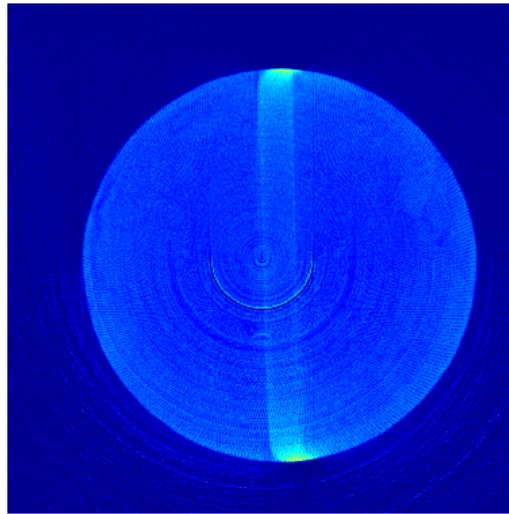
FBP,180



(c) Slice of inclined steel rod

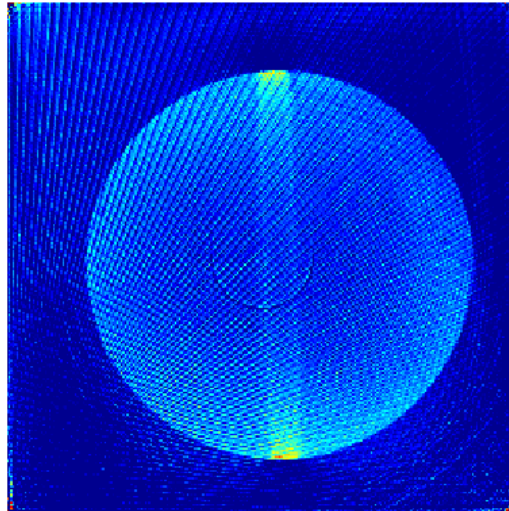
FIGURE 4.9: CT image of small concrete sample

FBP,180



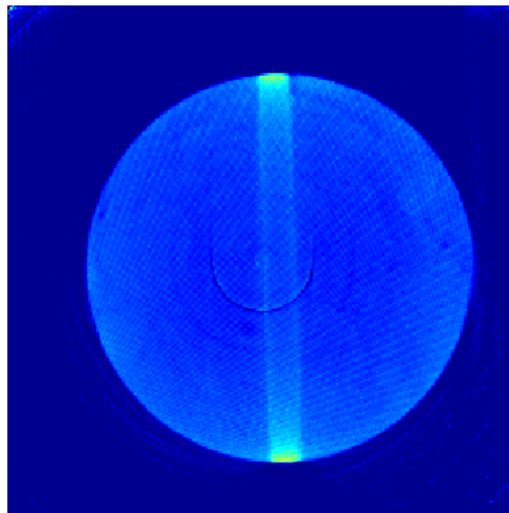
(A) FBP (180°)

ART,180



(B) ART (180°)

SART,180



(c) SART (180°)

FIGURE 4.10: CT image comparison by FBP, ART, SART (180°)

contrast between concrete and steel is relatively small. The software cannot precisely distinguish steel from concrete near their common boundary.

As a primary countermeasure, post manual processing is applied as figure 4.11 to condense the color of steel rod and enhance the contrast. After such treatment, 3D modeling and meshing is successfully built by VCAD software as showed in figure 4.12 and further mechanical analysis is available with the model and meshing.

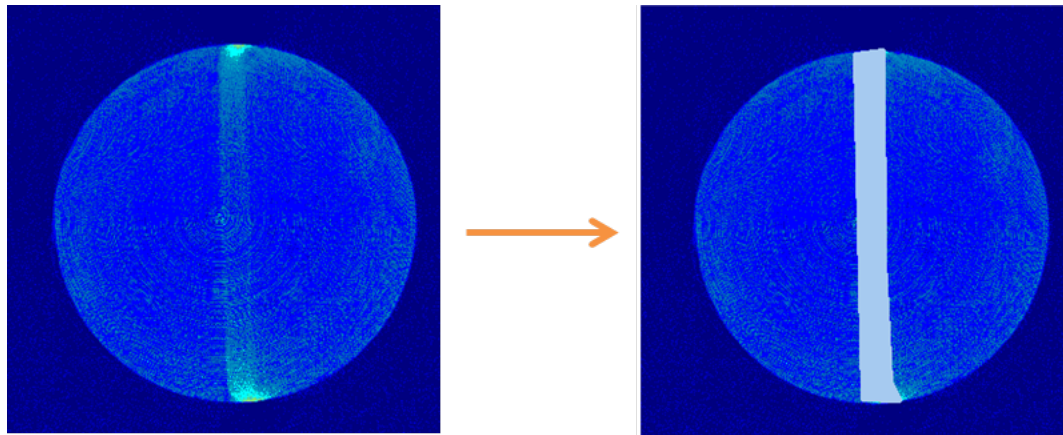


FIGURE 4.11: Post manual processing

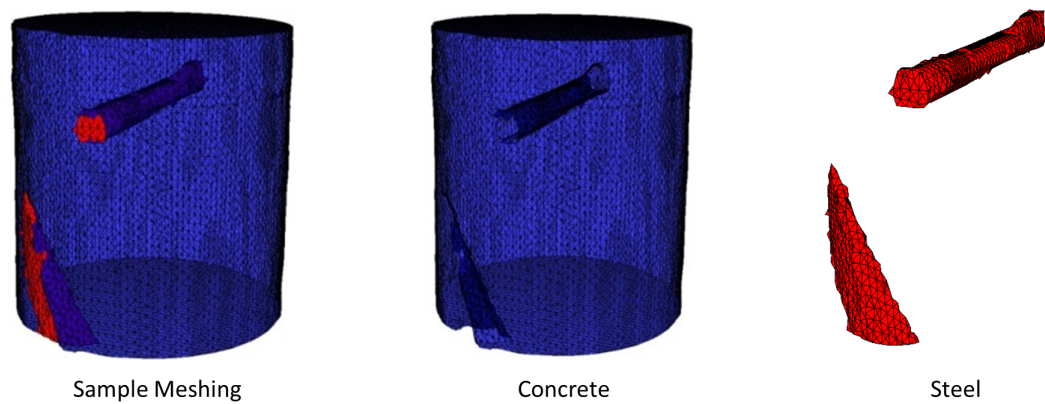


FIGURE 4.12: 3D model meshing of small sample

As an example, simple simulation is calculated by VCAD software with constraints in figure 4.13 that 50000N force is distributed uniformly on top surface of the sample. The bottom is fixed at vertical direction as constraint. Reference to material parameters are listed in table 4.4.

Calculation with the above mentioned mechanical model is done by VCAD software. The equivalent stress distribution of the sample are clearly signified in the results of figure 4.14, as well as displacement distribution in figure 4.15. The stress load and

displacement are shared by concrete and steel rod, and the sharing of each part can be clearly specified in the separate result presentation.

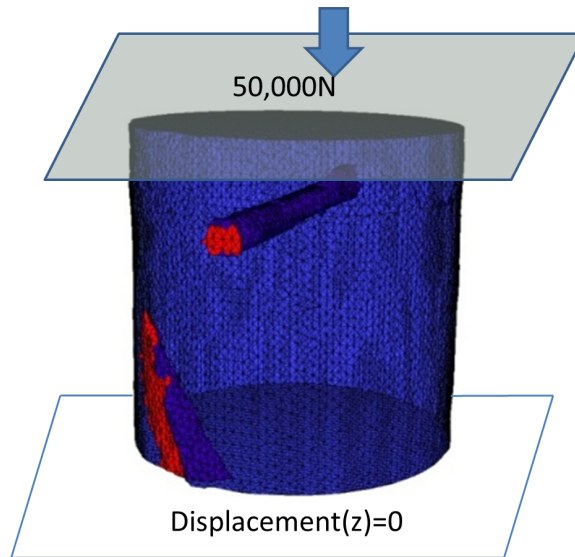


FIGURE 4.13: Mechanical model of structure analysis for small sample

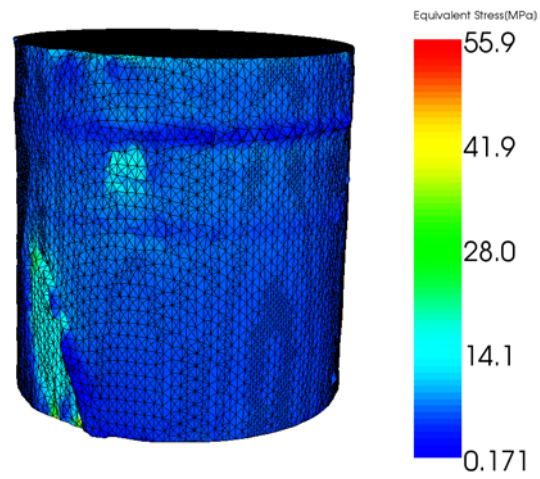
TABLE 4.4: Parameters of small sample

Material	Young's modulus(MPa)	Poisson's ratio
Concrete	28000	0.15
Steel	219620	0.30

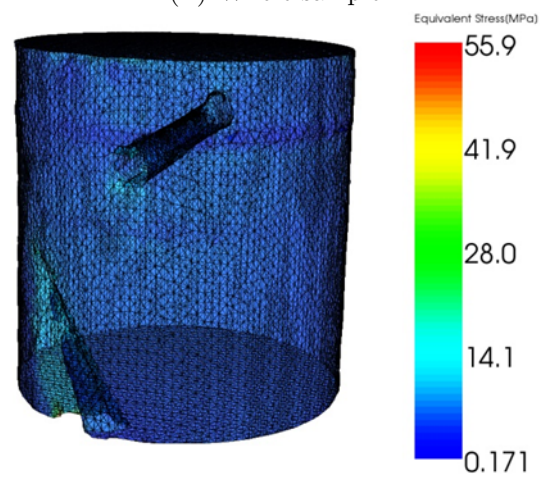
## 4.3 Experiment Improvement with Collimator

### 4.3.1 Experiment set-up

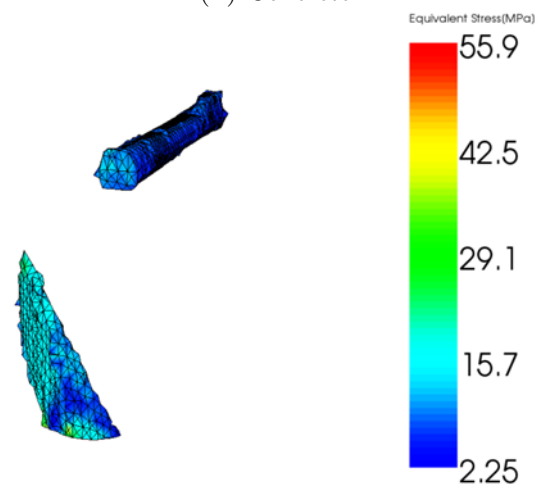
Scattered X-ray noise reduction and contrast enhancement become critical problems in this CT system development according to the above results. It caused serious influence to the image quality of reconstructed image and effects the identification for inner steel rod. Software improvement with wavelet-based image processing is under research in our group for contrast enhancement. On the other hand, improvement in hardware is also added to current system. IIC Todai Hybrid Scintillator is a line sensor with collimator and the configuration is illustrated in figure 4.16. [42] The lateral and vertical collimators could confine that only beam with a certain angle can enter the scintillator. It's possible to use a compacted two-fold scintillator to acquiring two kinds of data at the same time. While in this experiment only one scintillator is enough, the one in the



(A) Whole sample

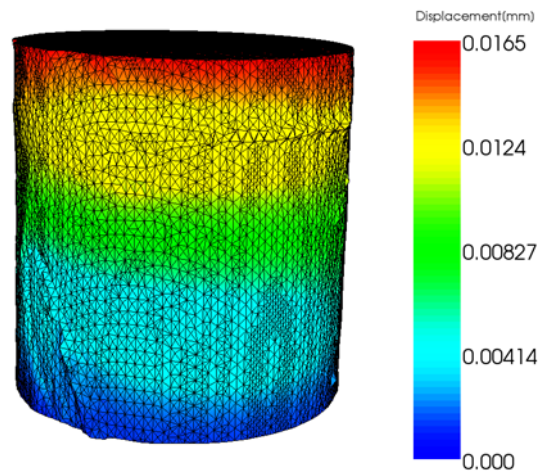


(B) Concrete

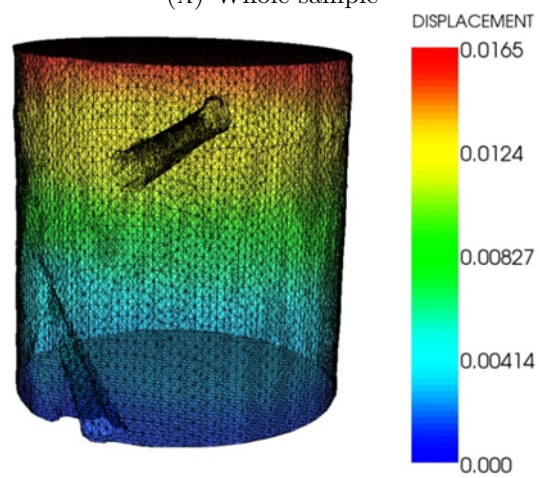


(C) Steel rods

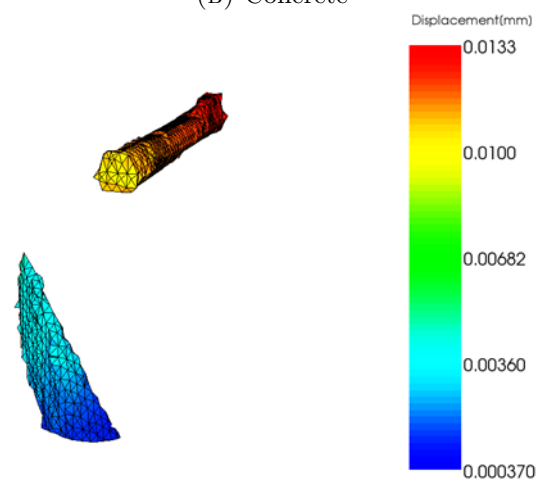
FIGURE 4.14: Structure analysis results for small sample: equivalent stress(MPa)



(A) Whole sample



(B) Concrete



(C) Steel rods

FIGURE 4.15: Structure analysis results for small sample: displacement(mm)

back made of 15mm CdWO<sub>4</sub>. As showed in figure 4.18 and figure 4.19, the CT system is set up again adopting this line sensor. Another reference detector attached to relative collimators is matched with the line sensor which can measure background signals and calculate calibration data. Since the line sensor collect data in 1 dimension, stage with both rotation and translation function is set up to realize 2 dimensions scanning. The same sample in figure 4.2 is used while all the attachment on the top is removed. Considering shortening scanning time, projection view is set as every 2° covering 180° range, still condense enough to be considered as full projection problem. Additionally, in order to synchronize frequency between data acquiring and bean emission, trigger synchronization system in figure 4.20 is added to generate synchronous trigger signals to excite the line sensor and the Linac at the same time.

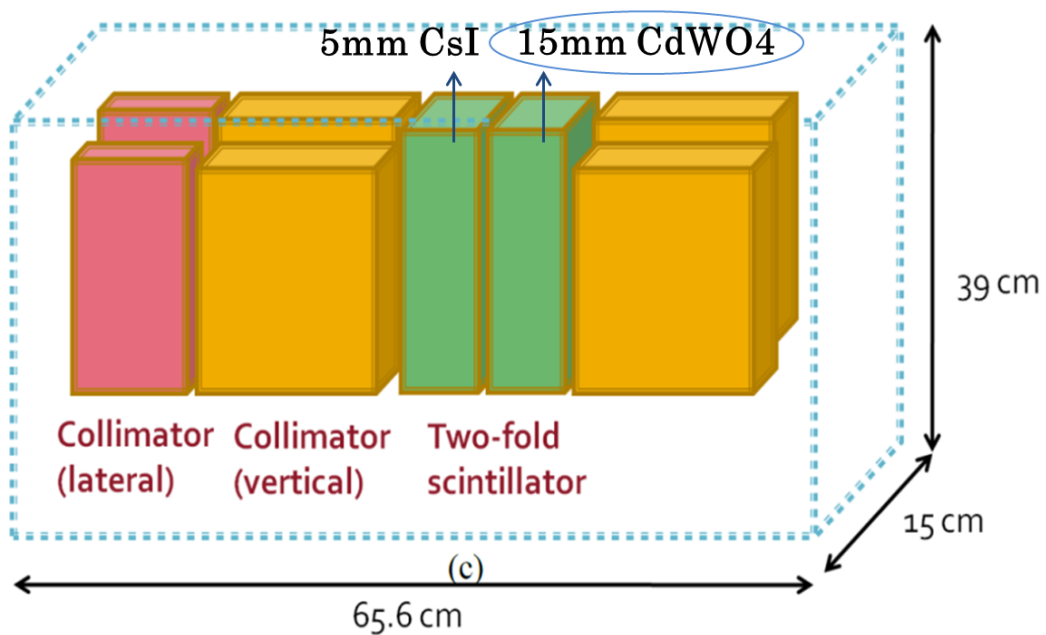
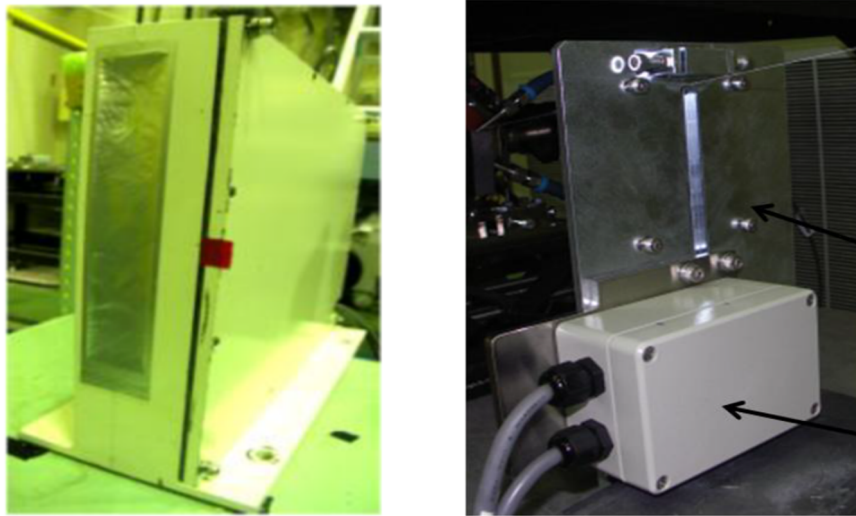


FIGURE 4.16: Configuration of IIC Todai Hybrid Scintillator

### 4.3.2 Result and discussion

The transmission images from different angles are showed in figure 4.21. Reconstruction image of slices located at steel rods are showed in figure 4.22. Compared with former results in figure 4.9, the steel rods are showing very distinctive contours and the color contrast between concrete and steel is quite clear. The better image quality proved that the scattered X-ray noise is suppressed substantially. There's no need for any further passed manual processing and the VCAD software can easily distinguish the color contrast between concrete and steel rod to built a precise 3D model as in figure 4.23, which provides more credible mechanical model for further structural analysis.



(A) IIC Todai Hybrid Scintillator (B) Reference detector with collimator

FIGURE 4.17: IIC Todai Hybrid Scintillator with reference detector

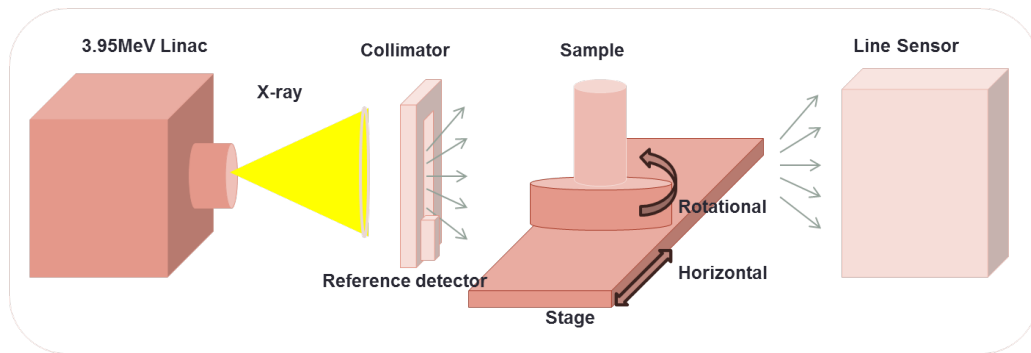


FIGURE 4.18: Experiment Schema of improved CT system

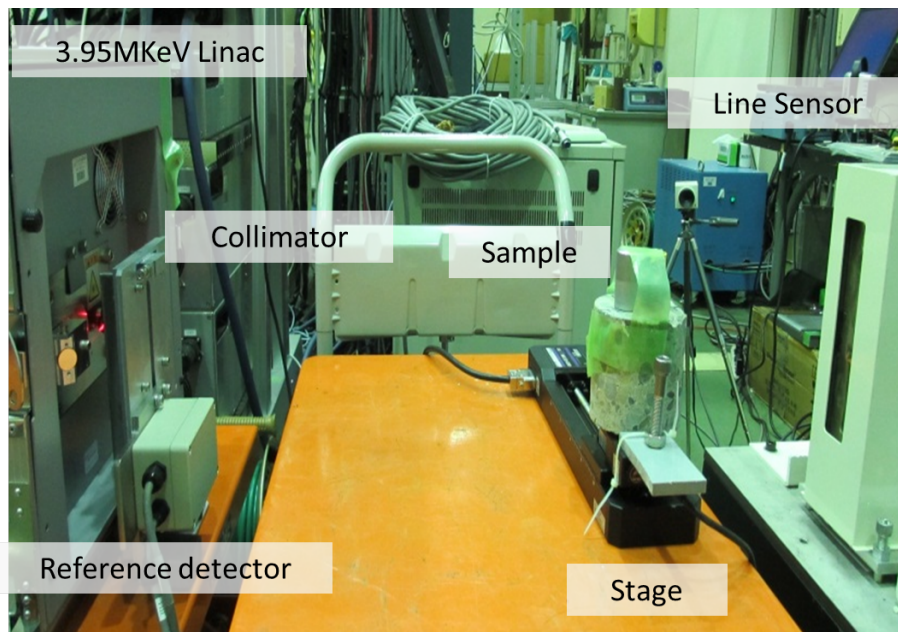
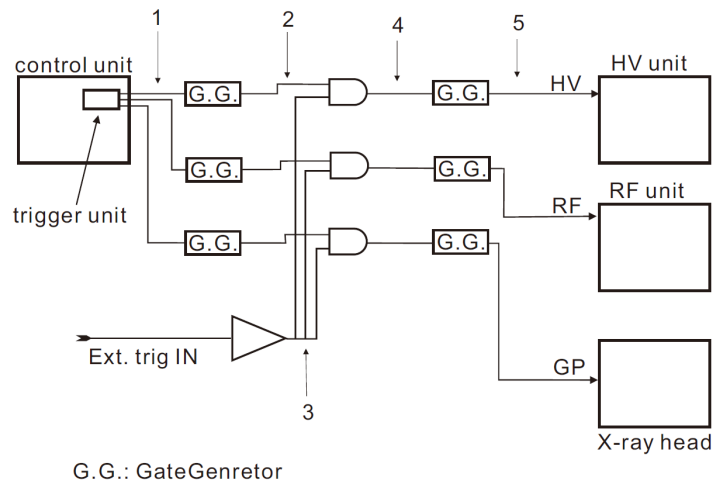
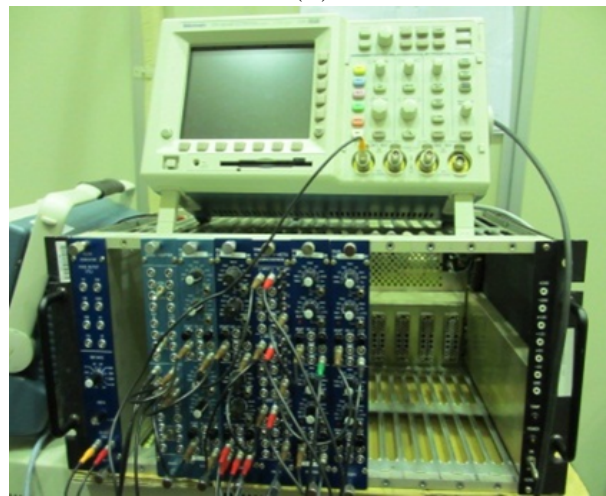


FIGURE 4.19: Experiment set up of improved CT system



(A)



(B)

FIGURE 4.20: Trigger synchronization system

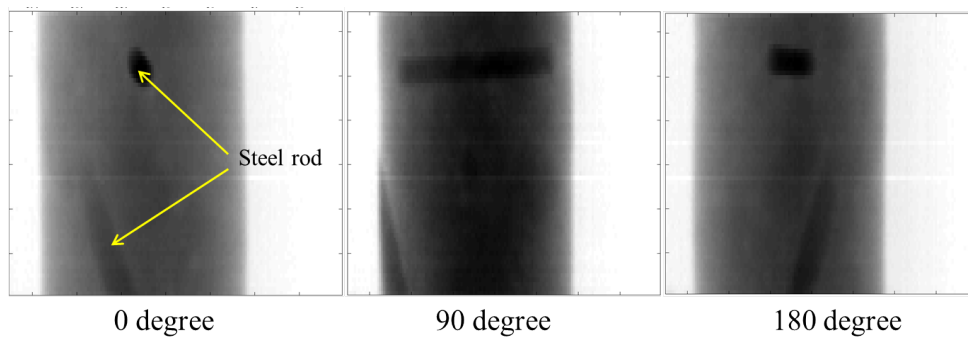
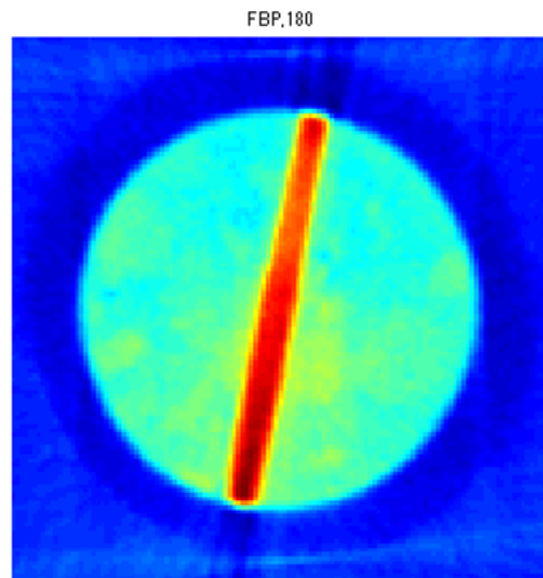
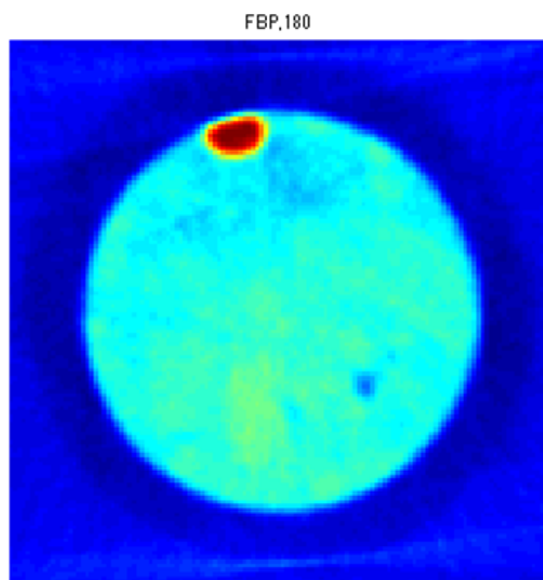


FIGURE 4.21: Transmission image



(A) Slice of flat steel rod



(B) Slice of inclined steel rod

FIGURE 4.22: CT image of small concrete sample of improved CT system

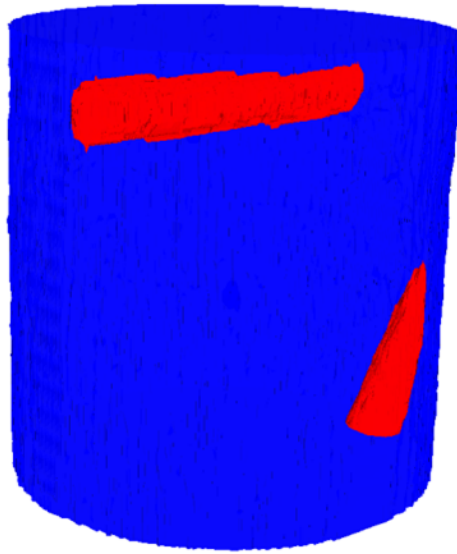
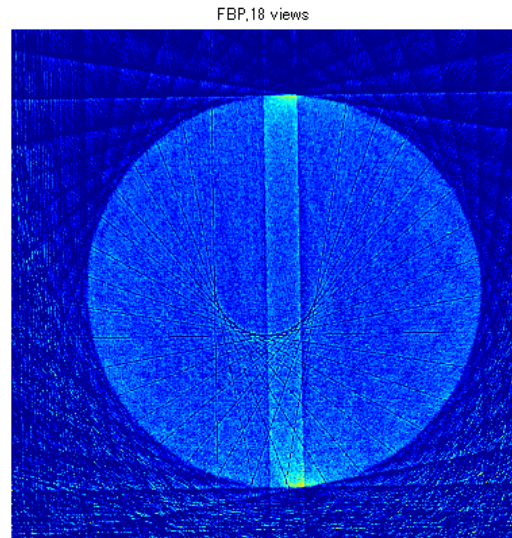


FIGURE 4.23: 3D model for small sample of improved CT system

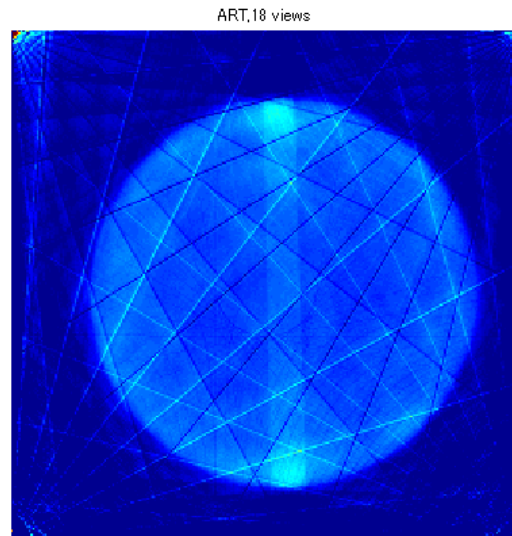
#### 4.4 Image Reconstruction under Incomplete Projection

In order to verify the effect of partial CT, reconstructions with incomplete projection are simulated with experimental data. General situations of few views and limited angle range problems are calculated with experimental data acquired by FPD at first. According to the results in figure 4.24 and figure 4.25, line artifact and shadow blurring caused by missing data is apparent in FBP, ART and SART reconstruction results. Then SART-TV is applied with the same experimental data. In figure 4.26, since the line artifact and steel rods are in the similar color due to low contrast, smoothing of TV minimization didn't make steel rods clearer. In figure 4.27, although more loops showed better recovery to the contour of sample, while the inner steel rods is also blurred to some extent during iteration. Thence how to choose proper parameters of SART-TV algorithm is very difficult when using experimental data.

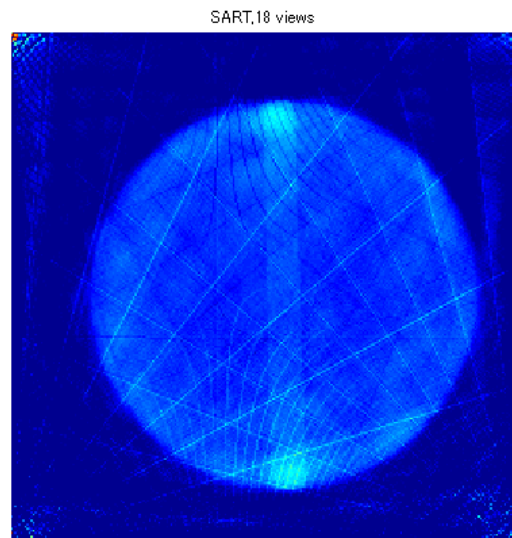
Similarly, reconstructions are calculated with experimental data acquired with line sensor. Figure 4.28 is sectional images using full projections. Comparatively figure 4.29 and figure 4.30 are reconstructed with incomplete projection data. It's showing much more artifacts and shadow especially in FBP reconstruction. SART-TV can effectively eliminate line artifact as showed in figure 4.29c and the contour of sample is also recovered in figure 4.30c. The discontinuous points in steel rods are caused by the effect of interruption during Linac operation. Another reason is that the bad pixels in detector is magnified during iteration, which is expected to be improved by optimize the initialization.



(A) FBP

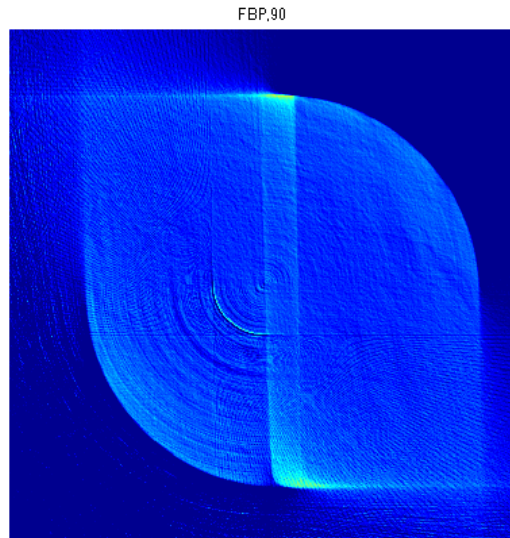


(B) ART

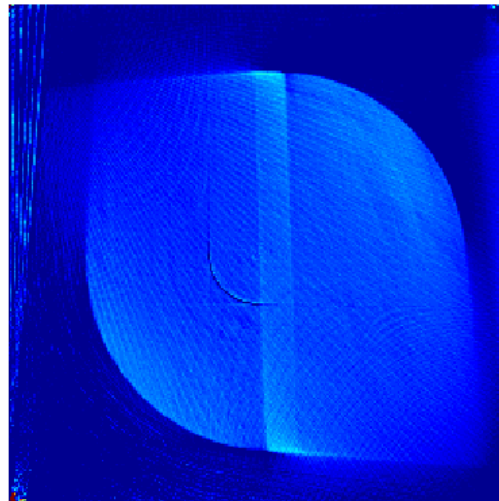


(C) SART

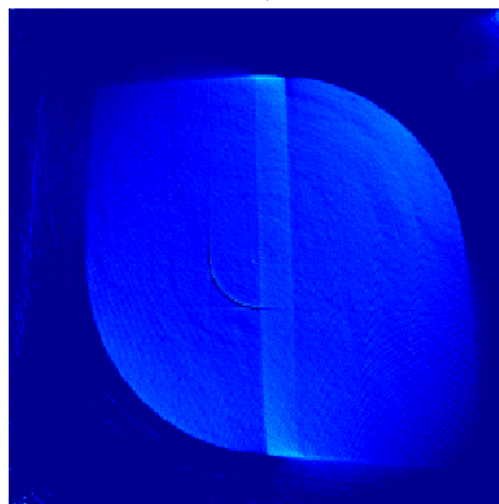
FIGURE 4.24: CT image of few view problem ( $10^\circ$  increment) using experimental data with FPD



(A) FBP  
ART,90



(B) ART  
SART,90



(C) SART

FIGURE 4.25: CT image of limited angle range ( $90^\circ$ ) using experimental data with FPD

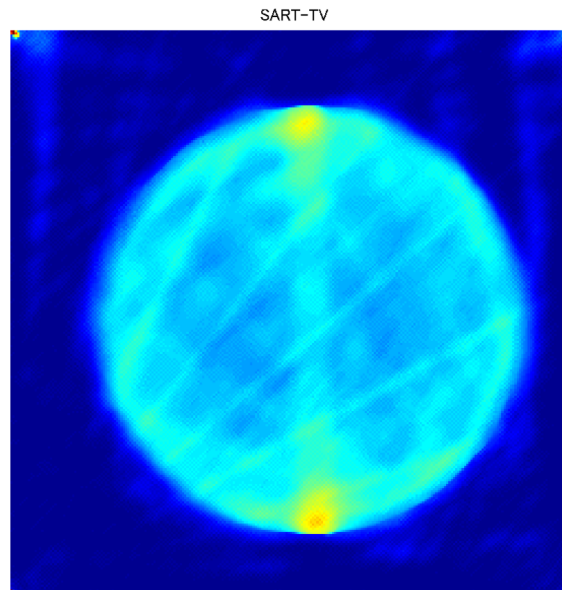
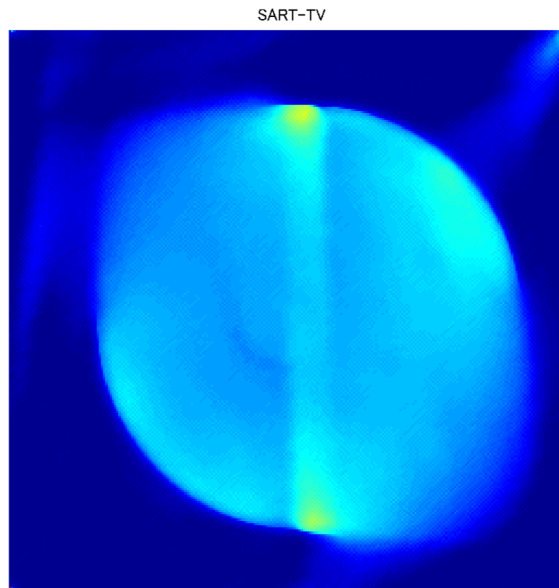
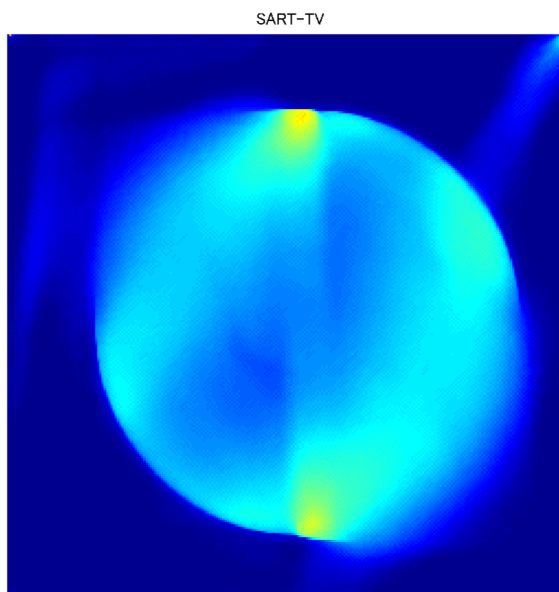


FIGURE 4.26: CT image of few view problem ( $10^\circ$  increment) using experimental data with FPD by SART-TV

In general, the sparsity of projection data would bring about artifacts and effect the evaluation of inner steel rod in sectional image. The sparser the data is, more serious the influence is. Algorithms with recovery ability such as SART-TV works perfectly in simulation but in practical application with experimental data, the noisy raw data makes the threshold and iteration parameter to be very difficult to be optimized. Suitability should be improved in future research.



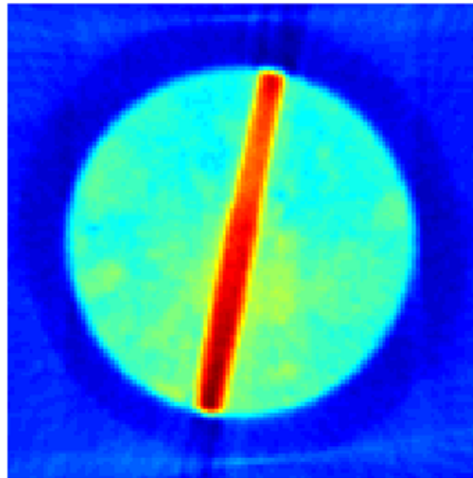
(A) Loop=10



(B) Loop=100

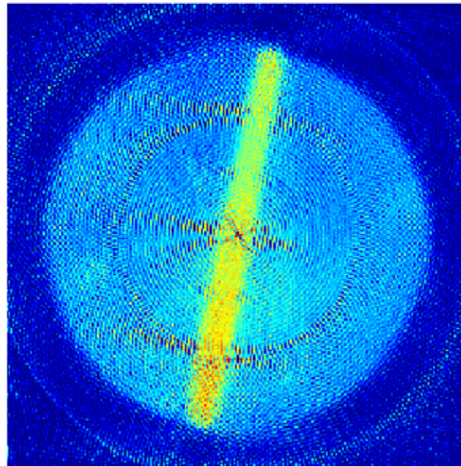
FIGURE 4.27: CT image of limited angle range ( $90^\circ$ ) using experimental data with FPD by SART-TV

FBP, 180



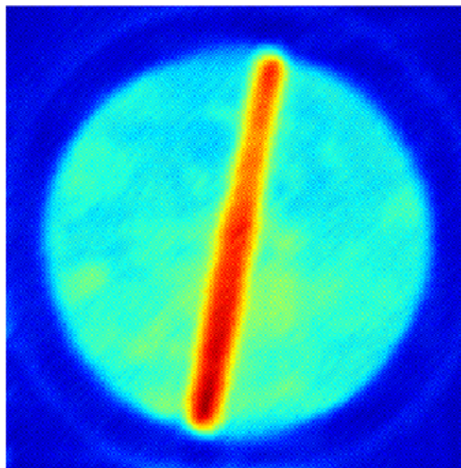
(A) FBP

SART, 180



(B) SART

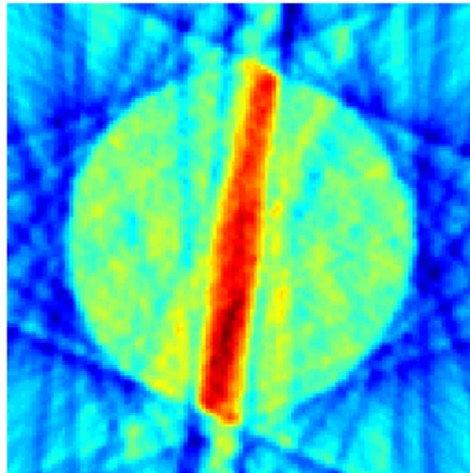
SART-TV, 180



(C) SART-TV

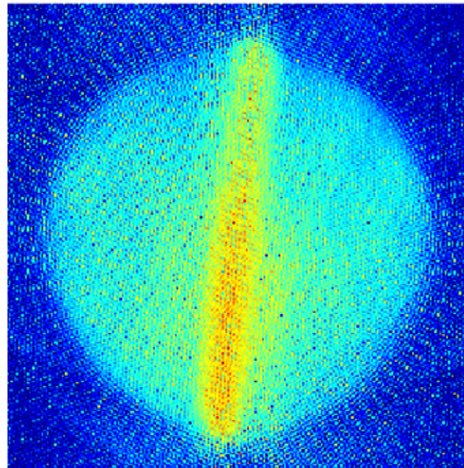
FIGURE 4.28: CT image using experimental data with line sensor ( $180^\circ$ )

FBP, 180, per 16 degree



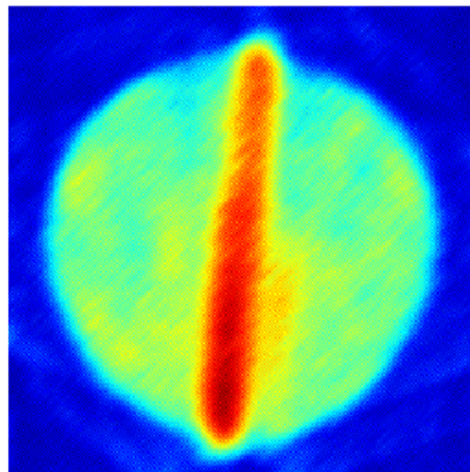
(A) FBP

SART, 180 pre 16 degree



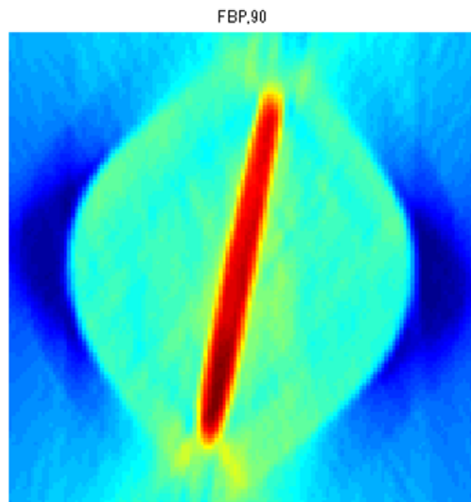
(B) SART

SART-TV, 180 pre 16 degree

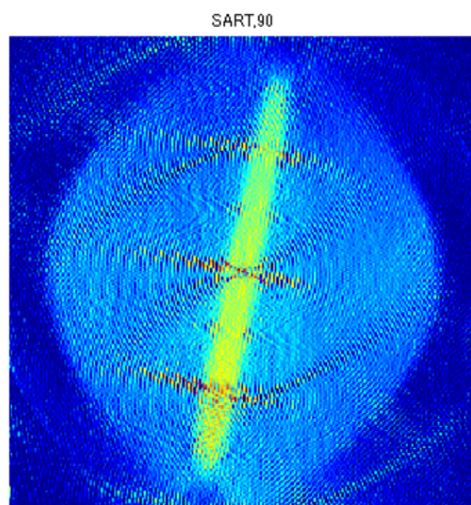


(C) SART-TV

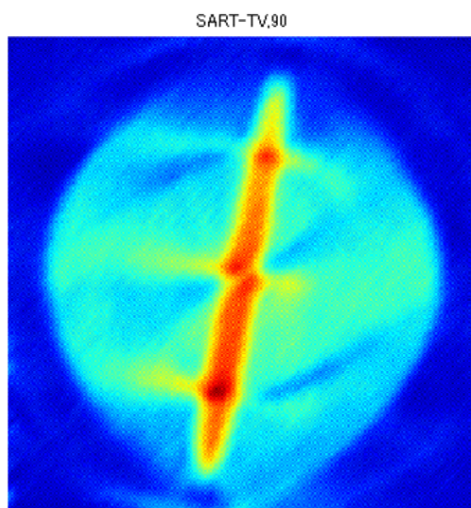
FIGURE 4.29: CT image of few view problem ( $16^\circ$  increment) using experimental data with line sensor



(A) FBP



(B) SART



(c) SART-TV

FIGURE 4.30: CT image of limited angle range ( $90^\circ$ ) using experimental data with line sensor

## Chapter 5

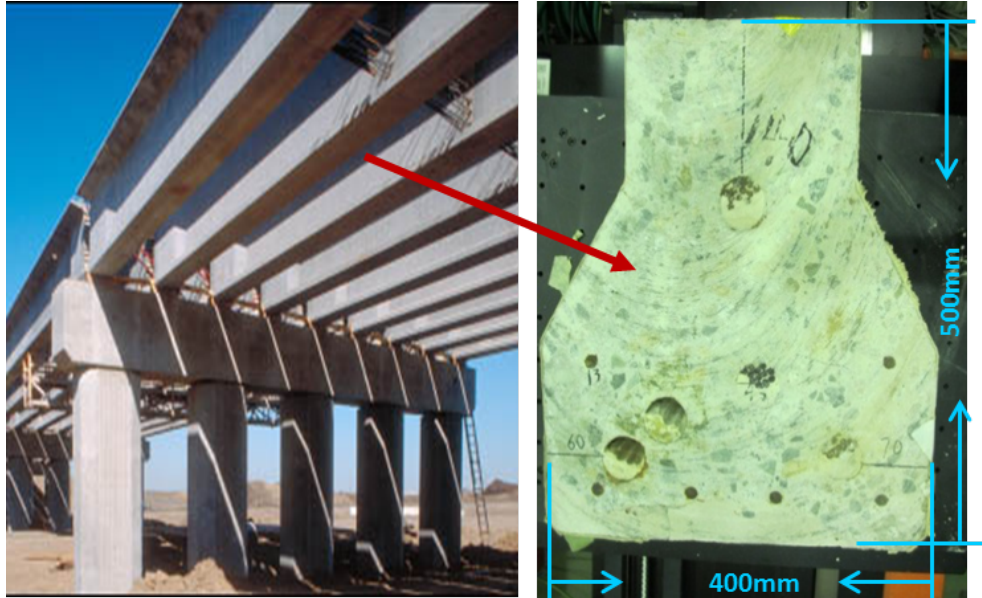
# Computed Tomography Experiment for Truncated Projection Problem

Based on former experience on experiments and simulations, in this chapter, CT for concrete specimen and scaled down specimen of PC bridge girder is conducted in the laboratory. Reconstruction work is mainly focused on ROI tomography for inner steel wire cluster.

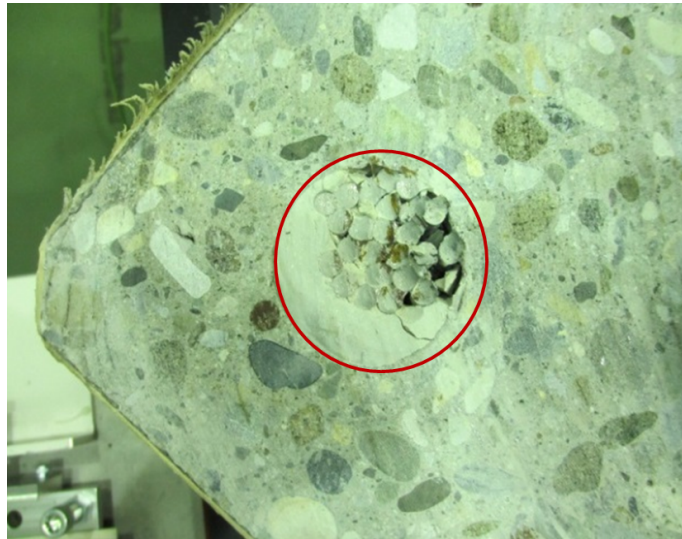
### 5.1 Experiment with Concrete Specimen of PC Bridge Girder

#### 5.1.1 Experiment set-up

The concrete specimen is a 10mm thick slice cut from bridge girder in the size of  $400 \times 500mm$ . Several RC steel rebars are embedded in the concrete as well as PC steel wire cluster as indicated in figure 5.1b. Considering that enough penetration ability is necessary to pass through concrete of such thickness, the 3.95MeV Linac is adopted as the X-ray beam source. The detector is similar to previous Flat Panel Detector but with lager size, parameters listed in table 5.2. The scatted X-ray noise is very serious so that some lead blocks is arranged around the specimen and detector. The shielding lead blocks can absorb the scattered X-ray of low energy in order to improve the scanning data quality as indicated in figure 5.2 and figure 5.3. Similarly, transmission data is also collected by line sensor for comparison.



(A) Concrete specimen cut from PC bridge girder



(B) PC steel wire cluster

FIGURE 5.1: Concrete specimen of PC bridge girder

TABLE 5.1: Specifications of 3.95MeV Linac

Operating frequency	9.3GHz
RF source	Magnetron
RF power	1.5MW
Repetitive of pulse	$4\mu s$ 200pps
Beam current	100mA
Output current of electron gun	300mA
Voltage of electron gun	20kV

TABLE 5.2: Specifications of large flat panel detector (Perkin Elmer XRD1622)

Size	500 × 560 × 22mm
Scintillator	Gd <sub>2</sub> O <sub>2</sub> S:Tb
Pixel number	2048 × 2048
Pitch	200 $\mu$ m
Radiation energy	20kV-15MV

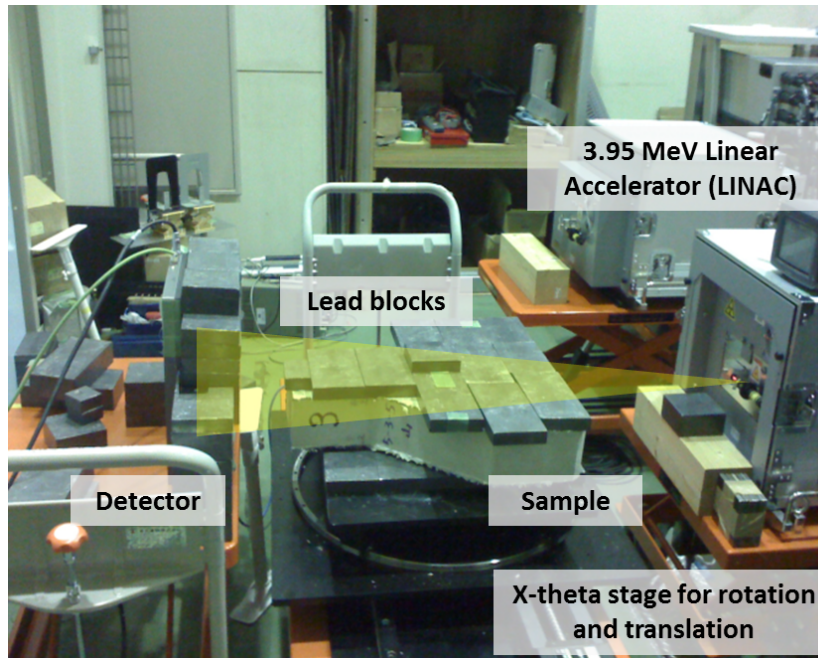
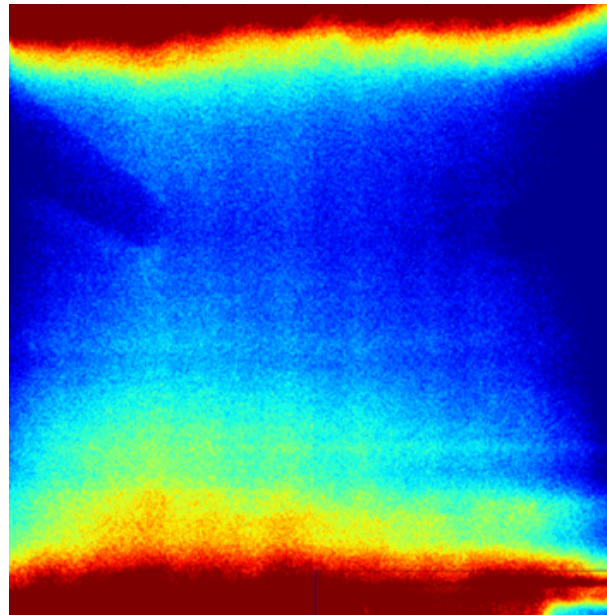


FIGURE 5.2: Experiment set up for big concrete specimen

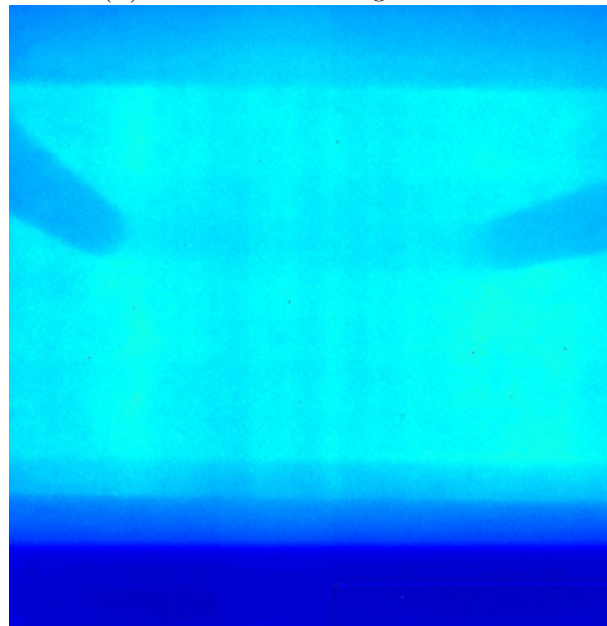
### 5.1.2 Results and discussion

Transmission images at two positions of big concrete specimen by FPD and line sensor are compared. In figure 5.4 at the position A, the photography was focused on vertical steel wire clusters. More than 20 wires are bundled in one cluster but only several of them can be confirmed at transmission image at a certain direction. Steel wires are discernable in both situations while in line sensor image, the image has larger color contrast and the steel rods are much clearer. The figure 5.5 gives the image taken at position B, where two steel rods can be seen located in the right. The wire clusters next to the two rods can only be identifies clearly in image taken by line sensor, and in FPD image, the wire cluster can hardly be affirmed.

According to EGS5 program [43] simulation results in figure 5.6, line sensor possesses higher sensitivity than FPD, especially to X-ray with higher energy level over 1MeV. Taking into account that the X-ray emitted by 3.95 MeV Linac should hold the spectrum mainly around several MeV magnitude, there's no doubt that line sensor is more capable



(A) Without collimating lead blocks



(B) With collimating lead blocks

FIGURE 5.3: Transmission image of RC Steel rod (reduce scattered X-ray noise by lead blocks to rise S/N ratio)

to capture the signals than FPD. In addition to high detector efficiency, the collimators of line sensor also contributes to better S/N ratio. However, the 2D scanning mode of line sensor is confined by stage accuracy of 1mm pitch that overall image resolution is worse than FPD and scanning is very time-consuming. By the way, strips appears due to synchronization and higher energy harmonics in the incident beam, which is expected to be solved through synchronization system.

The projection for CT didn't succeed with the big concrete specimen for the problem

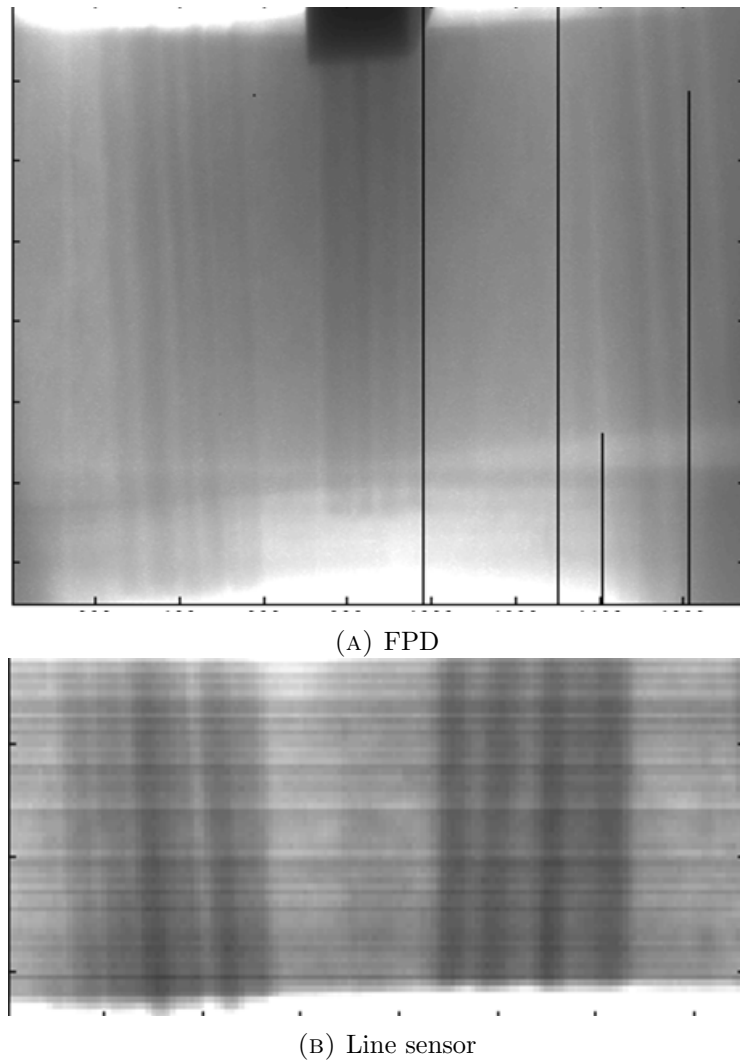
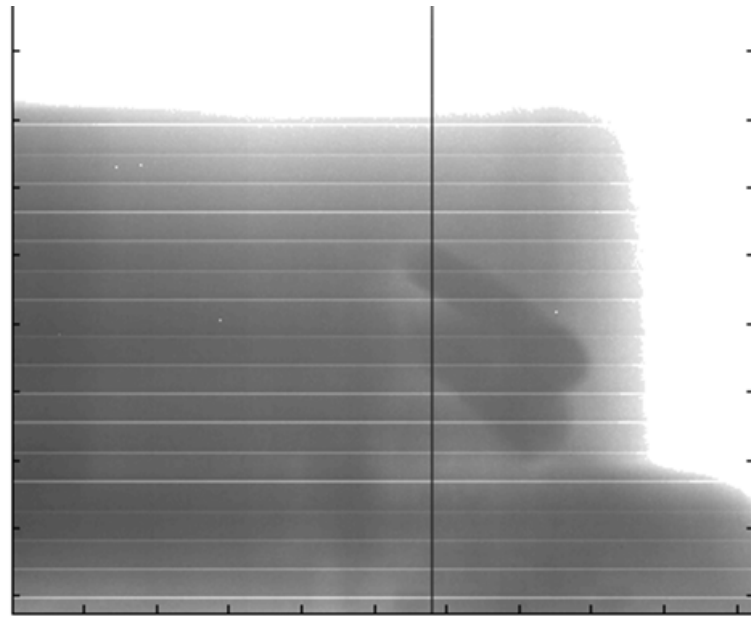
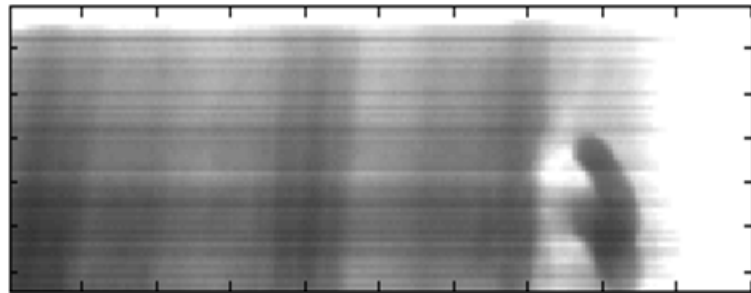


FIGURE 5.4: Transmission image at position A

that overexposure happens easily due to the complex contour shape of the specimen. Usually, the ideal situation for CT is that the X-ray passes through path of same length at each projection angle, which implies that the sample is shaped in a round circle and the center is in the rotation axis. Some little difference from ideal situation won't be a problem to apply CT. However, the big concrete specimen is in rather large size and the shape is too complex. It means that the length of beam path does not only vary at each projection angle distinctively, but also varies with quite big difference inside each view. This brings about great troubles to adjust the beam intensity to make sure that neither low penetration nor overexposure happens in all projection data. Two methods are proposed in future work. The first one is design a filter to adjust intensity according to the variation of beam path. Another one is adjust the exposure time of detector according to the concrete thickness the beam passed to ensure acquiring effective and valid projection data.



(A) FPD



(B) Line sensor

FIGURE 5.5: Transmission image at position B

## 5.2 ROI CT Experiment with Scaled Down Specimen

### 5.2.1 Experiment set-up

In order to verify the problems in CT for ROI reconstruction of large concrete sample under truncated projection, a preliminary test experiment is carried out using scaled down specimen made of polyethylene. The small specimen resembles the shape of the original concrete specimen but its size is only 1/10 of it. Similarly as the original concrete specimen, both rods and wire clusters are embedded inside the base material. The rods are made of aluminum with 3mm diameter. The wires are also made of aluminum and the diameter is 0.8mm. Each cluster consists of 6 wires. 2 rods and 3 wire clusters are in the vertical direction and 1 rod is inserted in horizontal direction as showed in figure 5.7.

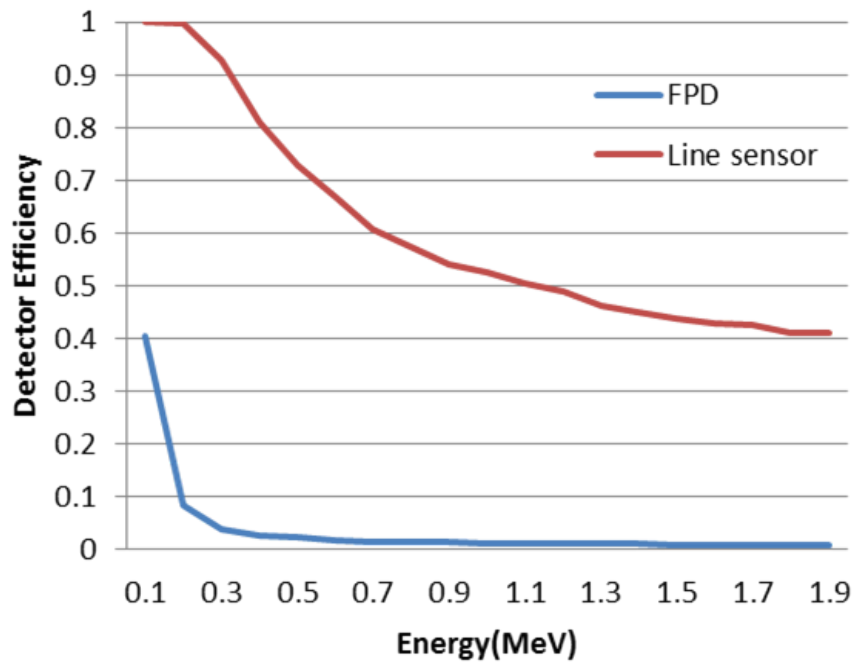
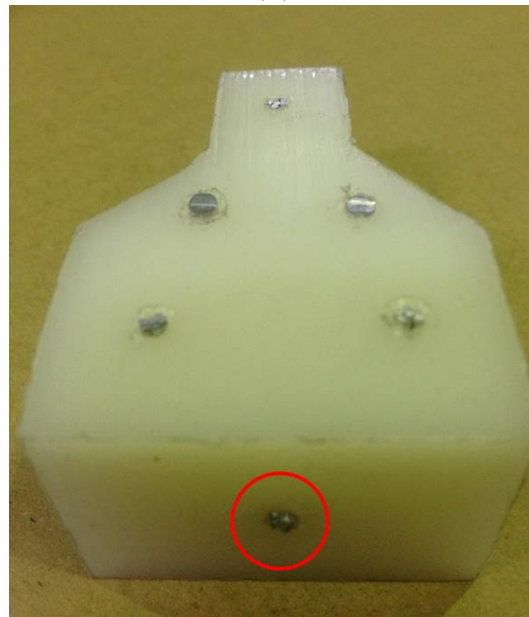


FIGURE 5.6: Detector efficiency of FPD and line sensor

The X-ray beam is provided by a X-ray tube system of Amptek Mini-X, specification of which is listed in table 5.3. The Scanning condition is set at 40kV and  $50\mu A$ . The transmission images are recorded by a front-illuminated FFT-CCD area image sensor of Hamamatsu S10811-11 and the exposure time is set as 6s for one shot. Each projection view was taken at  $1^\circ$  covering  $180^\circ$  range. The sensor size is relatively small compared with the specimen so that only part of the whole specimen other than the entire specimen can be photographed in the sensor. As a result, the scanning becomes a truncated projection problem, similar as the ROI tomography simulation geography in figure 3.11 of chapter 3. The specimen is fixed in a rotation stage and one of the wire cluster is placed near the rotary axis. Such geometry assures that in each projection view over the  $180^\circ$  angle range, this wire cluster is always reflected in the image sensor screen, although other part of the specimen would be outside the sensor screen and their information are missing at some of the projection angles. Besides, this geometry resembles figure 3.13 of chapter 3, which satisfies the conditions in DBPH reconstruction: each point of the wires is inside ROI and belongs to one Hilbert lines, and for each Hilbert line, one of its end point is outside the object support. The setup in figure 5.8 illustrated the experiment system.



(A)



(B)

FIGURE 5.7: Scaled down specimen

### 5.2.2 Results and discussion

The transmission image at  $0^\circ$ ,  $90^\circ$  and  $180^\circ$  are showed in figure 5.9. The denser the material is, the deeper is the color. The horizontal inserted rod indicated in figure 5.7b appears as the dark and wide horizontal line in the  $0^\circ$  and  $180^\circ$  transmission image. In the  $90^\circ$  transmission image it was presented as the big round shape when rotation stage reached the direction that the X-ray beam are parallel with this rod. The wire clusters and other 2 rods in vertical direction appears as vertical lines. There is only one wire

TABLE 5.3: Specifications of Amptek Mini-X X-ray tube

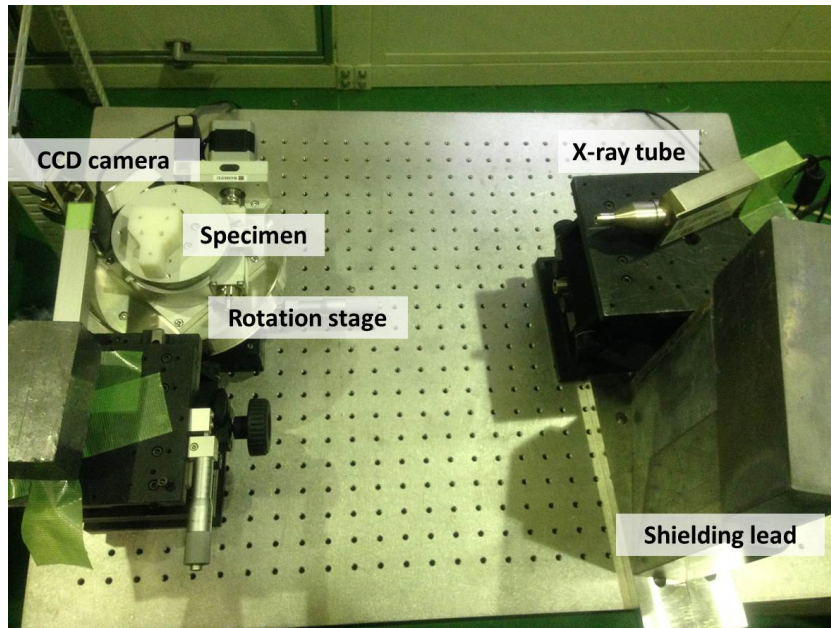
Target material	Silver (Ag)
Target thickness	$0.75\mu m(\pm 0.1\mu m)$
Tube voltage	10kV to 50kV
Tube current	$5\mu A$ Min./ $200\mu A$ Max.
Power consumption	9W at 50kV and $80\mu A$
Control	USB
Weight	360g

TABLE 5.4: Specifications of Hamamatsu CCD area image sensor (S10811-11)

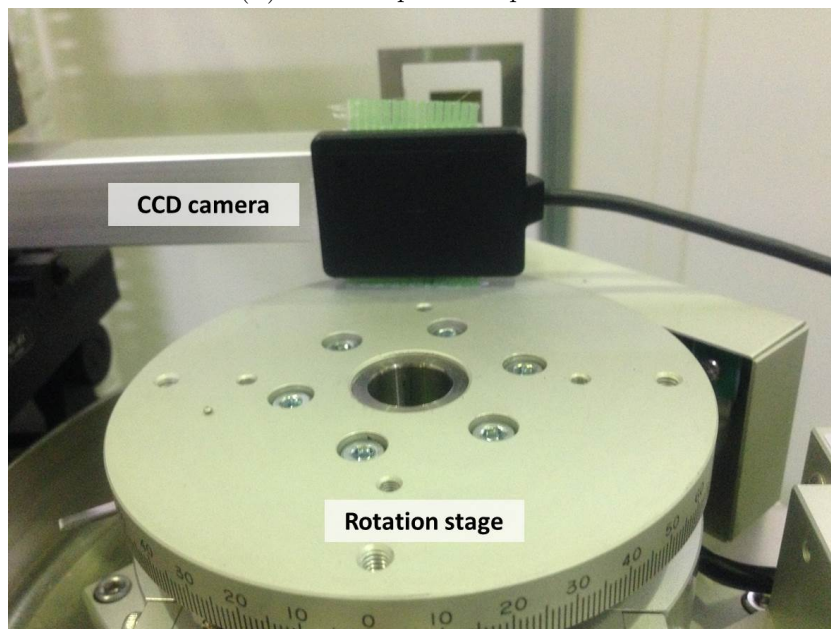
Size	$34 \times 24\text{mm}$
Scintillator	CsI(+FOP)
Pixel number	$1700 \times 1200$
Pitch	$20\mu m$
Max dose irradiation	50Gy

cluster in the center that is always appeared in transmission images at any projection angle. The reconstruction slice was chosen at the height where only vertical rods and wires are contained.

The reconstruction is implemented with FBP and DBPH algorithms with full projection angle range of  $180^\circ$ . The results are displayed in figure 5.10 under same gray scaling ruler of  $[0,0.003]$ . The wires located in the upper right position in the image because they are not exactly coincided with the rotation center. The image reconstructed by FBP suffers more serious ring artifact and the detail information of wires are submerged and missed in bright color, although the rough outline of wires can be recognized. This accords with previous analysis in chapter 3 that the truncated projection have influence spreading over the whole image. On the contrary, the image reconstructed by DBPH didn't brought bad influence caused by truncation to the ROI, which part always possesses full projection information. Each of the 6 wires in the cluster are showing clear boundaries and the resolution could be further improved by optimize the experiment geometry to enhance the image magnification effect or use detector with higher pixel number.

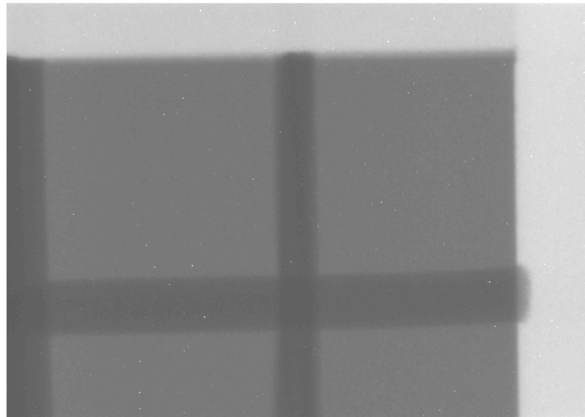


(A) Whole experiment platform

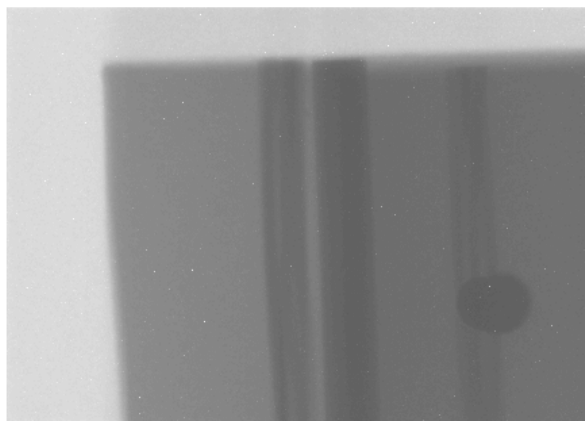


(B) CCD camera and rotation stage

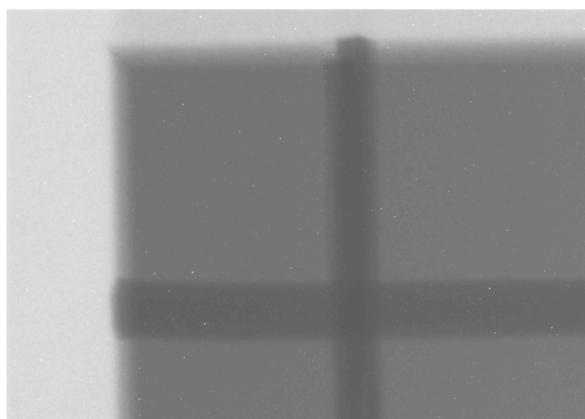
FIGURE 5.8: Experiment setup for ROI CT of scaled down specimen



(A)  $0^\circ$

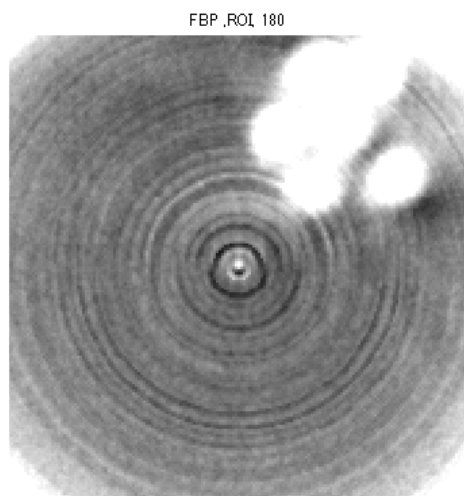


(B)  $90^\circ$

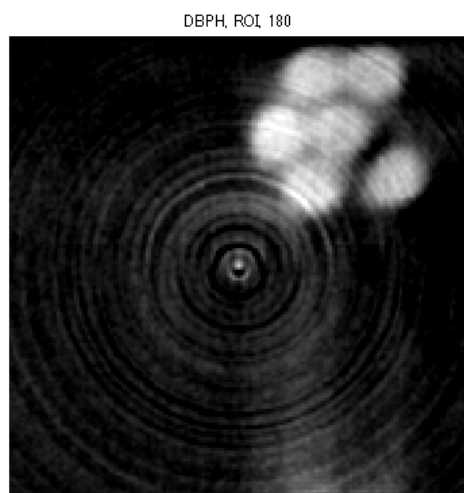


(C)  $180^\circ$

FIGURE 5.9: Transmission image of scaled down specimen



(A) FBP



(B) DBPH

FIGURE 5.10: ROI reconstruction for section of scaled down specimen

## Chapter 6

# Dual-energy Computed Tomography Analysis for Corrosion Evaluation

Dual-energy CT can be used to estimate the component of media material by identify the atomic number and density from CT images. It's expected to be applied in corrosion estimation of steel components in aging bridge such as rusted inner steel rods and corrosion layer of components in steel bridge. Relative research is discussed in this chapter, including both simulation and experiment works.

### 6.1 Simulation about Dual-energy CT Analysis

#### 6.1.1 Methodology of dual-energy CT

Dual-energy CT analysis for material identification is based on the attenuation character of the specific material under certain given energy level. Reconstructed with projection data, CT image is actually representation of linear attenuation coefficient  $\mu$  which denotes how strongly the media material absorbs or scatters beam light. This character can also be described by the mass attenuation coefficient

$$\mu_m = \mu/\rho$$

which is defined as attenuation coefficient per unit mass.

According to Beer-Lambert law,

$$I = I_0 e^{-(\mu/\rho)\rho l} \quad (6.1)$$

the original beam intensity of  $I_0$  become  $I$  after penetrating through the media object, where  $\rho$  is density,  $l$  is the length of beam path,  $\rho l$  is the area density known also as mass thickness.

When beam penetrate through media material, the attenuation mechanisms mainly consists the following process:[44]

- Rayleigh scattering (coherent scattering)
- Compton scattering (incoherent scattering)
- Photoelectric absorption
- Pair production

Generally, for most materials exposed to 1-100MeV energy beam source, Compton scattering and photoelectric absorption attributes most to scattering and it's common to ignore Rayleigh scattering and Pair production. So the attenuation coefficient can be expressed as

$$\mu_t = (\mu/\rho)\rho = (\mu_{photo}/\rho)\rho + (\mu_{compton}/\rho)\rho \quad (6.2)$$

Each kind of element media shows distinctive mass attenuation coefficient. For heterogeneous material, the mass attenuation coefficient includes effectiveness of all compound elements and is defined as below:

$$\mu_t = \sum_i W_i (\mu/\rho)_i \rho_i \quad (6.3)$$

Here  $W_i$  is fraction by weight of  $i_{th}$  atomic constituent.

In CT process, the represented value of  $\mu$  reconstructed from measured data is determined by mass density  $\rho$  and atomic number  $Z$  of absorber under given spectral source  $S(E)$  and detector characteristics  $D(E)$ :[45]

$$\mu = \int w(E) \mu_t(E) dE \quad \text{where} \quad w(E) = \frac{S(E)D(E)}{\int S(E)D(E)dE} \quad (6.4)$$

When measuring at two different energy levels, atomic number  $Z$  and density  $\rho$  can be deduced from the obtained  $\mu_1$  and  $\mu_2$  combined with energy spectrum and detector

information:

$$\begin{pmatrix} \mu_1(Z, \rho) \\ \mu_2(Z, \rho) \end{pmatrix} \rightarrow \begin{pmatrix} Z(\mu_1, \mu_2) \\ \rho(\mu_1, \mu_2) \end{pmatrix} \quad (6.5)$$

Using standard database as attenuation reference as figure 6.1 indicates, [46] the deducing process can be realized through numerical interpolation. Taking ratio of the measured  $\mu_1$  and  $\mu_2$  at two different energy levels,

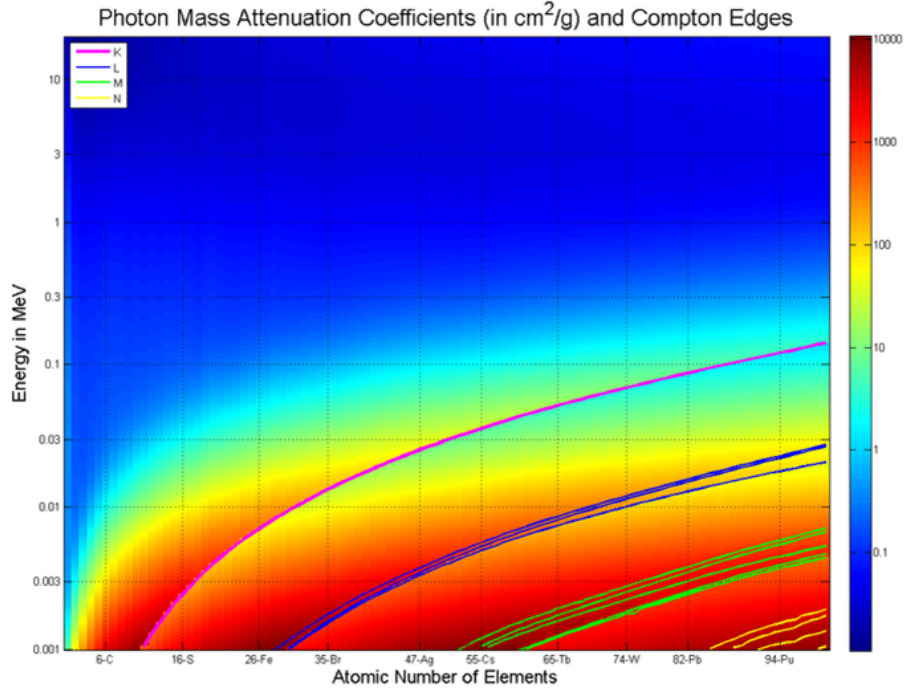


FIGURE 6.1: Standard database of attenuation

$$\frac{\mu_1}{\mu_2} = \frac{f_1}{f_2} = F(Z) \quad (6.6)$$

Here

$$f_j(Z) = \int w_j(E) \mu_m(E, Z) \rho dE \quad j = 1, 2 \quad (6.7)$$

$F(Z)$  shows as monotonic function with  $\mu_1/\mu_2$  so that we can get atomic number  $Z$  through numerical interpolation: [45]

$$Z = F^{-1}(\mu_1/\mu_2) \quad (6.8)$$

Relatively, density can be obtained by

$$\rho = \frac{\mu_j}{f_j(Z)} = \frac{\mu_j}{f_j[F^{-1}(\mu_1/\mu_2)]} \quad (6.9)$$

For heterogeneous material, atomic number  $Z$  and density  $\rho$  are defined as

$$\rho = \sum_i \rho_i \quad Z = \frac{\sum_i Z_i \rho}{\sum_i \rho_i}. \quad (6.10)$$

Simulation program is developed based on the above method and the flowchart is explained in figure 6.2.

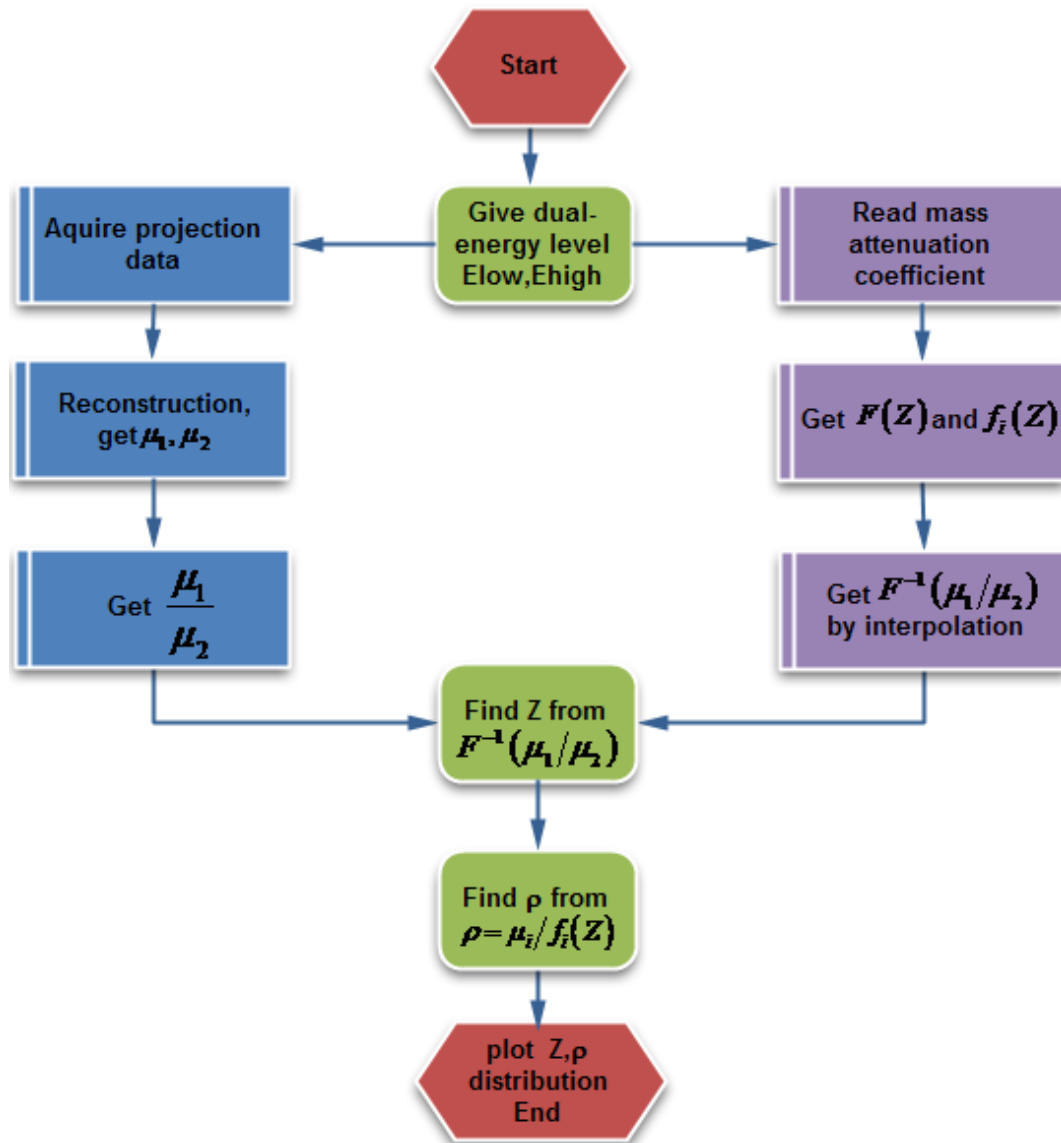


FIGURE 6.2: Program flowchart of dual-energy CT analysis

### 6.1.2 Simulation with monochromatic beam

Simulation is carried out with monochromatic beam at the first place. Beam energy is chosen as 30/60keV and detector efficiency is assumed as constant factor of 1. A very

simple phantom is designed in figure 6.3 of a concrete round sample. In the concrete, there is one steel rod with erosion coating with thickness of half its radius. The material parameters are listed in table 6.1 and atomic number  $Z$  for compounds and mixtures is calculated referring the density and composition from standard data table of NIST. [46] The relationship between atomic number  $Z$  and the ratio of  $\mu_1/\mu_2$  is displayed as  $F(Z)$  curve in figure 6.4. The black line is drawn according to the true value in database and the red line is interpolation result which corresponds well with the true value.

During simulation, identification of  $Z$  is very noisy especially in air region. Actually there is a relatively large gap of density magnification between air and steel or concrete referring to table 6.1. Such phenomenon makes the  $\mu$  value of air is almost 0 compared with other material. When taking ratio of  $\mu_1/\mu_2$  for air region, slight error of  $\mu_1$  or  $\mu_2$  with very small value will cause large error in the ratio value, so that air region cannot show correct identification result. For other material with relatively large density and  $\mu$  value, there is no such problem. In order to avoid blurring and smoothing of boundary between each materials by simply filtering, calibration instead of filtering is applied for air region. The  $\mu$  of reconstructed image with too small value ( $< 0.05$ ) are considered as within air region and automatically set as theoretical value of  $\mu_1$  or  $\mu_2$  of air. In this way, the noise is eliminated in air region during material identification.

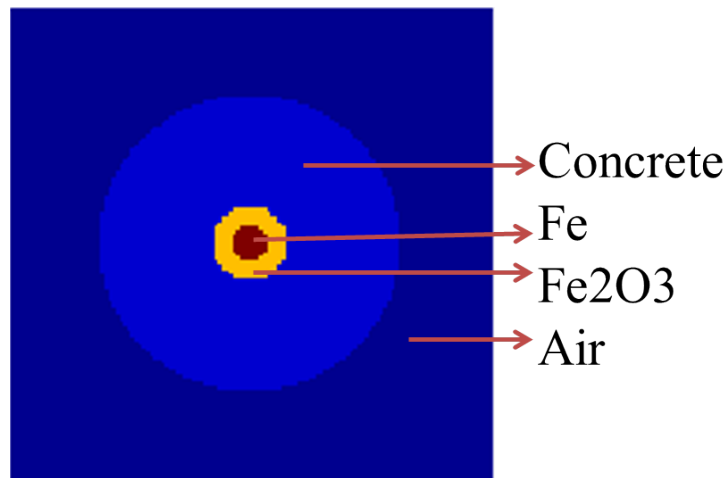
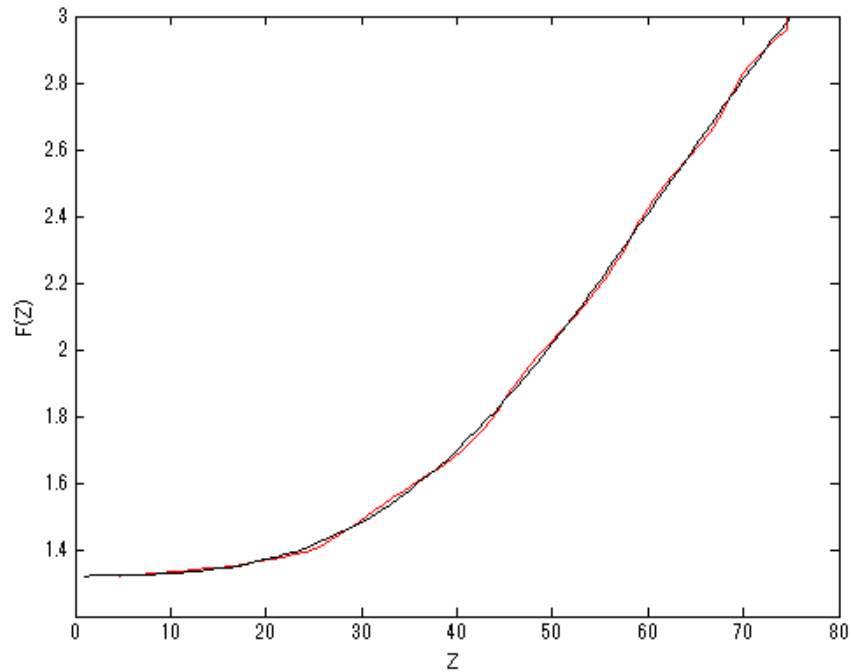


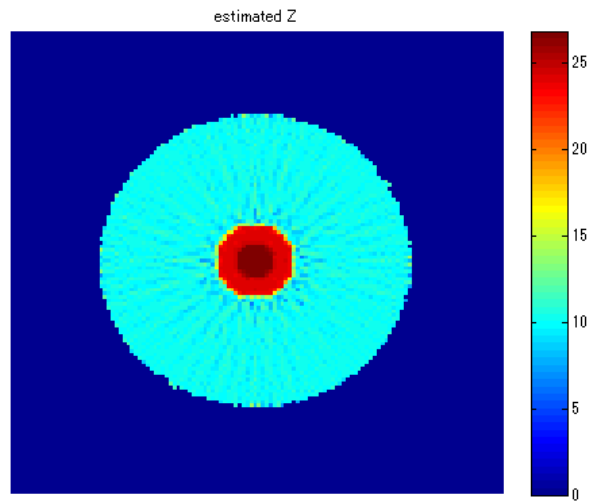
FIGURE 6.3: Simulation phantom of dual-energy CT analysis

Figure 6.5 is the results of estimated atomic number  $Z$  and density  $\rho$ , and the error is showed in figure 6.6. Corrosion coating can be identified clearly in the result. For Fe and Fe<sub>2</sub>O<sub>3</sub>, error of  $Z$  value is within 0.2-1.3 and error of density is within  $0.3g/cm^3$ . Some value near boundary between each materials is not precise enough mainly due to error during image reconstruction.

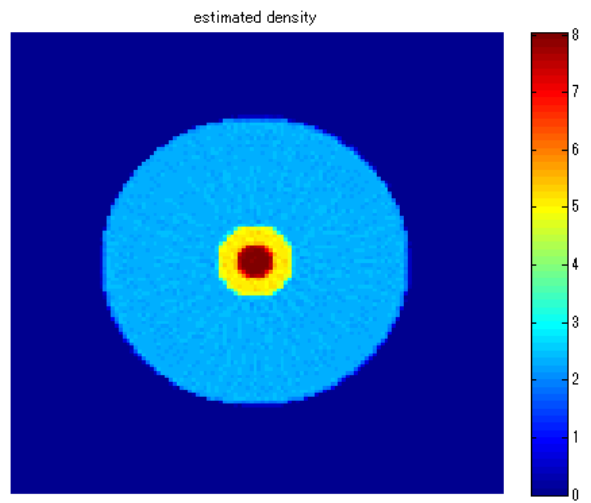
TABLE 6.1: Parameters of materials in the phantom

Material	Atomic number	Composition (Z: fraction by weight)	Density $g/cm^3$
Concrete	11.9877	1:0.022100	2.3
		6:0.002484	
		8:0.574930	
		11:0.015208	
		12:0.001266	
		13:0.019953	
		14:0.304627	
		19:0.010045	
20:0.042951			
26:0.006435			
Air	7.6776	6:0.000124	1.205E-03
		7:0.755268	
		8:0.231781	
		18:0.012827	
Fe	26	26:1	7.784
Fe <sub>2</sub> O <sub>3</sub>	23.0128	8:0.31582	5.24
		6:0.6842	

FIGURE 6.4:  $F(Z)$  curve under 30/60keV (black: true value; red: interpolation value)

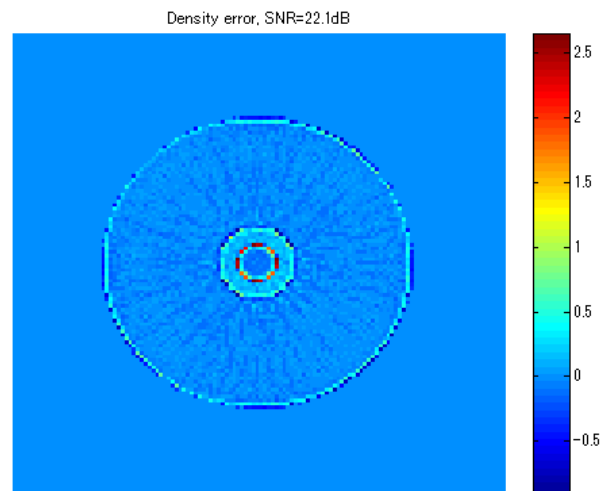


(A) Estimated atomic number  $Z$

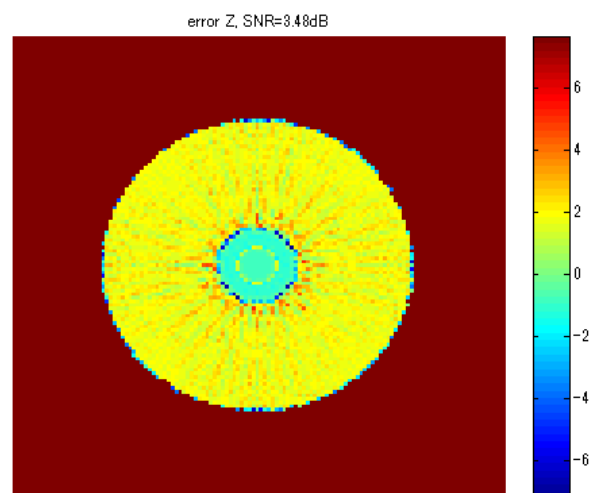


(B) Estimated density  $\rho$

FIGURE 6.5: Estimated material with monochromatic beam (30/60keV)



(A) Error of estimated atomic number  $Z$



(B) Error of estimated density  $\rho$

FIGURE 6.6: Error of estimated material with monochromatic beam (30/60keV)

### 6.1.3 Simulation with spectrum beam

Further simulation is complied considering spectrum beam and detector efficiency in accordance to the CT model in figure 6.7. The two scintillator compacted in line sensor is a thin detector of 5mm CsI with low transmittance, and a thick detector of 15mm CdWO<sub>4</sub> with high transmittance. The two detector are sensitive for low and high energy beam respectively. Such CT model can get dual-energy data at just one scanning and reduce measuring time to only half of ordinary model needs. The 3.95MeV Linac spectrum is employed as beam source and the equation 6.4 is used during simulation to determine the measured attenuation value of the absorber. Spectral source  $S(E)$  and detector characteristics  $D(E)$  are given by EGS5 simulation results in figure 6.8. The relationship between atomic number  $Z$  and the ratio of  $\mu_1/\mu_2$  under such spectrum beam is displayed as  $F(Z)$  curve in figure 6.9 and interpolation result still can correspond well with the true value.

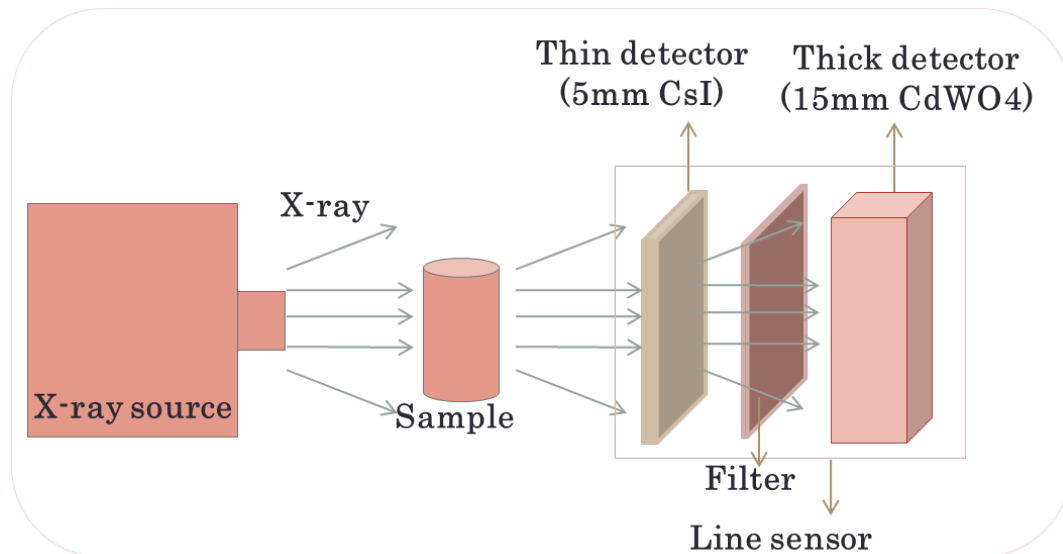
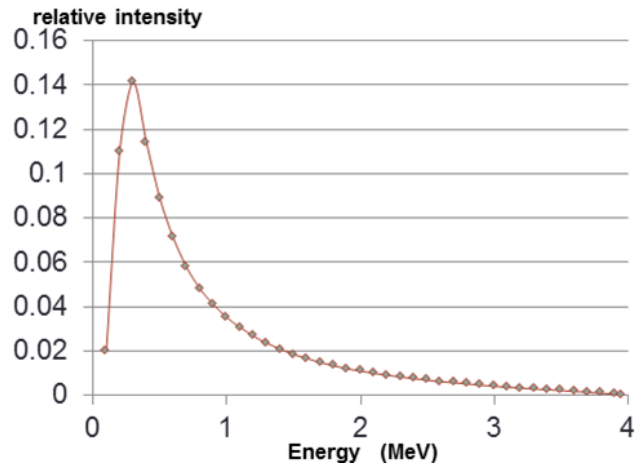
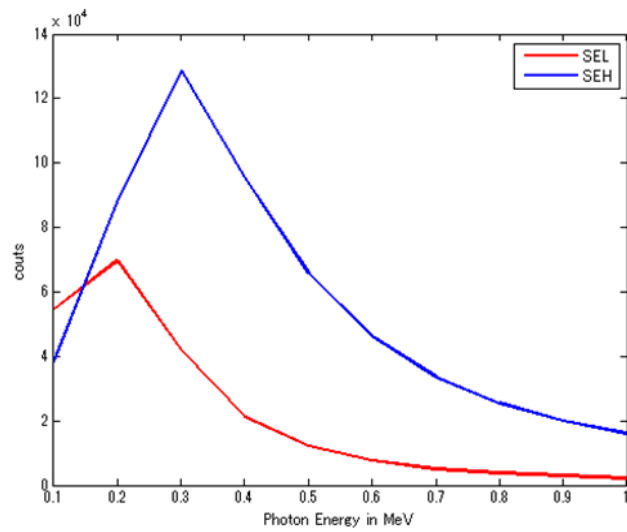


FIGURE 6.7: Simulation model of dual-energy CT using spectrum beam

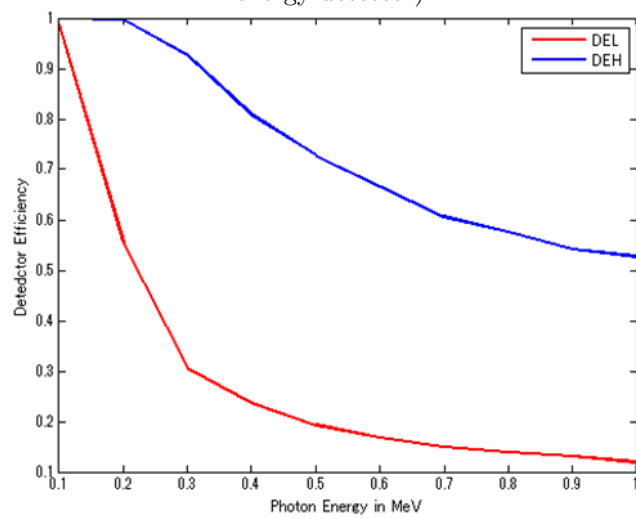
The estimated information of media materials are showing very good accuracy as displayed in figure 6.10 and figure 6.11. Both atomic number  $Z$  and density  $\rho$  are clearly distinguished among each material boundary, although some deviation appeared near the boundaries due to error during CT reconstruction. Rising resolution of sectional images is one of the approaches to avoid such error. The correct results of this simulation example suggests that it's very promising to using dual-energy CT analysis for practical identification of internal materials under spectrum beam irradiation.



(A) 3.95 linac spectrum



(B) Absorbed spectrum in line sensor (red: low energy detector; blue: high energy detector)



(C) Detector efficiency of line sensor (red: low energy detector; blue: high energy detector)

FIGURE 6.8: EGS5 simulation results about spectrum and detector

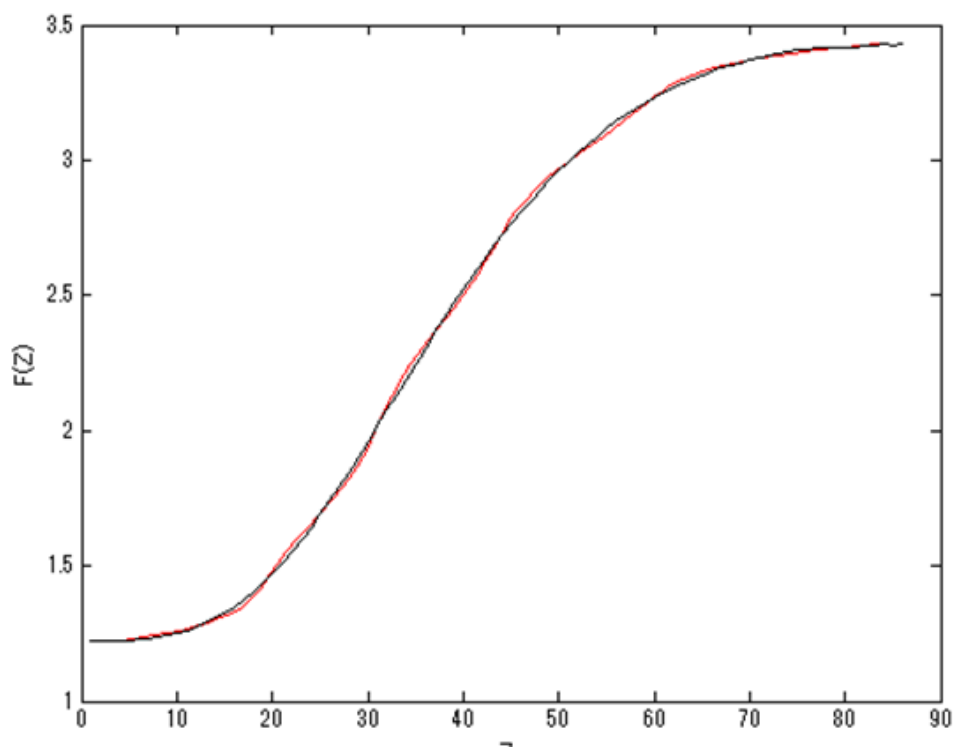
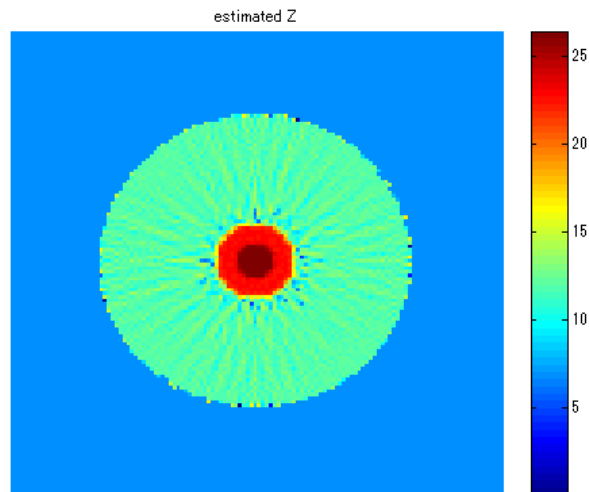
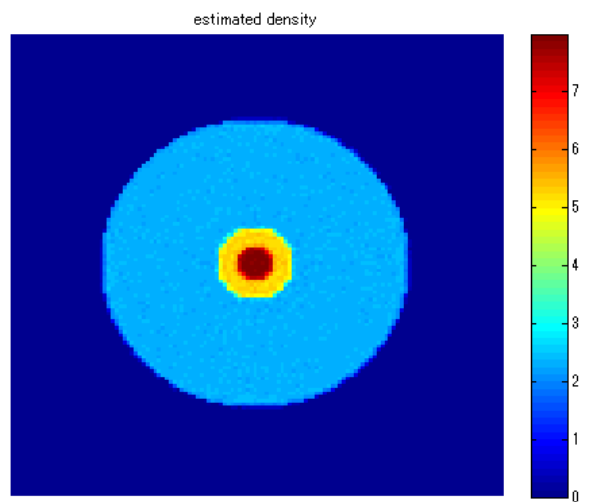


FIGURE 6.9:  $F(Z)$  curve under spectrum beam (black: true value; red: interpolation value)

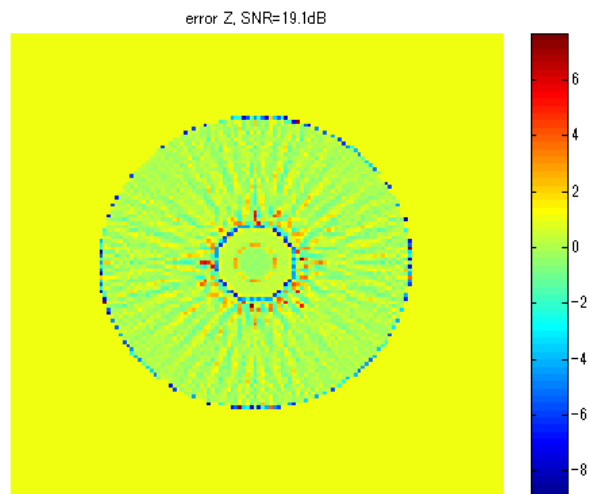


(A) Estimated atomic number  $Z$

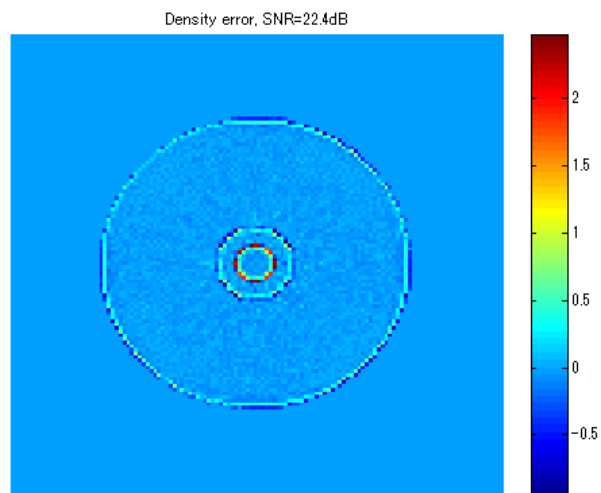


(B) Estimated density  $\rho$

FIGURE 6.10: Estimated material with spectrum beam



(A) Error of estimated atomic number  $Z$



(B) Error of estimated density  $\rho$

FIGURE 6.11: Error of estimated material with spectrum beam

## 6.2 Experiment for Material Identification of Rusty Iron Sample

### 6.2.1 Experiment set-up

The X-ray source is 3.95MeV Linac and large FPD (Perkin Elmer XRD1622) is adopted as detector. 4 sheets of Iron plates each with 4.25mm thickness are used as filters to adjust source in order to obtain two energy level beam. Projection data of full angle was taken twice: once when directly using beam from Linac, and then taken it again when filters are installed in front of Linac. The beam spectrum and detector sensitivity are simulated with EGS5 program.

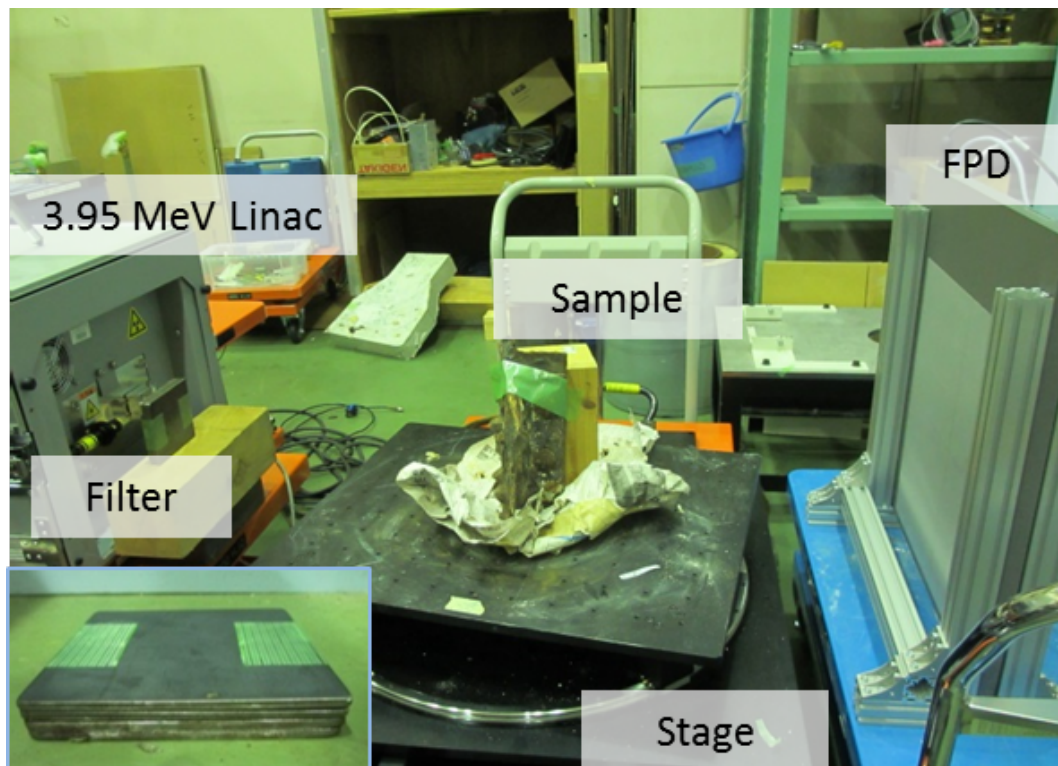


FIGURE 6.12: Experiment setup of dual-energy CT

The rusty iron sample is a serious corroded “ T ” shape component cut from aging steel bridge, as showed in figure 6.13.



(A) Lateral view

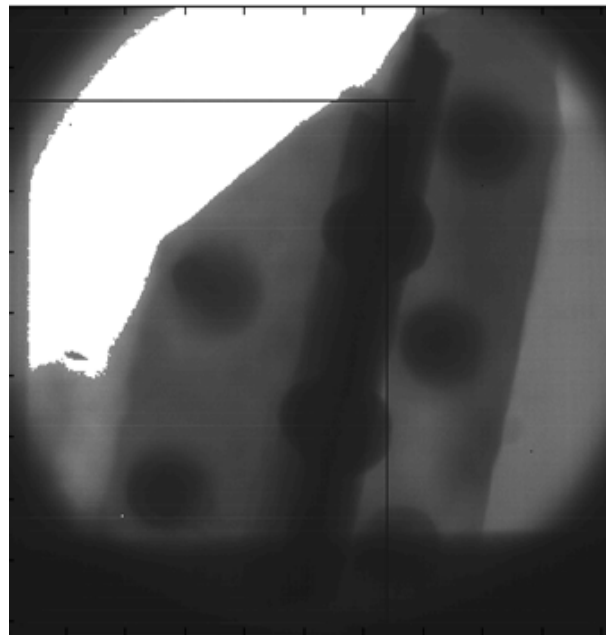


(B) Top view

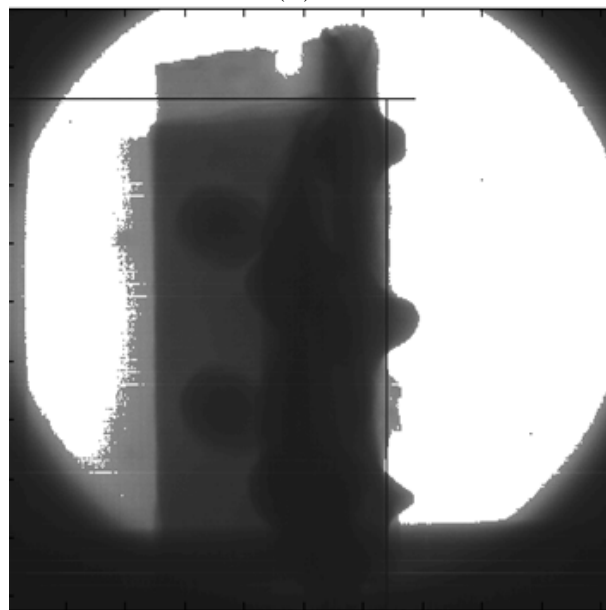
FIGURE 6.13: Rusty iron sample

### 6.2.2 Results and discussion

The transmission image from  $0^\circ$  and  $90^\circ$  are showed in figure 6.14. The sectional layer at the middle height of the sample is selected to reconstruct a section image as figure 6.15 showed. Through estimation from ratio  $\mu_1/\mu_2$  under given spectrum and detector efficiency, the estimated atomic number  $Z$  and density  $\rho$  are illustrated in figure 6.16. However, as well known that atomic number  $Z$  of iron is 26 and for rusty iron  $Z$  is around 23, the estimated result gives value above 40, which is very large error.



(A)  $0^\circ$



(B)  $90^\circ$

FIGURE 6.14: Transmission image of rusty steel sample

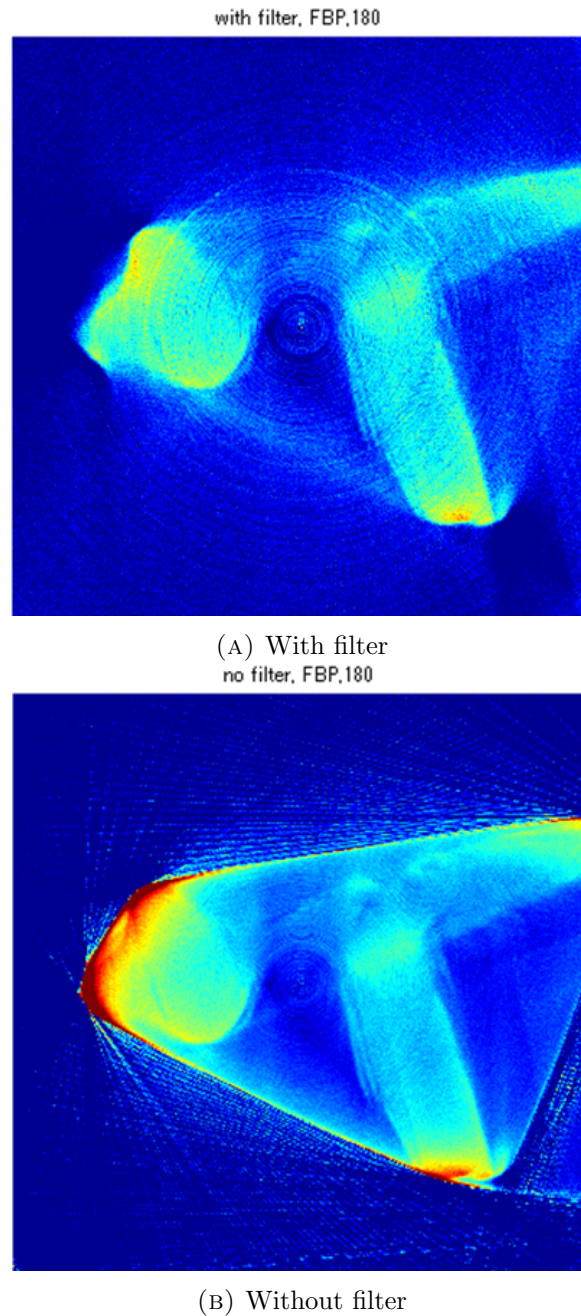


FIGURE 6.15: Reconstructed image of rusty steel sample

Possible reasons for such large error are discussed. The main reason is uncertainty of necessary spectrum data that is indispensable for the material estimation analysis. It's very difficult to monitoring the real beam spectrum during experiment. The used simulation result is after all different from real data during actual experiment condition. Besides, the Linac operation was interrupted several times due to unstable factors. The interruption caused that the beam intensity varies for all projection data. It increases error in CT reconstruction together with ring artifact and beam hardening effect. Moreover, the attenuation ability of Fe and  $\text{Fe}_2\text{O}_3$  are too close under the using energy level

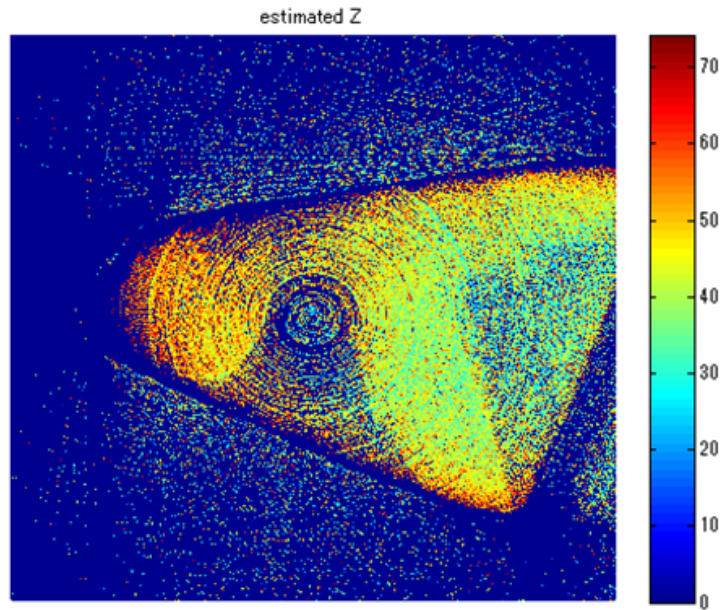
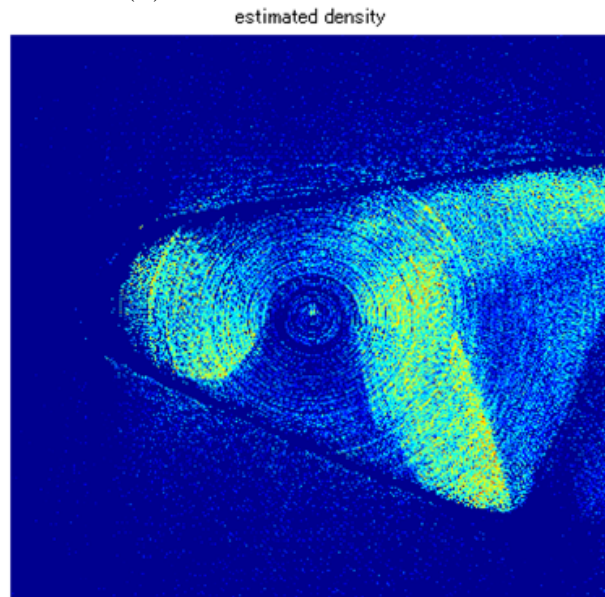
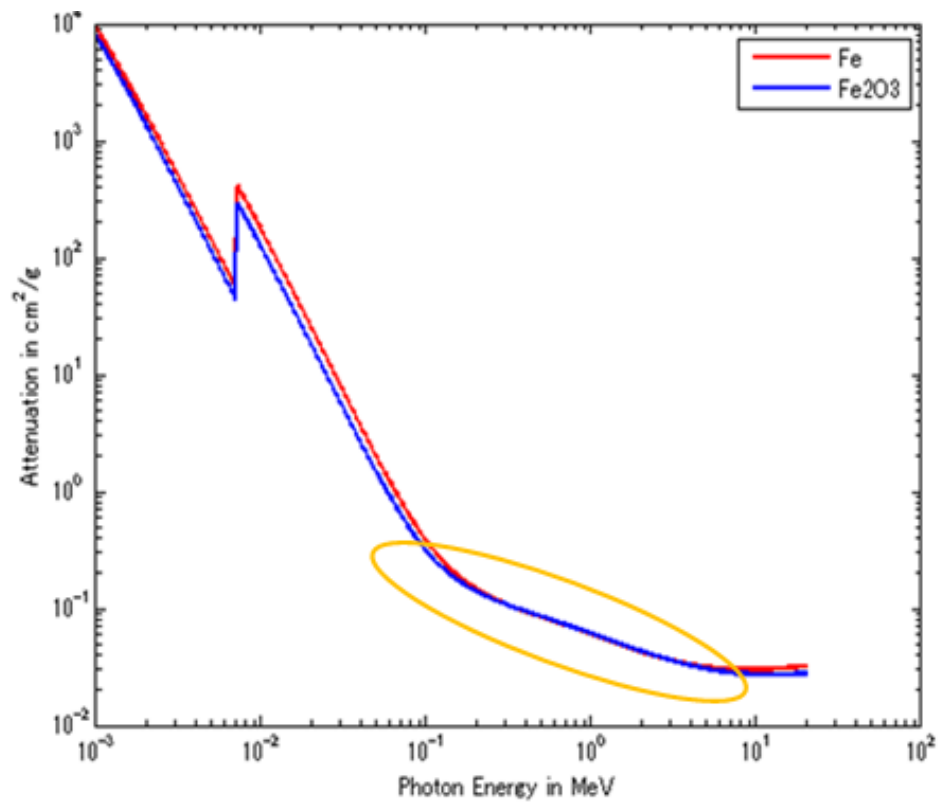
(A) Estimated atomic number  $Z$ (B) Estimated density  $\rho$ 

FIGURE 6.16: Estimated material of rusty steel sample

around a few MeV magnitude as indicated in figure 6.17. Comprehensively in such a case, the accuracy of material identification become unsatisfactory outcome.

In order to solve the above problems, filter material and thickness should be further optimized to prevent beam hardening effect. Other improvement such as compensation algorithm is also considered. Since it is very difficult to probe more information about real spectrum, calibration before estimation is proposed using information by attaching reference sample with known material to the object.

FIGURE 6.17: Attenuation ability of Fe and Fe<sub>2</sub>O<sub>3</sub>

## Chapter 7

# Conclusion and Future Work

### 7.1 Conclusion

The main work of this research is concentrated on in situ NDE technique development for internal structure of degradation bridge with portable 950keV/3.95MeV Linac X-ray beam source. Specific inspection methods are proposed for inspection of reinforced steel rebar thinning problem, prestressed steel wire cluster soundness problem and corrosion of steel component problem. In situ NDE experiment is successfully implemented for RC rebar inspection using radiography imaging. For realization of quantitative evaluation, methods are proposed with analyzing radiography images and image enhancement by tomosynthesis. In situ NDE experiment for PC structure is also conducted and based on this experience, computer tomography is proposed with consideration of partial projection conditions. Possible solution is proposed based on relative simulation and experiment work. As for corrosion evaluation, dual-energy analysis with computed tomography image is adopted. The following explains the major conclusions together with the work structure of figure 7.1 in this research.

Because the RC rebar is just a single steel rod, it's very easy to be confirmed in radiography image. Through the in situ NDE experiment to aging pillars of a berth pier, the operation procedure is established for field work using portable Linac as beam source. The transmission image provided intuitive and reliable result of inner RC steel rebar. It achieved satisfying evaluation conclusion and appropriate maintenance scheme was planned according to the measured rod diameter reduction situation. But it's still undeniable that without prior information, it's very difficult to evaluate the thing rate of rebar diameter quantitatively. One solution is proposed as analysis of radiography images at different measuring geometry. The test experiment proved the acceptable accuracy of quantitative estimation. More precise result is expected using

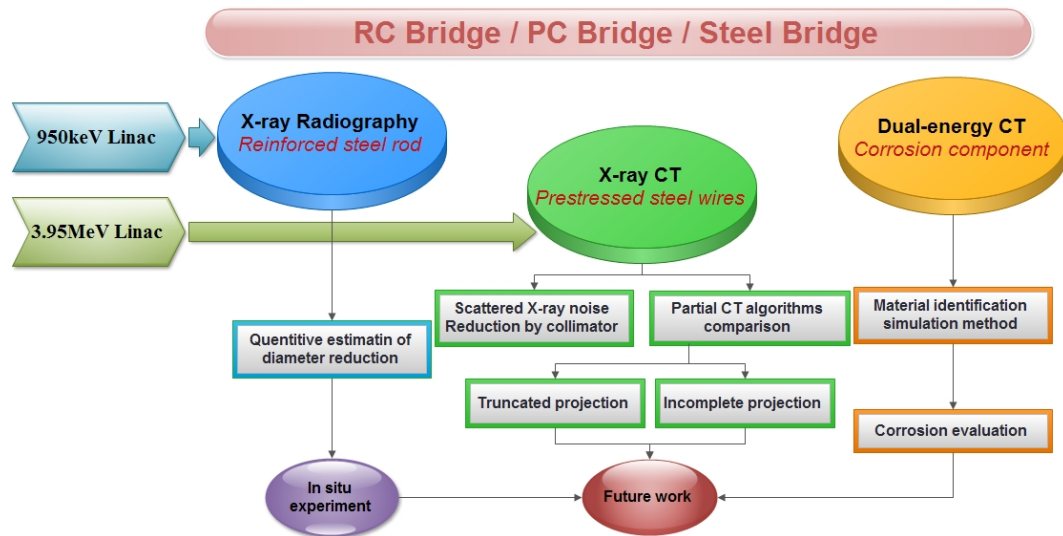


FIGURE 7.1: Research work structure

better enhanced images by other treatment such as tomosynthesis, which analyzes and reconstructs synthesized images with clear edge by transmission at several directions .

It's necessary to inspection PC wire clusters by sectional image reconstructed by Computed Tomography, because each bundle of clusters consists of more than 10 steel wires so that the overlapping reflection presented in transmission image can not tell detail information of the cluster. This situation is verified in situ experiment for PC structure. However, due to practical bridge scale and other constraints, partial CT methods become undeniable problem. According to simulation work, lack of enough projection data would induce artifacts and shadow which would deteriorate the reconstructed image quality. Advanced algorithms are compared and studied for improving the image quality. Simultaneous Algebraic Reconstruction Technique with Total Variation Minimization (SART-TV) is based on Compressed Sensing Theorem using Total Variation Minimization. It's effective to recover the sectional image when projection is incomplete or sparse in scanning angle range. Differentiated Back Projection with Hilbert transform (DBPH) cost very short time for reconstruction and it can avoid truncation influence to reconstruction about region of interest. Further comparison of the algorithms are analyzed combined with experiment in laboratory. Collimator is adopted during CT projection experiment to improve the raw data quality by reducing scattered X-ray noise. It's proved that the reconstructed sectional images and 3D model built from these slices can provide valuable reference for evaluation of inner structure and overall mechanical analysis. Through reconstruction under incomplete projection of limited or sparse projection conditions, the influence of partial CT is further verified. The SART-TV algorithm is also applied to practical partial CT reconstruction with experiment data. The recovery ability is apparent while it still needs to be improved

about the adjustment for appropriate parameter based on the raw data character. The CT application for real large concrete specimen cut from bridge girder is difficult to be realised due to problems like overexposure caused by the large scale and complex shape, which will be solved by adjusting irradiation time and designing proper filter. Scaled down specimen is tested for ROI tomography and the DBPH algorithm is very valid to present successful image of ROI. It's proved that this algorithm possess excellent resistance to truncated projection influence.

Corrosion evaluation method of steel components is proposed by discerning iron and rusty iron material using dual-energy CT analysis, which can distinguish the material by identifying the atomic number and density on the section of media object. The program is developed and simulation is successfully achieved for accurate estimation of the rusty layer of inner steel rebar in concrete sample under both monochromatic and spectrum beam source. Practice to rusty component cut from real steel bridge showed large error because of several reasons, such as lack of precise information of spectrum, beam hardening effect, small difference of attenuation ability between iron and rusty iron, etc. The spectrum uncertainty problem may be solved by calibration based on reference attachment with known material. Compensation algorithm may correct the beam hardening effect together with suitable filter to adjust beam intensity. The lower energy level of dual-energy CT will also make it easier to discriminate iron and rusty iron.

The mentioned inspection results would provide meaningful information for further evaluations referring to mechanical analysis and civil work criterions. Along with currently existed regular inspection for bridge of annually visual and tapping test, inspection by our method is expected for every 5 years in order to strengthen the prevention to early deterioration phenomenon of internal structures.

## 7.2 Future Work

The current research results imply that it's very promising to use portable Linac beam source for in situ NDE inspection for aging bridges by radiography and CT analysis. The fundamental application procedure is developed and established through simulation and experiment work. However, there is still problems need to be solved in future work.

1. Field work should be applied for quantitative evaluation of RC rebar thinning problem when prior information is unaccessible. The accuracy needs to be verified for geometry analysis of radiography image. At the same time, it would also be

beneficial to adopt some processing of transmission image by tomosynthesis or other treatment.

2. The advanced partial CT reconstruction algorithms should be optimized combined with experiment raw data to apply PC wire cluster inspection. The experiment system should be improved especially on source energy and detector to adapt to specimen with complex shape and large scale.
3. Practice for dual-energy CT analysis should be designed and conducted considering compensation and correction for several possible influencing factors including beam spectrum uncertainty and beam hardening, etc.

# Bibliography

- [1] Takenobu Kitamura Takashi Tamakoshi, Masanori Okubo. Annual report of basic data on road structures in fy 28. Technical report, National Institute for Land and Infrastructure Management, 2009.
- [2] Atsushi Yoshioka. Missions and particular activities of the center for advanced engineering structural assessment and research. Technical report, CAESAR, 2008.
- [3] Frederic J. Frommer. I-35w bridge collapses, August 1, 2007.
- [4] Joachim Naumann and Peter Haardt. Ndt methods for the inspection of highway structures. In *International Symposium Non-Destructive Testing in Civil Engineering*, 2003.
- [5] Glenn Washer. Nondestructive evaluation for highway bridges in the united states. In *International Symposium Non-Destructive Testing in Civil Engineering*, 2003.
- [6] GV Minesawa, Eiichi Sasaki, Chitoshi Miki, Kanako Kozaki, and Keigo Suzuki. Eddy current inspection of concrete embedded steel elements. In *Review of Progress in Non-Destructive Evaluation: VOLUME 32*, volume 1511, pages 1349–1354. AIP Publishing, 2013.
- [7] Robert A Novelline and Lucy Frank Squire. *Squire's fundamentals of radiology*. La Editorial, UPR, 2004.
- [8] H. H. Lester. X-rays in the steel industry. *Journal of the American Society for Naval Engineers*, 43(3):467–474, 1931.
- [9] Mitsuru Ueaska, Ming Jin, Wenjing Wu, Katsuhiko Dobashi, Takeshi Fujiwara, Jyoichi Kusano, Naoki Nakamura, Masashi Yamamoto, Eiji Tanabe, Seiji Ohya, Yukiya Hattori, and Itaru Miura. Commissioning of portable 950 keV/3.95 MeV x-band linac x-ray sources for on-site transmission testing. *E-Journal of Advanced Maintenance*, 5(2):93–100, 2013.
- [10] Elizabeth C Beckmann. Ct scanning the early days. *The British Journal of Radiology*, 79(937):5–8, 2006.

- 
- [11] Willi A. Kalender. X-ray computed tomography. *Physics in Medicine and Biology*, 51(13):R29–R43, 2006.
- [12] Pan Xiaochuan, Siewerdsen Jeffrey, La Riviere Patrick J., and Kalender Willi A. Anniversary paper: Development of x-ray computed tomography: The role of medical physics and aapm from the 1970s to present. *Medical Physics*, 35(8):3728, 2008.
- [13] G. Wang, H. Y. Yu, and B. De Man. An outlook on x-ray ct research and development. *Medical Physics*, 35(3):1051–1064, 2008.
- [14] X. C. Pan, E. Y. Sidky, and M. Vannier. Why do commercial ct scanners still employ traditional, filtered back-projection for image reconstruction? *Inverse Problems*, 25(12), 2009.
- [15] J Lambert, AR Chambers, I Sinclair, and SM Spearing. 3d damage characterisation and the role of voids in the fatigue of wind turbine blade materials. *Composites Science and Technology*, 72(2):337–343, 2012.
- [16] Julien Noel. Advantages of ct in 3d scanning of industrial parts. *3D Scanning Technologies Magazine*, 1(3):18, 2008.
- [17] T. Fuchs, P. Kesling, M. Firsching, F. Nachtrab, and G. Scholz. *Industrial Applications of Dual X-ray Energy Computed Tomography (2X-CT)*, volume 6 of *RILEM Bookseries*, chapter 13, pages 97–103. Springer Netherlands, 2013.
- [18] Heiskanen, Kaarlo A. and Rhim Hong C., Monteiro, and Paulo J. M. Computer simulations of limited angle tomography of reinforced concrete. *Cement and Concrete Research*, 21(4):625–634, 1991.
- [19] Pat Baldwin. Digital breast tomosynthesis. *Radiologic technology*, 81(1): 57M–74M, 2009.
- [20] Malcolm Slaney A C. Kak. *Principle of Computerized Tomographic Imaging*. IEEE, New York, 1999.
- [21] Gabriel Peyre. The numerical tours of signal processing - advanced computational signal and image processing. *IEEE Computing in Science and Engineering*, 13(4): 94–97, 2011.
- [22] Wuyts Sarah Van Hemelryck Tessa. *The implementation of iterative reconstruction algorithms in MATLAB*. master, University College of Antwerp, 2007.
- [23] Gabor T. Herman, Arnold Lent, and Stuart W. Rowland. Art: Mathematics and applications: A report on the mathematical foundations and on the applicability

- to real data of the algebraic reconstruction techniques. *Journal of Theoretical Biology*, 42(1):1–32, 1973.
- [24] S. Kaczmarz. Angenaherte auflosung von systemen linearer gleichungen. *Bull.Acad. Pol. Sci. Lett. A*, 6(8A):355–357, 1937.
- [25] Per Christian Hansen and Maria Saxild-Hansen. Air tools ? a matlab package of algebraic iterative reconstruction methods. *Journal of Computational and Applied Mathematics*, 236(8):2167–2178, 2012.
- [26] D. Fleischmann and F. E. Boas. Computed tomography-old ideas and new technology. *European Radiology*, 21(3):510–517, 2011.
- [27] A. H. Andersen and A. C. Kak. Simultaneous algebraic reconstruction technique (sart): A superior implementation of the art algorithm. *Ultrasonic Imaging*, 6(1): 81–94, 1984.
- [28] E. J. Candes, J. Romberg, and T. Tao. Robust uncertainty principles: exact signal reconstruction from highly incomplete frequency information. *Information Theory, IEEE Transactions on*, 52(2):489–509, 2006.
- [29] Emil Y. Sidky, Chien-Min Kao, and Xiaochuan Pan. Accurate image reconstruction from few-views and limited-angle data in divergent-beam ct. *Journal of X-Ray Science and Technology*, 14(2):119–139, 2006.
- [30] Emmanuel J. Candes, Justin K. Romberg, and Terence Tao. Stable signal recovery from incomplete and inaccurate measurements. *Communications on Pure and Applied Mathematics*, 59(8):1207–1223, 2006.
- [31] D. L. Donoho. Compressed sensing. *Information Theory, IEEE Transactions on*, 52(4):1289–1306, 2006.
- [32] Emmanuel J. Candes and Justin K. Romberg. Signal recovery from random projections. *Computational Imaging III*, pages 76–86, 2005.
- [33] E. Candes and J. Romberg. Robust signal recovery from incomplete observations. In *Image Processing, 2006 IEEE International Conference on*, pages 1281–1284, 2006.
- [34] Emmanuel J. Candes and Franck Guo. New multiscale transforms, minimum total variation synthesis: applications to edge-preserving image reconstruction. *Signal Processing*, 82(11):1519–1543, 2002.
- [35] Xin Jin, Liang Li, Zhiqiang Chen, Li Zhang, and Yuxiang Xing. Anisotropic total variation for limited-angle ct reconstruction. In *Nuclear Science Symposium Conference Record (NSS/MIC), 2010 IEEE*, pages 2232–2238, 2010.

- [36] Chen Zhiqiang, Jin Xin, Li Liang, and Wang Ge. A limited-angle ct reconstruction method based on anisotropic tv minimization. *Physics in Medicine and Biology*, 58(7):2119, 2013.
- [37] Yan Liu, Jianhua Ma, Yi Fan, and Zhengrong Liang. Adaptive-weighted total variation minimization for sparse data toward low-dose x-ray computed tomography image reconstruction. *Physics in Medicine and Biology*, 57(23):7923, 2012.
- [38] R. Clackdoyle and M. Defrise. Tomographic reconstruction in the 21st century. *Signal Processing Magazine, IEEE*, 27(4):60–80, 2010.
- [39] Frederic Noo, Rolf Clackdoyle, and Jed D Pack. A two-step hilbert transform method for 2d image reconstruction. *Physics in Medicine and Biology*, 49(17):3903, 2004.
- [40] Hiroyuki Kudo, Taizo Suzuki, and Essam A. Rashed. Image reconstruction for sparse-view ct and interior ct?introduction to compressed sensing and differentiated backprojection. *Quantitative Imaging in Medicine and Surgery*, 3(3):147–161, 2013.
- [41] Akitake Makinouchi. Vcad system: Advanced software system for production engineering and biological research. *JSCES*, 15(2):2309–2315, 2010.
- [42] Kiwoo Lee. *Dual energy X-ray imaging for material recognition using 950 keV X-band Linac*. Doctoral dissertation, The University of Tokyo, 2010.
- [43] Hideo Hirayama, Yoshihito Namito, Walter R Nelson, Alex F Bielajew, Scott J Wilderman, and U Michigan. The egs5 code system. Technical report, United States. Department of Energy, 2005.
- [44] Costel Rizescu, Calin Besliu, and Alexandru Jipa. Determination of local density and effective atomic number by the dual-energy computerized tomography method with the 192ir radioisotope. *Nuclear Instruments and Methods in Physics Research Section A: Accelerators, Spectrometers, Detectors and Associated Equipment*, 465(2-3):584–599, 2001.
- [45] B. J. Heismann. Density and atomic number measurements with spectral x-ray attenuation method. *Journal of Applied Physics*, 94(3):2073–2079, 2003.
- [46] S. M. Seltzer J. H. Hubbell. Tables of x-ray mass attenuation coefficients and mass energy-absorption coefficients, 1996.

- [47] D. Breyse. Nondestructive evaluation of concrete strength: An historical review and a new perspective by combining ndt methods. *Construction and Building Materials*, 33:139–163, 2012.
- [48] Rudin, Leonid I., Osher, Stanley, Fatemi, and Emad. Nonlinear total variation based noise removal algorithms. *Physica D: Nonlinear Phenomena*, 60(1?4): 259–268, 1992.
- [49] Schulze R., Heil U. and Gross D., Bruellmann D. D., Dranischnikow E., Schwanecke U., and Schoemer E. Artefacts in cbct: a review. *Dentomaxillofacial Radiology*, 40(5):265–273, 2011.
- [50] J.T. Bushberg. *The Essential Physics of Medical Imaging*. Lippincott Williams and Wilkins, 2002.
- [51] R. Clackdoyle, F. Noo, Guo Junyu, and J. A. Roberts. Quantitative reconstruction from truncated projections in classical tomography. *Nuclear Science, IEEE Transactions on*, 51(5):2570–2578, 2004.
- [52] Michel Defrise, Frederic Noo, Rolf Clackdoyle, and Hiroyuki Kudo. Truncated hilbert transform and image reconstruction from limited tomographic data. *Inverse Problems*, 22(3):1037, 2006.
- [53] GAO Hewei, ZHANG Li, CHEN Zhiqiang, and CHENG Jianping. Reviews of image reconstruction from limited-angle. *CT Theory and Application*, 5(1):46–50, 2006.
- [54] F. Nachtrab, S. Weis, P. Kesling, F. Sukowski, U. Hasler, T. Fuchs, N. Uhlmann, and R. Hanke. Quantitative material analysis by dual-energy computed tomography for industrial ndt applications. *Nuclear Instruments and Methods in Physics Research Section A: Accelerators, Spectrometers, Detectors and Associated Equipment*, 633, Supplement 1(0):S159–S162, 2011.
- [55] Rangaraj Rangayyan, Atam Prakash Dhawan, and Richard Gordon. Algorithms for limited-view computed tomography: an annotated bibliography and a challenge. *Appl. Opt.*, 24(23):4000–4012, 1985.
- [56] Ioannis Sechopoulos. A review of breast tomosynthesis. part i. the image acquisition process. *Medical Physics*, 40(1), 2013.
- [57] Ioannis Sechopoulos. A review of breast tomosynthesis. part ii. image reconstruction, processing and analysis, and advanced applications. *Medical Physics*, 40(1), 2013.

- [58] Gheorghe TODORAN, Rodica HOLONEC, and Ciprian IAKAB. Discrete hilbert transform. numeric algorithms. *Facultatea de Inginerie Electrica*, 2008.
- [59] Dean Verhoeven. Limited-data computed tomography algorithms for the physical sciences. *Appl. Opt.*, 32(20):3736–3754, 1993.
- [60] Zhen Wang and Hiroyuki Kudo. Metal artifact reduction in x-ray computed tomography by using analytical dbp-type algorithm. In *Physics of Medical Imaging*, volume 8313, 2012.
- [61] Wenjing Wu, Haitao Zhu, Ming Jin, Katsuhiko Dobashi, Takesi Fujiwara, Mitsuru Uesaka, Joichi Kusano, Naoki Nakamura, Eiji Tanabe, Hideyuki Sunaga, and Yoshie Otake. Partial ct and structural analysis with 950 kev/3.95 mev x-band linac x-ray sources. *E-Journal of Advanced Maintenance*, 5(2):121–127, 2013.
- [62] Lin Xiaozhen, Luo Shouhua, Wang Liyan, He Siyuan, and Chen Gong. An experimental study on dbp and hilbert filtering method for tomography reconstruction. In *Image and Signal Processing (CISP), 2010 3rd International Congress on*, volume 6, pages 2737–2741, 2010.
- [63] Duan Xinhui, Zhang Li, Xing Yuxiang, Zhiqiang Chen, and Cheng Jianping. Few-view projection reconstruction with an iterative reconstruction-reprojection algorithm and tv constraint. *Nuclear Science, IEEE Transactions on*, 56(3):1377–1382, 2009.
- [64] Xu Qiong. *Statistical Reconstruction Methods for Insufficient X-ray CT Projection Data*. PhD thesis, Xi'an Jiaotong University, 2012.
- [65] Ye Yangbo, Yu Hengyong, Wei Yuchuan, and Wang Ge. A general local reconstruction approach based on a truncated hilbert transform. *Journal of Biomedical Imaging*, 2007(1):2–2, 2007.
- [66] Hengyong Yu and Ge Wang. Compressed sensing based interior tomography. *Physics in Medicine and Biology*, 54(9):2791, 2009.
- [67] B. Zhang and G. L. Zeng. Two-dimensional iterative region-of-interest (roi) reconstruction from truncated projection data. *Medical Physics*, 34(3):935–944, 2007.
- [68] Industrial radiography, 2012.
- [69] Liu Baodong. *Reconstruction Algorithms of Industrial CT with Truncated Projection Data*. PhD thesis, Chongqing University, 2010.

- [70] Antonin Chambolle. An algorithm for total variation minimization and applications. *Journal of Mathematical Imaging and Vision*, 20(1-2):89–97, 2004.
- [71] Joachim Dahl, PerChristian Hansen, SorenHoldt Jensen, and TobiasLindstrom Jensen. Algorithms and software for total variation image reconstruction via first-order methods. *Numerical Algorithms*, 53(1):67–92, 2010.
- [72] M. Krause, F. Mielentz, B. Milman, W. Muller, V. Schmitz, and H. Wiggenhauser. Ultrasonic imaging of concrete members using an array system. *NDT and E International*, 34(6):403–408, 2001.
- [73] Xu Qiong, Mou Xuanqin, Tang Shaojie, and Zhang Yanbo. Ct reconstruction based on improved total variation minimization. In *Nuclear Science Symposium Conference Record (NSS/MIC), 2010 IEEE*, pages 3241–3244, 2010.
- [74] Masami Torikoshi, Takanori Tsunoo, Makoto Sasaki, Masahiro Endo, Yutaka Noda, Yumiko Ohno, Toshiyuki Kohno, Kazuyuki Hyodo, Kentaro Uesugi, and Naoto Yagi. Electron density measurement with dual-energy x-ray ct using synchrotron radiation. *Physics in Medicine and Biology*, 48(5):673, 2003.
- [75] Yi Zhang, Wei-Hua Zhang, Hu Chen, Meng-Long Yang, Tai-Yong Li, and Ji-Liu Zhou. Few-view image reconstruction combining total variation and a high-order norm. *International Journal of Imaging Systems and Technology*, 23(3):249–255, 2013.